Nonlinear Optical Methods for Noninvasive Analytics

by

Joshua A. Jasensky

A dissertation submitted in partial fulfillment
of the requirements for the degree of
Doctor of Philosophy
(Biophysics)
in The University of Michigan
2015

Doctoral Committee:

Professor Zhan Chen, Chair
Assistant Professor Julie S. Biteen
Associate Professor Jennifer P. Ogilvie
Professor Gary D. Smith
Professor Nils G. Walter

Dedication

To my family

Acknowledgements

I have a great number of people to thank as I look upon the last number of years; time that I have spent growing both as a scientist, and as a person. My time at the University of Michigan has been extraordinary and it is due to both the experiences I have had, as well as the people who have made it exceptional. Michigan is a unique place; an environment full of great-minded people and the most fascinating research. It will always be a place that I have great memories.

I first would to acknowledge my advisor and mentor, Dr. Zhan Chen, for if it wasn't for his support and dedication, I wouldn't be at the point I am now. I am incredibly lucky to have had the opportunity to work under him, be guided by him, and through this see my development into who I am today. Because of his support, I've had many opportunities that I feel make my graduate school experience unique and special. I appreciate his trust in me and letting me pursue both my own passions in science and research as well as in writing.

It was my undergraduate research advisor, Dr. Paul Urayama, who instilled me with a drive for research and helped foster a passion for knowledge and understanding. It was with his guidance that I owe my initial research success, which has allowed the opportunity to study at the University of Michigan. I thank you for the many opportunities and support that you have given me.

I want to give my special thanks to my collaborators, without whom a large part of this thesis would not be possible. I have had the privilege of working with many groups over the years and

I would like to acknowledge them for their time, resources, valuable discussion, and support. Chapter 2 would not have been possible without the efforts from all of the PI's, postdocs, and students from our MURI. In particular, Professor Charles Brooks, Professor Neil Marsh, Dr. Benjamin Buer and Dr. Shuai Wei have provided invaluable support. Chapters 4 and 5 have been a large part of my graduate career, and all was possible with the support of Professor Gary Smith, Jun Ding, Dr. Christian Jensen, Dr. Thias Fortes, Dr. André Monteiro da Rocha, and Dr. David Lai.

I am also indebted to my committee members, Professors Julie Biteen, Jennifer Ogilive, Gary Smith, and Nils Walter. You have been a great resource support for my graduate work. Many of you I've had the pleasure of working for, either as collaborators, or as a student in your labs. I have learned a lot from everyone and it has helped me tremendously.

I feel that have made a lot of friends in the five years at Michigan, especially with my colleagues working in Chen lab. To Dr. Jesse Zhang, Dr. Yuwei Liu, Dr. Lauren Soblosky and Dr. Bei Ding, you have been an inspiration to me. Every moment has been a pleasure and I thank you all for your friendship, kindness, and making our time very special. You all hold a place in my heart, I cant thank you enough for the time that we have spent together. As for the past and present members of Chen Lab, It was a pleasure working with you all. I thank you for making the most of every day, for teaching me patience for my work, giving me guidance, and letting me know that you always support me.

Finally, I would like to thank my family and friends for their unconditional support and encouragement. I am incredibly lucky to have such loving parents and brother who I always look to for support, and appreciate all that they've done for me. Thank you for everything.

Table of Contents

List of Figures

Abstract

To date, many of the current tools and technologies used to explore biophysical processes and phenomena are limited in part by their inability to probe without external perturbation. Factors such as size restrictions, samples used for non-terminal studies, and small molecule dynamics cannot be addressed by these techniques. This has not only driven the field of noninvasive analytics, but has had a direct impact on shaping the next generation of biological and clinical assays. Highlights of my thesis work herein focus on the development of nonlinear optical spectroscopy and imaging modalities, sum frequency generation (SFG) spectroscopy and coherent anti-Stokes Raman scattering (CARS) microscopy. Each has their own unique qualities that make them ideal as noninvasive tools and techniques.

Using these two techniques, my studies address fundamental questions about: (1) the orientation and behavior of chemically immobilized peptides on abiotic surfaces for the rational design of improved biosensors and bioactive textiles, (2) understanding the relations between cytosolic lipids, cellular energy homeostasis/consumption, and developmental biology in female reproductive cells, and (3) the ability to classify and measure male reproductive health as it relates to acrosome integrity.

Results from SFG, a surface-sensitive spectroscopy, demonstrate that surface tethering

mechanisms govern both the orientation and activity of antimicrobial peptide MSI-78 on surfaces. Attachment of the n-terminus of this peptide results in an orientation perpendicular to the surface normal (lying down) whereas c-terminus attachment leads to a parallel orientation (standing up). Other methods complementary to SFG including circular dichroism (CD) spectroscopy and coarse-grained simulation molecular dynamics simulations also support this conclusion. Antimicrobial activity on the other hand is higher for n-terminally attached MSI-78.

In reproductive biology, lipids demonstrate a unique purpose. Unlike somatic cells, which use sugar substrates as a primary source of energy, oocytes utilize lipids as a supplementary source of energy. CARS microscopy is used to evaluate the contributions of lipid in oocyte growth, development, and for metabolic disease. Results show that lipid content fluctuates as oocytes progress through meiosis, indicated by an increase in content as the oocytes grow and a decrease as oocytes resume meiosis. As for male reproductive cells, CARS microscopy is beginning to be used for the identification of acrosome reaction, an important predictor of male infertility.

Results of this research have impact in areas such as bio-based functionalization of sensors or textiles, clinical infertility therapies, and reproductive biology as a whole. The development of such techniques is essential for a new generation of noninvasive assays.

CHAPTER 1: Introduction

1.1 Motivation – Importance of the Noninvasive Measurement

Developments in modern spectroscopies and microscopies have revolutionized the way we are able to see and interpret the world around us. Research in biology, medicine, and materials science has seen a huge impact in the development of new equipment and analysis methods. For example, the invention of the light microscope in the 16^{th}-17^{th} century, vacuum pump in the 18^{th} century, vacuum phototubes in 1934, and the laser in 1959 have allowed for unparalleled sensitivity to “watch” the smallest features and to “detect” the weakest signals. From these technologies, a wealth of new techniques have emerged, and for the majority of these, have become standards in laboratories of all disciplines.

Optical microscopy has been an influential technology for the progression of biological research. What was once an invisible world of cells, organelles, and biomolecules became a quest for science to understand functional roles of many biological systems. Despite its simplicity, optical microscopes provide sub-micron spatial resolution and generally have a relaxed requirement on sample conditions. Its contrast mechanism is the transmission or reflectivity of the sample, which is difficult for most biological samples where overall transmission is often very high.

Because of this, histological staining methods using artificial dyes were developed [1]. Staining yields a strong image contrast and allows for the specific visualization of microscopic structures based on their molecular composition, making them a good tool for visualization of subcellular locations. Unfortunately, however, staining sacrifices noninvasiveness, which is one of the main advantages of optical microscopy and crucially important in many live cell conditions.

This problem initiated the development of optical microscopy techniques that provide contrast without the necessity to compromise the sample with cellular fixation or staining. Such an advantage is exactly provided by phase contrast microscopy and differential interference contrast microscopy [2], where both methods rely on small differences in the refractive index of the sample. These phase shifts, which are observed after the excitation light has transversed the sample, are used to generate image contrast. From this mechanism it is clear that neither of these two techniques are chemically selective.

It was the discovery of green fluorescent protein (GFP) [3-6] and its variants that lead to the idea of genetically-encoded fluorescence labeling. By the expression of a fusion protein composed of a fluorescent protein with a target protein in living cells and organisms, ultimate specificity can be achieved: proteins can now be tracked by monitoring the fluorescence of the fluorescent protein. However, fusion with a fluorescent protein may lead to major changes in the physiological properties of a target, phototoxicity to the sample, or photobleaching of the fluorescent protein. Despite

the overwhelming success of the techniques listed above, it is imperative that methods still be developed with the goal of minimal invasiveness and the ability to gain maximum information

Noninvasiveness is of pivotal importance for many studies, e.g., live cells in nonterminal studies where cellular fixation is counterproductive and small molecule dynamics where fluorophore size limits molecular behavior. New frontiers of disease detection, biochemistry, and cell biology demand the ability to visualize the molecular identity in complex systems in real time. Therefore, the development of tools and techniques for noninvasive analytics is paramount.

The aim of this thesis, and the work presented herein, is to present new modalities that preserve the noninvasive measurement with chemical sensitivity. These nonlinear optical techniques, sum frequency generation (SFG) spectroscopy and coherent anti-Stokes Raman scattering (CARS) microscopy, are tools that generate molecular specific contrast based on the vibrational spectra of the sample molecules. These analytical techniques can provide important molecular level insight as well as biological significance of cellular macromolecules and have found important applications in material and biological sciences, as well as related research fields. Thanks to the fast development of laser technologies, nonlinear vibrational spectroscopies and microscopies have emerged and were developed into powerful analytical tools for modern science and technology.

1.2 Sum Frequency Generation (SFG) Spectroscopy

In this section, a brief overview of SFG, the experimental system setup used in this thesis, and basic SFG theory, are discussed.

1.2.1 Basic SFG Overview.

SFG is a second order nonlinear optical process. It occurs when two pulsed laser beams, one with a tunable IR frequency ω_{IR}, and the other with a fixed visible frequency ω_{vis}, spatially and temporally overlap at an interface. A signal is generated at a specific direction given by phase matching conditions with a frequency $\omega_{SFG} = \omega_{IR} + \omega_{vis}$. The intensity of this sum frequency beam is resonantly enhanced when the tunable IR frequency matches a vibrational transition of a molecule. Therefore, when SFG signal intensity plotted against the input IR frequency, the resonant signal collected provides a vibrational spectrum. SFG can provide molecular level structural information because molecular vibrational modes are fingerprints of molecules. In SFG, an SFG vibrational spectrum is obtained by detecting SFG signal intensity at each IR input frequency and continuously tuning the IR frequency.

SFG has several advantages over other surface sensitive techniques, making it unique in examining molecular structures of many surfaces or interfaces involving biomolecules.

Among other surface sensitive techniques such as X-ray photoelectron spectroscopy (XPS) and secondary ion mass spectrometry (SIMS), these spectroscopies are capable

of determining the elemental composition and functional groups of a surface (often only to a depth of 10 nm below the surface) [7-11]. Its ability for surface analysis is complicated by the fact that both techniques require high vacuum to operate and cannot be used to study many biological interfaces, which involve aqueous media. AFM is a high-resolution scanning probe microscopy, which uses a sharp tip to interact with a sample surface [12,13]. AFM can provide a three-dimensional surface profile without the need for sample pretreatment or high vacuum environment. However, it is difficult for AFM to measure molecular structures or to probe buried solid/solid interfaces. SPR is a laser based interfacial sensitive technique which can study buried interfaces *in situ*. It is sensitive to local refractive index changes at a thin metal film surface due to the adsorption of various materials such as biomolecules or nanoparticles to the surface [13,14]. A linear relationship is often observed between the adsorbed mass and the resulting refractive index change in the SPR experiment, which can then be used in a variety of biosensor applications. Ellipsometry is an optical technique used to study thin film dielectric properties [15]. The change of polarization of polarized input light is measured after interaction with the sample. Although both SPR and ellipsometry can provide *in situ* measurements, they cannot provide molecular structural information.

Vibrational spectroscopies on the other hand, can provide molecular structural information about surfaces and interfaces. For example, molecular composition, orientation, and time dependent dynamics at surfaces can be studied by using infrared light to characterize intrinsic vibrational modes of surface molecules. One important surface vibrational spectroscopy is attenuated total-internal reflectance-Fourier

transform infrared (ATR-FTIR) spectroscopy [16-18]. The surface selectivity of ATR-FTIR is provided by the penetration depth of the evanescent wave, which has the same order of magnitude as the IR wavelength. By applying different polarized incident light beams, interfacial molecular orientations can be derived in ATR-FTIR measurements. However, the surface sensitivity of ATR-FTIR is poor; sometimes in order to probe surface/interfacial structures, it is necessary to subtract large signal contribution from the bulk media. Another surface specific vibrational technique is surface-enhanced Raman spectroscopy (SERS), which enhances the Raman scattering signal of molecules adsorbed on rough metal substrates (usually gold or silver) [13,19,20]. The enhancement factor can be as high as 10^{14}~10^{15} which allows SERS to detect single molecules [20]. However, it is difficult to apply SERS to study other surfaces and interfaces. Buried solid/solid interfaces in particular are difficult to study using above surface sensitive techniques.

SFG can probe interfaces that are accessible to laser light. More importantly, the selection rule for this second order nonlinear process (which will be discussed in the next part) indicates SFG has intrinsic sub-monolayer interfacial selectivity [21-26]. It has been extensively shown that SFG can provide *in situ* measurements on buried interfaces in real time. By applying different polarization combinations of the input/output laser beams, SFG can also be used to determine molecular orientations at interfaces [27-31]. SFG experiments do not require high vacuum to perform (as in XPS and SIMS experiments). Compared to AFM, SPR, and ellipsometry techniques, vibrational spectroscopic signatures can provide more detailed molecular structural information on

surfaces. SFG spectroscopy also provides *in situ* measurement of molecular presence and orientation with great sensitivity at buried interfaces, which cannot be obtained using ATR-FTIR or SERS techniques.

1.2.2 SFG Selection Rule.

The interfacial sensitivity of SFG is defined by its selection rule, which is different from linear vibrational spectroscopy (e.g. IR or Raman spectroscopy). SFG is a second order nonlinear optical process in which the signal intensity is proportional to the square of the second order nonlinear optical susceptibility of the material $\chi^{(2)}$ under the electric dipole approximation. $\chi^{(2)}$ is a third rank tensor which changes sign under inversion operation: $\chi^{(2)}(-r) = -\chi^{(2)}(r)$ [32,33]. For materials with inversion symmetry, the relation $\chi^{(2)}(-r) = \chi^{(2)}(r)$ holds. Comparing these two relations, we know $\chi^{(2)}(r) = 0$. This

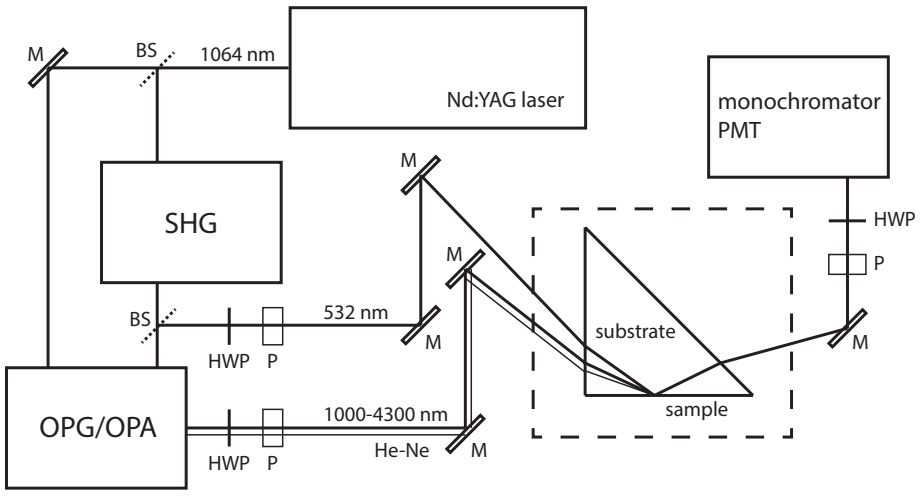

Figure 1.1: SFG Experimental Design. M: mirror, BS: beam splitter, HWP: half-wave plate, P: polarizer, SHG: second-harmonic generation, OPG/OPA: optical parametric generation/optical parametric amplification, HeNe: Helium-Neon laser.

Adapted from http://www.ekspla.com

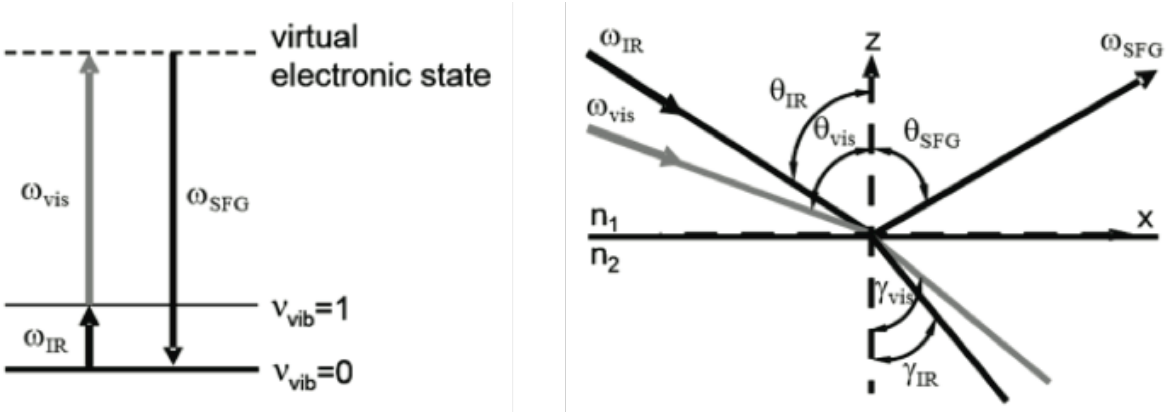

Figure 1.2: SFG Fundamentals. Left: Co-Propagating Non-Collinear SFG Experimental Geometry. The reflected infrared and visible beams and transmitted beams have been omitted for clarity. Right: Schematic of the SFG energy diagram which involves both IR and Raman transitions.

---

demonstrates that no SFG signal will be generated if the material has inversion symmetry under the electric dipole approximation. SFG signal can only be generated from a medium with no inversion symmetry. Most bulk materials have inversion symmetry and therefore do not generate SFG signal. However, at surfaces or interfaces where the centro-symmetry is broken, $\chi^{(2)}(-r) \neq \chi^{(2)}(r)$, so the SFG process can occur. In the systems studied in this thesis, signals contributed from surfaces or interfaces dominate the SFG spectra and bulk signal usually can be neglected.

1.2.3 SFG Experimental Setup.

The SFG system layout is shown in **Fig 1.1**. The SFG spectrometer used here (EKSPLA, Vilnius, Lithuania) is composed of a pico-second Nd:YAG laser, a harmonic unit, an optical parametric generation (OPG)/amplification (OPA)/difference frequency generation (DFG) system, and a detection system. The visible beam (532 nm) is generated by frequency-doubling the fundamental output pulses of 20 ps pulsewidth from the Nd:YAG laser. OPG and OPA can generate a signal beam (420 to 680 nm)

and an idler beam (740 to 2300 nm). The idler beam and the 1064 nm pump beam are used in DFG to generate a frequency tunable mid-IR beam (1000 cm^{-1} to 4300 cm^{-1}). For SFG experiments, the input visible and IR pulse energies are ~30 μJ and ~100 μJ, respectively. The pulses were overlapped at the sample surface or interface spatially and temporarily to generate the sum frequency signal beam. The incident angles of the visible and the IR input beams are 50° and 55° versus the surface normal, respectively. The SFG signal from the surface is collected by a photomultiplier tube (PMT) attached to a monochromator.

A schematic of the general SFG experimental geometry and the SFG energy diagram are shown in **Fig 1.2**.

1.2.4 Basic SFG Theory.

The theoretical background of SFG has been developed in earlier publications [27]. New SFG data analysis methods have also been developed [21,29,34,35].

In short, SFG signal intensity can be expressed as:

$$I_{SFG} \propto \left|\chi_{eff}^{(2)}\right|^2 I_{IR} I_{vis} \tag{1.1}$$

Here I_{IR} and I_{vis} are intensities of the input IR and visible beams, respectively. $\chi_{eff}^{(2)}$ is the effective second order nonlinear optical susceptibility, which can be expressed as the sum of a nonresonant term and a resonant term:

$$\chi_{eff}^{(2)} = \chi_{NR}^{(2)} + \sum_q \frac{A_q}{\omega_{IR} - \omega_q + i\Gamma_q} \tag{1.2}$$

Here $\chi_{NR}^{(2)}$ is the nonresonant contribution from the sample. The resonant contribution can be modeled as the sum of Lorentzians with signal strength or amplitude A_q, frequency ω_q, and linewidth Γ_q. **Equation (1.2)** can be used to fit SFG spectrum in the experiment to obtain quantitative vibrational strength comparisons of different functional groups.

For an isotropic interface in the x-y plane, the effective second order nonlinear optical susceptibility components can be related to the second order nonlinear optical susceptibility components of the sample in the lab-fixed coordinating system:

$$\chi_{eff,ssp}^{(2)} = L_{yy}(\omega_{SF})L_{yy}(\omega_{vis})L_{zz}(\omega_{IR})\sin\theta_{IR}\cdot\chi_{yyz}^{(2)} \tag{1.3}$$

$$\chi_{eff,sps}^{(2)} = L_{yy}(\omega_{SF})L_{zz}(\omega_{vis})L_{yy}(\omega_{IR})\sin\theta_{vis}\cdot\chi_{yzy}^{(2)} \tag{1.4}$$

$$\chi_{eff,pss}^{(2)} = L_{zz}(\omega_{SF})L_{yy}(\omega_{vis})L_{yy}(\omega_{IR})\sin\theta_{SFG}\cdot\chi_{zyy}^{(2)} \tag{1.5}$$

$$\begin{aligned}\chi_{eff,ppp}^{(2)} = &-L_{xx}(\omega_{SF})L_{xx}(\omega_{vis})L_{zz}(\omega_{IR})\cos\theta_{SFG}\cos\theta_{vis}\sin\theta_{IR}\cdot\chi_{xxz}^{(2)}\\ &-L_{xx}(\omega_{SF})L_{zz}(\omega_{vis})L_{xx}(\omega_{IR})\cos\theta_{SFG}\sin\theta_{vis}\cos\theta_{IR}\cdot\chi_{xzx}^{(2)}\\ &+L_{zz}(\omega_{SF})L_{xx}(\omega_{vis})L_{xx}(\omega_{IR})\sin\theta_{SFG}\cos\theta_{vis}\cos\theta_{IR}\cdot\chi_{zxx}^{(2)}\\ &+L_{zz}(\omega_{SF})L_{zz}(\omega_{vis})L_{zz}(\omega_{IR})\sin\theta_{SFG}\sin\theta_{vis}\sin\theta_{IR}\cdot\chi_{zzz}^{(2)}\end{aligned} \tag{1.6}$$

In these expressions, $\chi_{IJK}^{(2)}(IJK = x,y,z)$ is a local nonlinear second order optical susceptibility component of the material at the interface defined in the lab-fixed coordinate frame. θ_{IR} and θ_{vis} are the incident angles of the input IR and visible beams vs. the surface normal, respectively. The angle θ_{SFG} is the output angle of SFG signal vs. the surface normal. $L_{ii}(i = x,y,z)$ is the Fresnel coefficient which is a function of beam input angles and the refractive indices of materials forming the interface. ω_{SF}, ω_{vis}

and ω_{IR} are frequencies of the sum frequency beam, the visible beam and the IR beam, respectively. Moreover, ssp, sps, pss, and ppp are different polarization combinations of SFG measurement ('ssp' indicates s-polarized signal, s-polarized visible beam, and p-polarized IR beam).

$L_{xx}(\omega)$, $L_{yy}(\omega)$, and $L_{zz}(\omega)$ are the Fresnel coefficients for beam ω given by:

$$L_{xx}(\omega) = \frac{2n_1(\omega)\cos\gamma}{n_1(\omega)\cos\gamma + n_2(\omega)\cos\theta},$$
$$L_{yy}(\omega) = \frac{2n_1(\omega)\cos\theta}{n_1(\omega)\cos\theta + n_2(\omega)\cos\gamma}, \qquad (1.7)$$
$$L_{zz}(\omega) = \frac{2n_2(\omega)\cos\theta}{n_1(\omega)\cos\gamma + n_2(\omega)\cos\theta}\left(\frac{n_1(\omega)}{n'(\omega)}\right)^2$$

where $n'(\omega)$ is the refractive index of the interfacial layer, θ is the incident angle of the beam in consideration, and γ is the corresponding refracted angle satisfies:

$$n_1(\omega)\sin\theta = n_2(\omega)\sin\gamma.$$

The measured SFG second order nonlinear optical susceptibility components defined in the lab-fixed coordination system can be related to the molecular hyperpolarizability components through molecular orientations considering the coordinate transformation.

$$\chi^{(2)}_{IJK} = N\sum_{IJK=x,y,z}\left\langle R_{Ii}R_{Jj}R_{Kk}\right\rangle\beta^{(2)}_{ijk} \qquad ijk = a,b,c \qquad (1.8)$$

In this expression, N is the surface number density. R is the transformation matrix from the molecular frame (a,b,c) to the lab frame (x,y,z). $\beta^{(2)}_{ijk}$ is the hyperpolarizability component. The angle brackets here mean ensemble average, indicating that the macroscopic susceptibility is the ensemble average of the hyperpolarizability of each molecule projected to the lab frame multiplied by the total molecule density and divided

by vacuum permittivity. R is usually a function of three angles, azimuthal angle ϕ, twist angle ψ, and tilt angle θ. Therefore, we have:

$$\chi_{IJK}^{(2)} = N \sum_{IJK=x,y,z} f(\phi,\psi,\theta)\beta_{ijk}^{(2)} \qquad ijk = a,b,c \tag{1.9}$$

For an isotropic surface, the azimuthal angle can be averaged between 0 to 2π. Then the expression is reduced to

$$\chi_{IJK}^{(2)} = N \sum_{IJK=x,y,z} f(\psi,\theta)\beta_{ijk}^{(2)} \qquad ijk = a,b,c \tag{1.10}$$

If the distribution of twist angle is considered to be random, then

$$\chi_{IJK}^{(2)} = N \sum_{IJK=x,y,z} f(\theta)\beta_{ijk}^{(2)} \qquad ijk = a,b,c \tag{1.11}$$

The resonant part of $\beta_{ijk}^{(2)}$ is directly proportional to the product of the IR dipole derivative and the Raman polarizability derivative of the vibrational mode Q as described below:

$$\beta_{ijk}^{(2)} \propto \frac{\partial \alpha_{ij}}{\partial Q}\frac{\partial \mu_k}{\partial Q} \tag{1.12}$$

Therefore, only those vibrational modes that are both IR-active and Raman-active will be SFG-active.

1.3 Limitations of SFG

SFG measurements offer the ability to probe changes in molecular orientation and conformation with high surface sensitivity, and without the need for rigorous background subtraction. However, due to the relations that govern observed signal intensities (as shown in **Equation 1.9**), it is not always directly possible to distinguish changes in orientation from interfacial number density: a dense layer of molecules lying parallel to

the surface might yield no signal [36].

Also, SFG can only provide a limited number of experimental measurements. For complicated situations, more assumptions or combination of SFG and other supplemental techniques are needed [37,38]. Furthermore, although the amide I band is somewhat sensitive to changes in protein secondary structure, small changes in protein conformation may not be detectable within the limited resolution of our spectrometer. A more detailed picture of protein structure may be obtained using computational methods such as molecular dynamics simulations.

1.4 Coherent Anti-Stokes Raman Scattering (CARS) Microscopy

In this section, a brief overview of CARS, its implementation, and methods for background subtraction, are discussed. Because the technical design is discussed in **Chapter 3**, it will be omitted here.

1.4.1 Brief Overview of CARS.

Coherent anti-Stokes Raman scattering (CARS) is a four wave mixing (FWM) process which probes the third order nonlinearity of molecules. **Fig.1.3** (a) is the energy level diagram of CARS. If the frequency difference $\omega_1 - \omega_2$ matches the molecule vibration frequency, the two input fields can provide a coherent driving force to all the molecules within the beam path, modulating the material's polarizability. A third field ω_3 probes the modulated polarizability and generates blue shifted light. The photo damage of UV light and the low resolution and detection efficiency of IR light are all circumvented by CARS,

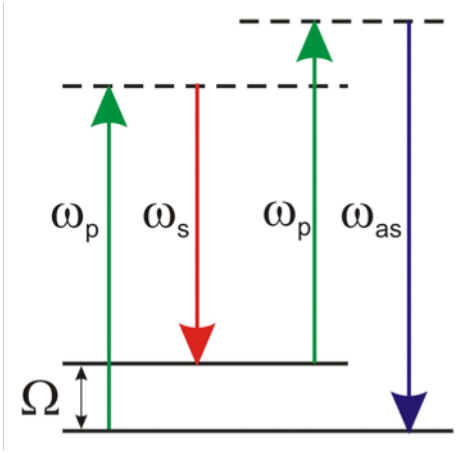

Figure 1.3: CARS Energy Level Diagram. Photons transition through virtual states. The resulting parametric process scatters light with vibrational information encoded.

---

which uses near IR pulsed light sources. In addition, the vibration of the molecules is synchronized. Thus the electromagnetic signal field adds up coherently, in contrast to the incoherent intensity summation in spontaneous Raman scattering.

The blue shifted light (anti-Stokes signal) is used in microscopy and therefore eliminates background due to one-photon fluorescence. However, CARS is not background free. The NR signal will be discussed further in **Section 1.3.3**.

CARS spectroscopy was first demonstrated in 1965 [39]. Since its initial demonstration, CARS has become a widely adopted method, finding application in physics, chemistry, and material science [40-46].

1.4.2 Implementation of CARS Microscopy.

With the development of pulsed laser technology, tunable picosecond mode-locked lasers became available. In the early 80's, visible picosecond dye lasers were employed

for CARS microscopy [47]. This light source was not ideal for biological samples due to the presence of two-photon resonances, which presented as strong NR background. In addition, the non-collinear beam geometry in this experiment prevented high spatial resolution imaging.

It was not until the late 90's [48] that near-IR pico-second solid state pulsed light sources were used for imaging biological samples. Near-IR pulsed sources were a much better tool than visible light sources for three reasons: first, Rayleigh scattering is significantly reduced which increased the penetration depth of light; second, NR signal is reduced for longer wavelength, therefore weakening the NR contribution; third there is less photo damage at longer wavelengths. This system, although an improvement on its previous generation, was constructed with two electronically synchronized lasers. Temperature fluctuations and electronic walk off were often a problem for such designs.

A simpler and more robust method than this early implementation is to use a single pulsed source to generate light of different colors. This way the timing jitter is negligible. One commonly used nonlinear optics technique is optical parametric generation (OPG) or the use of a photonic crystal fiber. Both of these techniques are discussed in **Chapters 3** and **5**, respectively.

1.5 Limitations of CARS

Despite the major advantages previously described, CARS as a technique has not been widely accepted in biomedical research. As compared to other microscopic techniques

such as phase contrast, staining, or fluorescence labeling, CARS does not allow for straightforward image interpretation due to the difficulties associated with non-resonant background signal.

Non-resonance signal arises from the electronic response of the material sample, is independent of vibrational resonances, and for the most part, wavelength independent. The overall sample response is proportional to the third-order nonlinear optical susceptibility, or $\chi_{eff}^{(3)}$, comprised of both a resonant (R) and nonresonant (NR) term. This susceptibility takes the form:

$$\chi_{eff}^{(3)} = \left(\chi_{\mathrm{R}}^{(3)} + \chi_{\mathrm{NR}}^{(3)} \right) \tag{1.13}$$

$$I_{\mathrm{CARS}} \propto \left(\chi_{eff}^{(3)} \right)^2 \tag{1.14}$$

Because of the mixed terms in this expansion (**Equation 1.14**), background signal cannot be easily subtracted as in linear spectroscopies/microscopies.

For multiplex CARS, the NR signal increases signal background and also distorts the spectral lineshape. It requires spectral fitting to make numerical corrections. Also, based on the difference between the NR signal and the resonant signal, a few optical techniques have been applied to suppress the NR signal.

One method of background suppression is based on polarization discrimination of the anti-Stokes signal. This method works very well in spectroscopy for studying samples in liquid form [49]. For biomedical applications, the NR signal generated may not have a

fixed polarization, and the scattering inside the sample can often distort the polarization and cause errors in measurement.

One other difference between the NR signal and the resonant signal is the time scale of the response function. The NR signal originates from electron's motion which is much faster than nuclear motion (Raman signal). If the time response function can be directly measured, the two signal components can be easily separated from each other. With sub 20 fs pulses, the Raman modes within the fingerprint regime can be directly time resolved [50,51].

Recent research has implemented the use of algorithms to remove nonresonant contributions after data is collected; the most common are a modified Kramers-Krönig transform [52], as well as maximum entropy method [53]. Both methods aim to isolate the imaginary portion of the resonant signal in CARS. This signal is functionally identical to the spontaneous Raman lineshape and, more importantly, is linear with concentration.

1.6 Presented Research

In this thesis, both SFG and CARS will be used in developing methods for noninvasive measurements in biological applications. Presented in **Chapter 2**, I will examine the behavior of surface-bound peptides with SFG as well as complimentary techniques including circular dichroism (CD) spectroscopy, molecular dynamics simulations, and antibacterial activity tests. In applications ranging from pathogen detection and

elimination, to biomolecule-based biosensors, an understanding of how peptides interact when chemically bound to a surface is important in designing materials with better performance, or biomolecules with maximum activity.

In the remaining three chapters (**Chapter 3**, **4**, and **5**), I will discuss the implementation of CARS in noninvasive biological imaging. Since most of my thesis work was dedicated to the development of this technique, and analysis methods to compliment it, those will be discussed primarily in **Chapter 3**. Broadband CARS has been an ideal tool in its ability to generate hyperspectral data. This data contains chemical information of a variety of different functional groups within one image. In order to identify such chemical species, singular value decomposition (SVD) was also implemented for this research. SVD was the best solution since it was able to uniquely identify different chemistries even with low-quality images.

With this developed CARS system, I addressed the biological significance of lipids in reproductive biology. In **Chapter 4**, I investigate the ability for CARS to accurately identify lipid droplets in live oocytes, or female reproductive cells. These cells, unlike the majority of somatic cells, have applications in clinical diagnostics where fixation is impractical. Therefore, CARS must have utility in assessing lipid for nonterminal studies and be able to help make objective decisions to maximize reproductive outcomes.

Finally, in **Chapter 5**, I will begin to assess CARS for its ability to identify acrosome reaction (AR) in human sperm cells. The noninvasive nature of CARS makes it an ideal

candidate for the development of a clinical assay to identify AR. This reaction, along with capacitation, give sperm a biological advantage (albeit necessary) for successful fertilization. A lack of sperm capacitation, or improper timing of AR is one of many factors that cause male infertility. Outcomes of this research have important clinical impact for the identification of AR, and the subsequent projected increase in successful pregnancies.

In summary, the chapters which will be presented in this thesis show my research effort in the development of nonlinear optical methods, especially SFG and CARS, and their ability to shape the next generation of noninvasive analytics.

1.7 References

[1] Gavrieli, Y.; Sherman, Y.; Ben-Sasson, S.A. Identification of Programmed Cell Death *In Situ* Via Specific Labeling of Nuclear DNA Fragmentation. *J Cell Biol*, **1992**, *119*, 493–501.

[2] Kimmel, C.B.; Ballard, W.W.; Kimmel, S.R.; Ullmann, B.; Schilling, T.F. Stages of Embryonic Development of the Zebrafish. *Dev Dyn*, **1995**, *203*, 253–310.

[3] Heim, R.; Cubitt, A.B.; Tsien, R.Y. Improved Green Fluorescence. *Nature*, **1995**, *373*, 663–664.

[4] Miyawaki, A.; Llopis, J.; Heim, R.; McCaffery, J.M.; Adams, J.A.; Ikura, M.; Tsien, R.Y. Fluorescent Indicators for Ca^{2+} Based on Green Fluorescent Proteins and Calmodulin. *Nature*, **1997**, *388*, 882–887.

[5] Ormö, M.; Cubitt, A.B.; Kallio, K.; Gross, L.A.; Tsien, R.Y.; Remington, S.J. Crystal Structure of the *Aequorea Victoria* Green Fluorescent Protein. *Science*, **1996**, *273*, 1392–1395.

[6] Tsien, R.Y. The Green Fluorescent Protein. *Annu Rev Biochem*, **1998**, *67*, 509–544.

[7] McArthur, S.L. Applications of XPS in Bioengineering. *Surf Interface Anal*, **2006**, *38*, 1380–1385.

[8] Roach, P.; Parker, T.; Gadegaard, N.; Alexander, M.R. Surface Strategies for Control of Neuronal Cell Adhesion: a Review. *Surf Sci Rep*, **2010**, *65*, 145–173.

[9] Benninghoven, A. Developments in Secondary Ion Mass Spectroscopy and Applications to Surface Studies. *Surf Sci*, **1975**, *1*, 596–625.

[10] Henry, M.; Dupont-Gillain, C.; Bertrand, P. Conformation Change of Albumin Adsorbed on Polycarbonate Membranes as Revealed by ToF-SIMS. *Langmuir*, **2003**, *19*, 6271–6276.

[11] Baugh, L.; Weidner, T.; Baio, J.E.; Nguyen, P.-C.T.; Gamble, L.J.; Stayton, P.S.; Castner, D.G. Probing the Orientation of Surface-Immobilized Protein G B1 Using ToF-SIMS, Sum Frequency Generation, and NEXAFS Spectroscopy. *Langmuir*, **2010**, *26*, 16434–16441.

[12] Hessler, J.A.; Budor, A.; Putchakayala, K.; Mecke, A.; Rieger, D.; Banaszak Holl, M.M.; Orr, B.G.; Bielinska, A.; Beals, J.; Baker, J., Jr. Atomic Force Microscopy Study of Early Morphological Changes During Apoptosis. *Langmuir*, **2005**, *21*, 9280–9286.

[13] Wark, A.W.; Lee, J.; Kim, S.; Faisal, S.N.; Lee, H.J. Bioaffinity Detection of Pathogens on Surfaces. *J Ind Eng Chem*, **2010**, *16*, 169–177.

[14] Cambell, C.T.; Kim, G. SPR Microscopy and Its Applications to High-Throughput Analyses of Biomolecular Binding Events and Their Kinetics. *Biomaterials*, **2007**, *28*, 2380–2392.

[15] Santos, O.; Kosoric, J.; Hector, M.P.; Anderson, P.; Lindh, L. Adsorption Behavior of Statherin and a Statherin Peptide Onto Hydroxyapatite and Silica Surfaces by *In Situ* Ellipsometry. *J Colloid Interface Sci*, **2008**, *318*, 175–182.

[16] Sharon, M.; Oren, Z.; Shai, Y.; Anglister, J. 2D-NMR and ATR-FTIR Study of the Structure of a Cell-Selective Diastereomer of Melittin and Its Orientation in Phospholipids. *Biochemistry*, **1999**, *38*, 15305–15316.

[17] Chittur, K.K. FTIR/ATR for Protein Adsorption to Biomaterial Surfaces. *Biomaterials*, **1998**, *19*, 357–369.

[18] Schartner, J.; Güldenhaupt, J.; Mei, B.; Rögner, M.; Muhler, M.; Gerwert, K.; Kötting, C. Universal Method for Protein Immobilization on Chemically Functionalized Germanium Investigated by ATR-FTIR Difference Spectroscopy. *J Am Chem Soc*, **2013**, *135*, 4079–4087.

[19] Wen, Z.-Q.; Li, G.; Ren, D. Detection of Trace Melamine in Raw Materials Used for Protein Pharmaceutical Manufacturing Using Surface-Enhanced Raman Spectroscopy (SERS) with Gold Nanoparticles. *Appl Spectrosc*, **2011**, *65*, 514–521.

[20] Chen, J.-W.; Liu, X.-P.; Feng, K.-J.; Liang, Y.; Jiang, J.-H.; Shen, G.-L.; Yu, R.-Q. Detection of Adenosine Using Surface-Enhanced Raman Scattering Based on Structure-Switching Signaling

Aptamer. *Biosens Bioelectron*, **2008**, *24*, 66–71.

[21] Wang, J.; Even, M.A.; Chen, X.; Schmaier, A.H.; Waite, J.H.; Chen, Z. Detection of Amide I Signals of Interfacial Proteins *In Situ* Using SFG. *J Am Chem Soc*, **2003**, *125*, 9914–9915.

[22] Chen, X.; Wang, J.; Sniadecki, J.J.; Even, M.A.; Chen, Z. Probing A-Helical and B-Sheet Structures of Peptides at Solid/Liquid Interfaces with SFG. *Langmuir*, **2005**, *21*, 2662–2664.

[23] Roy, S.; Covert, P.A.; FitzGerald, W.R.; Hore, D.K. Biomolecular Structure at Solid–Liquid Interfaces as Revealed by Nonlinear Optical Spectroscopy. *Chem Rev*, **2014**, *114*, 8388–8415.

[24] Fu, L.; Liu, J.; Yan, E.C.Y. Chiral Sum Frequency Generation Spectroscopy for Characterizing Protein Secondary Structures at Interfaces. *J Am Chem Soc*, **2011**, *133*, 8094–8097.

[25] Han, X.; Uzarski, J.R.; Mello, C.M.; Chen, Z. Different Interfacial Behaviors of N- and C-Terminus Cysteine-Modified Cecropin P1 Chemically Immobilized Onto Polymer Surface. *Langmuir*, **2013**, *29*, 11705–11712.

[26] Li, Y.; Wei, S.; Wu, J.; Jasensky, J.; Xi, C.; Li, H.; Xu, Y.; Wang, Q.; Marsh, E.N.G.; Brooks, C.L., III; Chen, Z. Effects of Peptide Immobilization Sites on the Structure and Activity of Surface-Tethered Antimicrobial Peptides. *J Phys Chem C*, **2015**, *119*, 7146–7155.

[27] Zhuang, X.; Miranda, P.B.; Kim, D.; Shen, Y.R. Mapping Molecular Orientation and Conformation at Interfaces by Surface Nonlinear Optics. *Phys Rev B*, **1999**, *59*, 12632–12640.

[28] Nguyen, K.T.; Le Clair, S.V.; Ye, S.; Chen, Z. Molecular Interactions Between Magainin 2 and Model Membranes *In Situ*. *J Phys Chem B*, **2009**, *113*, 12358–12363.

[29] Nguyen, K.T.; Le Clair, S.V.; Ye, S.; Chen, Z. Orientation Determination of Protein Helical Secondary Structures Using Linear and Nonlinear Vibrational Spectroscopy. *J Phys Chem B*, **2009**, *113*, 12169–12180.

[30] Yang, P.; Glukhova, A.; Tesmer, J.J.G.; Chen, Z. Membrane Orientation and Binding Determinants of G Protein-Coupled Receptor Kinase 5 as Assessed by Combined Vibrational Spectroscopic Studies. *PLoS ONE*, **2013**, *8*, e82072–11.

[31] Yang, P.; Ramamoorthy, A.; Chen, Z. Membrane Orientation of MSI-78 Measured by Sum Frequency Generation Vibrational Spectroscopy. *Langmuir*, **2011**, *27*, 7760–7767.

[32] Shen, Y.R. Surface Properties Probed by Second-Harmonic and Sum-Frequency Generation. *Nature*, **1989**, *337*, 519–525.

[33] Chen, Z.; Shen, Y.R.; Somorjai, G.A. Studies of Polymer Surfaces by Sum Frequency Generation Vibrational Spectroscopy. *Annu Rev Phys Chem*, **2002**, *53*, 437–465.

[34] Kim, J.; Cremer, P.S. Elucidating Changes in Interfacial Water Structure Upon Protein Adsorption. *ChemPhysChem*, **2001**, *2*, 543–546.

[35] Ye, S.; Nguyen, K.T.; Chen, Z. Interactions of Alamethicin with Model Cell Membranes Investigated Using Sum Frequency Generation Vibrational Spectroscopy in Real Time *In Situ*. *J Phys Chem B*, **2010**, *114*, 3334–3340.

[36] Clarke, M.L.; Wang, J.; Chen, Z. Conformational Changes of Fibrinogen After Adsorption. *J Phys Chem B*, **2005**, *109*, 22027–22035.

[37] Wang, J.; Paszti, Z.; Even, M.A.; Chen, Z. Measuring Polymer Surface Ordering Differences in Air and Water by Sum Frequency Generation Vibrational Spectroscopy. *J Am Chem Soc*, **2002**, *124*, 7016–7023.

[38] Chen, X.; Wang, J.; Boughton, A.P.; Kristalyn, C.B.; Chen, Z. Multiple Orientation of Melittin Inside a Single Lipid Bilayer Determined by Combined Vibrational Spectroscopic Studies. *J Am Chem Soc*, **2007**, *129*, 1420–1427.

[39] Maker, P.D.; Terhune, R.W. Study of Optical Effects Due to an Induced Polarization Third Order in the Electric Field Strength. *Physical Review*, **1965**, *137*, A801–A818.

[40] Potma, E.O.; Xie, X.S. Detection of Single Lipid Bilayers with Coherent Anti-Stokes Raman

Scattering (CARS) Microscopy. *J Raman Spectrosc*, **2003**, *34*, 642–650.

[41] Cheng, J.-X.; Volkmer, A.; Book, L.D.; Xie, X.S. Multiplex Coherent Anti-Stokes Raman Scattering Microspectroscopy and Study of Lipid Vesicles. *J Phys Chem B*, **2002**, *106*, 8493–8498.

[42] Camp, C.H., Jr; Lee, Y.J.; Heddleston, J.M.; Hartshorn, C.M.; Walker, A.R.H.; Rich, J.N.; Lathia, J.D.; Cicerone, M.T. High-Speed Coherent Raman Fingerprint Imaging of Biological Tissues. *Nat Photonics*, **2014**, *8*, 627–634.

[43] Li, L.; Wang, H.; Cheng, J.-X. Quantitative Coherent Anti-Stokes Raman Scattering Imaging of Lipid Distribution in Coexisting Domains. *Biophys J*, **2005**, *89*, 3480–3490.

[44] Brackmann, C.; Norbeck, J.; Åkeson, M.; Bosch, D.; Larsson, C.; Gustafsson, L.; Enejder, A.M.K. CARS Microscopy of Lipid Stores in Yeast: the Impact of Nutritional State and Genetic Background. *J Raman Spectrosc*, **2009**, *40*, 748–756.

[45] Potma, E.O.; Xie, X.S.; Muntean, L.; Preusser, J.; Jones, D.; Ye, J.; Leone, S.R.; Hinsberg, W.D.; Schade, W. Chemical Imaging of Photoresists with Coherent Anti-Stokes Raman Scattering (CARS) Microscopy. *J Phys Chem B*, **2004**, *108*, 1296–1301.

[46] Paar, M.; Jungst, C.; Steiner, N.A.; Magnes, C.; Sinner, F.; Kolb, D.; Lass, A.; Zimmermann, R.; Zumbusch, A.; Kohlwein, S.D.; Wolinski, H. Remodeling of Lipid Droplets During Lipolysis and Growth in Adipocytes. *J Biol Chem*, **2012**, *287*, 11164–11173.

[47] Duncan, M.D.; Reintjes, J.; Manuccia, T.J. Scanning Coherent Anti-Stokes Raman Microscope. *Opt Lett*, **1982**, *7*, 350–352.

[48] Zumbusch, A.; Holtom, G.R.; Xie, X.S. Three-Dimensional Vibrational Imaging by Coherent Anti-Stokes Raman Scattering. *Phys Rev Lett*, **1999**, *82*, 4142–4145.

[49] Cheng, J.-X.; Book, L.D.; Xie, X.S. Polarization Coherent Anti-Stokes Raman Scattering Microscopy. *Opt Lett*, **2001**, *26*, 1341–1343.

[50] Cui, M.; Skodack, J.; Ogilvie, J.P. Chemical Imaging with Fourier Transform Coherent Anti-Stokes Raman Scattering Microscopy. *Appl Opt*, **2008**, *47*, 5790–5798.

[51] Jurna, M.; Korterik, J.P.; Otto, C.; Herek, J.L.; Offerhaus, H.L. Background Free CARS Imaging by Phase Sensitive Heterodyne CARS. *Opt Express*, **2008**, *16*, 15863–15869.

[52] Liu, Y.; Lee, Y.J.; Cicerone, M.T. Broadband CARS Spectral Phase Retrieval Using a Time-Domain Kramers–Kronig Transform. *Opt Lett*, **2009**, *34*, 1363–1365.

[53] Rinia, H.A.; Bonn, M.; Müller, M.; Vartiainen, E.M. Quantitative CARS Spectroscopy Using the Maximum Entropy Method: the Main Lipid Phase Transition. *ChemPhysChem*, **2007**, *8*, 279–287.

CHAPTER 2: Investigation of Surface Behaviors of Cysteine-Modified Antimicrobial Peptide MSI-78 on Abiotic Surfaces

The content of this chapter will be included into the following reference:

Jasensky J, Li Y, Wei S, Wu J, Buer BC, Han XF, Xi C, Marsh ENG, Brooks CL III, Chen Z. Investigation of Surface Behaviors of Cysteine-Modified Antimicrobial Peptide MSI-78 on Abiotic Surfaces. **2015**, in preparation.

2.1 Introduction

Functionalization of abiotic surfaces with biomolecules create unique biotic/abiotic interfaces which are widely used in many advanced materials. These materials are designed to induce or regulate biological activities and their functions and have been applied extensively in fields ranging from antibiofouling coatings, device engineering, and biosensing [1-5]. While this technology has made advances in several aspects of overall design, functionality of the incorporated biomolecule is often affected; either by enhancement or inhibition [6,7]. In order to tailor the performance of these materials, it is crucial to understand the behaviors and compatibility of bioactive components with their tethering surfaces and factors that govern favorable interactions.

Recently, biocatalysis using enzymes has become a plausible alternative to synthetic catalysts. These enzymes are “greener”, more environmentally sustainable, super specific, extremely effective, and only require very mild reaction conditions [3,8]. Currently, the production costs are typically high and the overall yield is slow. Moreover,

these solution-based enzymes must be recollected and reused which has proven to be difficult [7,9]. In order to enhance the efficiency and reusability of such biocatalysts, the adsorption and immobilization of enzymes on solid substrates have been proven to have promising potential [8]. If these enzymes are chemically tethered to a solid support in a controlled and predictable way, then efficiency can be not only similar to that of enzymes in solution, but can be reusable or easily recycled.

In a similar fashion, the immobilization of peptides to solid surfaces has applications in antibiofouling and pathogen elimination [10,11]. Since biofouling can occur on a variety of surfaces from medical devices to marine ships, understanding and eliminating this saves lives, health care costs, and fuel consumption.

With their high potency, broad range of activity, and strong affinity to various microorganisms, anti-microbial peptides (AMPs) are preferred tethering molecules and have been considered in the development of peptide-functionalized surfaces for pathogen detection and elimination [5,12-14]. As a potential candidate for selective targeting, AMPs are short sequences (often fewer than 30 amino acids) and easy to mass-produce, have the ability to be readily functionalized with a variety of native and non-native amino acids, and are known to selectively target bacteria, fungi, and even human malignancies [15,16]. Previous publications have shown that free AMPs in solution have many modes of action, but generally target bacteria thorough the initial electrostatic interactions between positively charged peptides and negatively charged bacterial cell membranes; the disruption of these membranes due to the amphipilicity of

the peptide [17-20]. The first and most widely studied antimicrobial peptides are peptides in the magainin family, which was first isolated from the frog *Xenopus laevis* skin [21]. Our studies focus on MSI-78, or pexiganan, an antimicrobial peptide designed by the Genaera Corporation, which is a potent synthetic analogue of magainin.

Investigations into the molecular interactions between MSI-78 and various model cell membranes have found a concentration-dependent interaction mechanism with different observed peptide orientations relative to the membrane surface [18]. Other research groups have also studied membrane disruption of MSI-78 by nuclear magnetic resonance (NMR) spectroscopy [22-27]. It has been reported that MSI-78 adopts an α–helical structure on association with a cellular membrane and a random coil in aqueous solution [28,29]. Its short sequence and α–helical structure make it a good choice for structural characterization.

Bulk and solution measurements are only the first step in understanding surface-bound behavior. A variety of surface sensitive analytical techniques and methodologies have been applied to explore conformation, ordering, and orientation behaviors of the interfacial molecules. Examples include adsorption/desorption measurements using ellipsometry and surface plasmon resonance (SPR) [30-32], elemental analysis with secondary ion mass spectrometry (SIMS) and x-ray photoelectron spectroscopy (XPS) [33-36], and surface vibrational spectroscopy using attenuated total reflectance-Fourier transform infrared (ATR-FTIR) spectroscopy [37-40] and surface-enhanced Raman spectroscopy (SERS) [41]. Although these experimental tools have the ability to acquire

a qualitative and quantitative understanding at the molecular level of interfacial proteins/peptides and their functions, it is still very difficult to probe molecular level structural information of peptides and proteins *in situ* (e.g. at the solid/liquid interface) with monolayer surface sensitivity using the techniques listed above. As a result, further investigations of these molecular interactions still require more accurate *in situ* measurements.

In this study, we immobilized MSI-78 through different peptide termini onto surfaces in order to create antimicrobial coatings. We characterized the surface-immobilized MSI-78 structure using sum frequency generation (SFG) spectroscopy, a second-order nonlinear optical spectroscopy that is intrinsically surface sensitive [42,43] and has been applied to examine the secondary structures and orientations of various peptides and proteins adsorbed on surfaces [44-47]. The experimentally deduced MSI-78 structure was further validated using circular dichroism (CD) spectroscopy and coarse-grained molecular dynamics simulations. In addition, we determined the antimicrobial activities of different peptide analogues in order to correlate the deduced structural information with the biological efficacy of the AMPs with the hope of understanding the structure/function relationship of surface immobilized AMPs.

2.2 Materials and Methods

All chemicals and solvents were purchased from Sigma Aldrich (St. Louis, MO) and used without further purification unless otherwise stated. O-(Propargyl)-N-(Triethoxysilylpropyl) Carbamate (alkyne-silane) (Gelest, Arlington, VA), azido-EG3-

Maleimide linker (Click Chemistry Tools, Scottsdale, AZ) and maleimide-EG1-NHS linker (Conju-Probe, San Diego, CA) were used as received.

2.2.1 Substrate Surface Preparation.

2.2.1.1 Right-Angle CaF_2 Prisms.

Right-angle CaF_2 prisms (Altos Photonics, Inc., Bozeman MT) were first soaked in toluene for 24 hr and then sonicated in 1% Contrex AP solution (Decon Laboratories, King of Prussia PA) for 10 min. Prisms were then thoroughly rinsed with deionized water (18.2 MΩ cm), dried under N_2 gas, and treated with O_2 plasma (Glen 1000P) for 30 s immediately before being coated with SiO_2. A layer of 100 nm of SiO_2 was deposited onto the cleaned CaF_2 prism by electron-beam deposition process using an SJ-26 evaporator system at pressure below 10^{-5} Torr with a deposition rate of 5 Å s^{-1}. After multiple uses, old SiO_2 was removed using a 5% (by volume) solution of HF.

2.2.1.2 Quartz Discs.

UV-grade quartz disks (Jasco Inc., Japan) used for circular dichroism measurements were cleaned in piranha solution, thoroughly rinsed with deionized water, dried under N_2 gas, and treated with a 3 min O_2 plasma.

2.2.2 Surface Functionalization.

2.2.2.1 Self-Assembled Monolayer (SAM).

SiO_2-coated CaF_2 prisms and quartz disks were cleaned under O_2 plasma (PE-25-JW) for 3 min, then immediately placed into a freshly prepared solution with anhydrous

toluene and 0.1 mM either octadecyltrichlorosilane (OTS, **Fig 2.1 *A***), alkyne-EG1-silane (2-step click, **Fig 2.1 *B***), or APTES (2-step APTES, **Fig 2.1 *C***) solution to prepare a self-assembled monolayer (SAM). Reaction was allowed for 24 h at room temperature to form SAM materials. The functionalized prisms were then rinsed with copious toluene and methanol and were then dried under nitrogen gas.

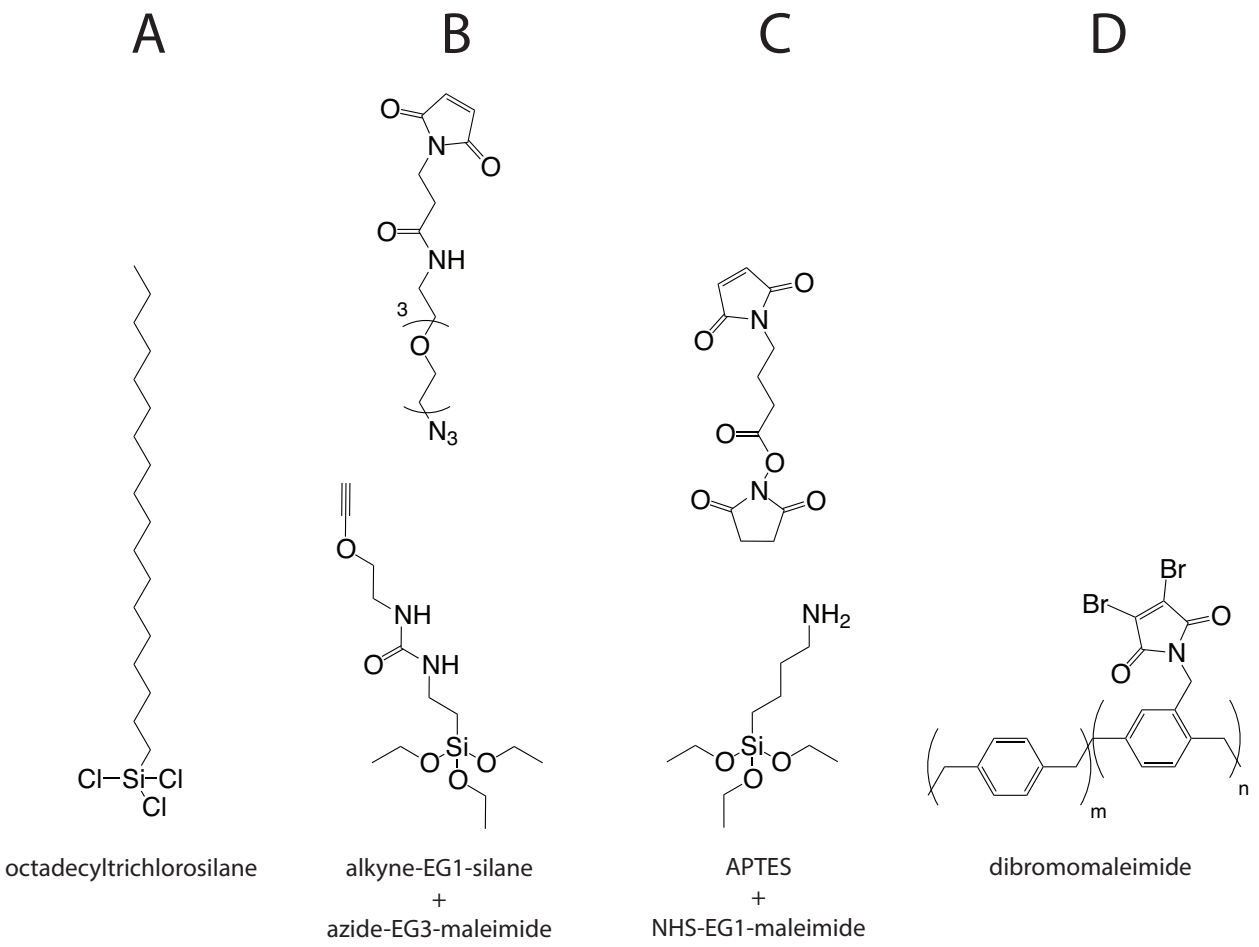

Figure 2.1: Chemical Structures of Surface Functionalization Materials. (A) Octadecyltrichlorosilane (OTS), used for non-specific binding of MSI-78. (B,C) Maleimide functionalization with two different SAMs and their corresponding linkers. (D) Dibromomaleimide (DBM) polymer.

ID	Sequence
MSI-78	GIGKFLKKAKKFGKAFVKILKK-NH_2
nMSI-78	**C**GIGKFLKKAKKFGKAFVKILKK-NH_2
cMSI-78	GIGKFLKKAKKFGKAFVKILKK**C**-NH_2

Table 2.1: Amino Acid Sequence of wild type MSI-78, nMSI-78, and cMSI-78. Mutations are highlighted in red.

2.2.2.2 2-Step Linker.

For two of the three SAMs, linkers containing maleimide functionality must be added to the existing surface for successful peptide immobilization. Azido-EG3-maleimide linker (**Fig 2.1 *B***) was prepared according to the manufacturers' instruction. The alkyne-functionalized prisms were placed into an aqueous solution containing azido-EG3-maleimide linker (1 mM), sodium ascorbate (0.2 M), and copper sulfate (0.5 mM), and reacted overnight. Prisms were then rinsed with water, EDTA, and water to remove any remaining copper ions. Amine functionalized prisms were placed into a phosphate buffer (pH 7.4, ionic strength 5 mM) solution containing maleimide-EG-NHS linker (**Fig 2.1 *C***, 1 mM) and reacted for 1 hour. Then the prisms were rinsed with copious phosphate buffer.

2.2.2.3 Dibromomaleimide (DBM) CVD Polymer.

All surface preparation using dibromomaleimide (DBM) polymer was done by collaborators in the Lahann lab at the University of Michigan. Details of their CVD equipment as well as DBM synthesis and deposition can be found in references [48,49]. Briefly, DBM precursor was deposited by CVD polymerization using a custom-built CVD

system. Precursor was first sublimed at approximately 120°C. The precursor vapor then underwent pyrolysis at 750°C, and was deposited and polymerized simultaneously onto pre-cleaned calcium fluoride (CaF_2) prisms at 15^{o}C at a pressure of 0.1 mbar.

2.2.3 Cysteine-Modified MSI-78 Surface Immobilization.

MSI-78 is a 22-residue antimicrobial peptide with the amino acid sequence: GIGKFLKKAKKFGKAFVKILKK-NH_2. C-terminal amidation of this peptide was reported to increase its activity [23]. Cysteine-mutated MSI-78 was synthesized using the solid phase Fmoc method with a single cysteine added to the n-terminus (nMSI-78) or c-terminus (cMSI-78) of MSI-78. The nMSI78 and cMSI78 sequences are shown in **Table 2.1**. Peptide stock solutions were prepared by dissolving 2.0 mg of peptide powder into 8.0 mL of Millipore deionized water (18.2 MΩ cm) and stored in a -30 °C freezer.

Surface-functionalized prisms or disks were placed into a phosphate buffer solution (pH 7.2, ionic strength 5.0 mM) containing nMSI-78 or cMSI-78 (5.0 μM), tris(2-carboxyethyl)phosphine (TCEP) (5.0 μM, used as a reductant to minimize disulfide bonds between cysteines of different peptides) and left to react for 2 h. After peptide immobilization, prisms were rinsed with both phosphate buffer and 1.0 mM sodium dodecyl sulfate (SDS) to wash away physically adsorbed peptides, followed by several additional phosphate buffer washes.

2.2.4 Circular Dichroism (CD) Spectroscopy.

The CD spectra of free MSI-78 in solution and immobilized MSI-78 on surfaces were collected with a J-815 CD spectrometer (Jasco Inc., Japan) using continuous scanning

mode at room temperature. All spectra were scanned between 195 and 240 nm at 1 nm resolution, 20 nm min^{-1} scan rate, and averaged by five successive scans for each sample.

2.2.5 Sum Frequency Generation (SFG) Vibrational spectroscopy.

The SFG setup used in this study was purchased from EKSPLA. The details regarding SFG theories and measurements have been described both in **Chapter 1** and in previous publications [50-66]. Briefly, SFG is a second-order nonlinear optical technique and is intrinsically sensitive to surfaces and interfaces. In our experimental setup, two laser beams (one 532 nm visible laser beam and one frequency-tunable IR beam) pass through one surface of a right angle CaF_2 prism and then overlap spatially and temporally at the other surface (shown in **Fig 2.2**). The incident angles of the 532 nm and IR beams in the SFG setup are 58° and 55°, respectively, relative to the surface normal of the incident prism surface. SFG spectra with different polarization

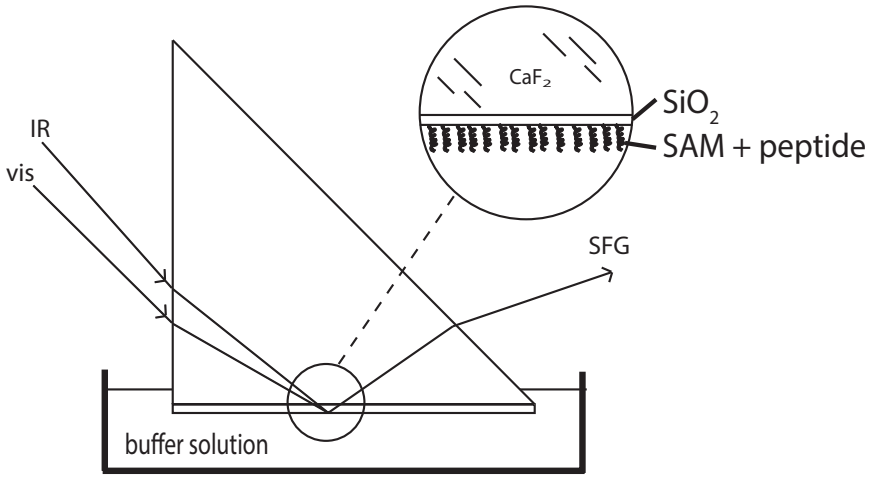

Figure 2.2: SFG Experimental Design. The use of near-total-internal-reflection of both visible and IR light enhances peptide signal. This geometry is used with immobilized nMSI-78 or cMSI-78 on right angle prisms in phosphate buffer.

combinations of the input and generated signal beams including ssp (s-polarized output SFG signal, s-polarized input visible beam, and p-polarized input IR beam) and ppp were collected using near total internal reflection geometry [67].

For an α–helical structure, the Amide I signal is centered at about 1650 cm^{-1} [68]. The orientation of an α–helix can be deduced from the measured ratio of the effective second-order nonlinear optical susceptibility tensor components detected in ssp and ppp polarizations [44,47]. This method has been applied to deduce orientation of peptides associated with lipid bilayers [18,69].

SFG spectra are fitted using the following equation as previously reported [44]:

$$\chi_{eff}^{(2)}(\omega) = \chi_{\mathrm{NR}}^{(2)} + \sum_{q} \frac{A_q}{\omega - \omega_q + i\Gamma_q} \tag{2.1}$$

Where ω is the frequency of the IR beam, A_q is the amplitude of the *q*th vibrational mode, and Γ_q is the damping coefficient of the *q*th vibrational mode.

2.2.6 Coarse-Grained Molecular Dynamics Simulations on Immobilized MSI-78.

All implementations of molecular dynamics simulations and results therein were developed and performed in the Brooks lab at the University of Michigan. A previously developed coarse-grained surface force field is used in this work to study peptide-surface interactions [70]. This model was developed based on the Karanicolas and Brooks' (KB) Go-like protein model [71,72] and was well parameterized based on a set

of benchmark experimental data for protein adsorption free energies onto SAM surfaces [73]. The KB protein model is used because it has been shown to be able to consistently reproduce protein folding free energy surfaces and folding mechanisms. Using the formation of native contacts defined in the KB protein model, a five-term potential was used to describe the interaction between each residue and a SAM surface (as shown below in eq. 2). The first three terms describe the adsorption well and the energy barrier, which are general for any residue and surface type. The last two terms are used to delineate the hydrophobicity of each residue and surface.

$$V_{\text{surface}} = \sum_{i}^{\text{N}} \left\{ \pi\rho\sigma_i^3\varepsilon_i \left[\theta_1 \left(\frac{\sigma_i}{z_{is}} \right)^9 - \theta_2 \left(\frac{\sigma_i}{z_{is}} \right)^7 + \theta_3 \left(\frac{\sigma_i}{z_{is}} \right)^3 - \left(\theta_s \left(\chi_s - 4.5 \right) + \theta_p \chi_p \right) \left(\frac{\sigma_i}{z_{is}} \right)^3 \right] \right\} \tag{2.2}$$

All θ's are parameters that were optimized for this surface. A maleimide surface is slightly hydrophilic with χ_s set to be 1.5 [70]. The values of χ_p are hydropathy indices of residues that can be found in many biochemistry textbooks. The bond between the maleimide surface and the cysteine side chain was simulated through the addition of a harmonic restraint tethering the terminal residue of the peptide to the surface and represented by the interaction potential of the following form:

$$U_{\text{restraint}} = \frac{1}{2} k_r \left(r - r_{\text{eq}} \right)^2 \tag{2.3}$$

Where k_r = 10 kcal/mol is the parameter describing the strength of the restraint and r is the distance of the tethering site from the origin of the surface (0, 0, 0), and r_{eq} = 5.8

Å is the equilibrium distance from the tethering site to the surface origin. The tethering length was used to approximate the distance between the maleimide surface and the C_α of the cysteine residue at the tethering site.

2.2.7 Antimicrobial Activity Test of Immobilized Peptide.

Quartz disks were used to grow SAMs and immobilize peptide in the antimicrobial test (instead of prisms used in SFG). They were cleaned using the same method presented in **Section 2.2.1.2**.

A LIVE/DEAD BacLight Bacterial Viability kit (L-7007, Invitrogen, Carlsbad, CA) was used to determine bacterial cell viability. A solution of the mixed SYTO 9 and propidium iodide (PI) dyes was prepared according to the manufacture's instructions. *Escherichia coli* ATCC 25922 was grown in Luria-Bertani (LB) broth (3 mL, pH 7.2) at 37 °C overnight. The overnight grown bacterial culture was diluted with fresh LB medium to a concentration around 10^8 CFU/mL. A 5.0 µL sample of diluted bacterial culture was mixed with the fluorescent dyes (5.0 µL); the mixture was dropped onto a peptide-coated quartz disk or an untreated quartz slide (control), and a glass coverslip (2.5 cm x 2.5 cm) was placed on the droplet. This slide sample was incubated at room temperature in a dark environment for 15 min before being examined using a fluorescence microscope (Olympus IX71, Center Valley, PA) equipped with a fluorescence illumination system (X-Cite 120, EXFO) and appropriate filter sets. Images were randomly acquired on different spots by using an oil immersion 60X objective lens.

2.3 Results

2.3.1 Surface Behavior of MSI-78 on Octadecyltrichlorosilane (OTS) SAMs.

In order to understand surface properties of chemically immobilized MSI-78, we first looked at its adsorption behavior at surfaces with no functionality for chemical immobilization. Octadecyltrichlorosilane (OTS), a hydrophobic long chain SAM, was used as a model for non-specific binding. Results in **Fig 2.3** show that in the presence of an amphipathic environment (hydrophilic water and hydrophobic SAM), cysteine-modified MSI-78 not only is present at the surface, but forms α-helical structure as seen in the peak located at 1650 cm^{-1} (**Fig 2.3 *A***). All forms of MSI-78, nMSI-78 (not shown) and cMSI-78 (not shown), exhibit a propensity to interact with the surface and form α-helical structures at this aqueous SAM interface.

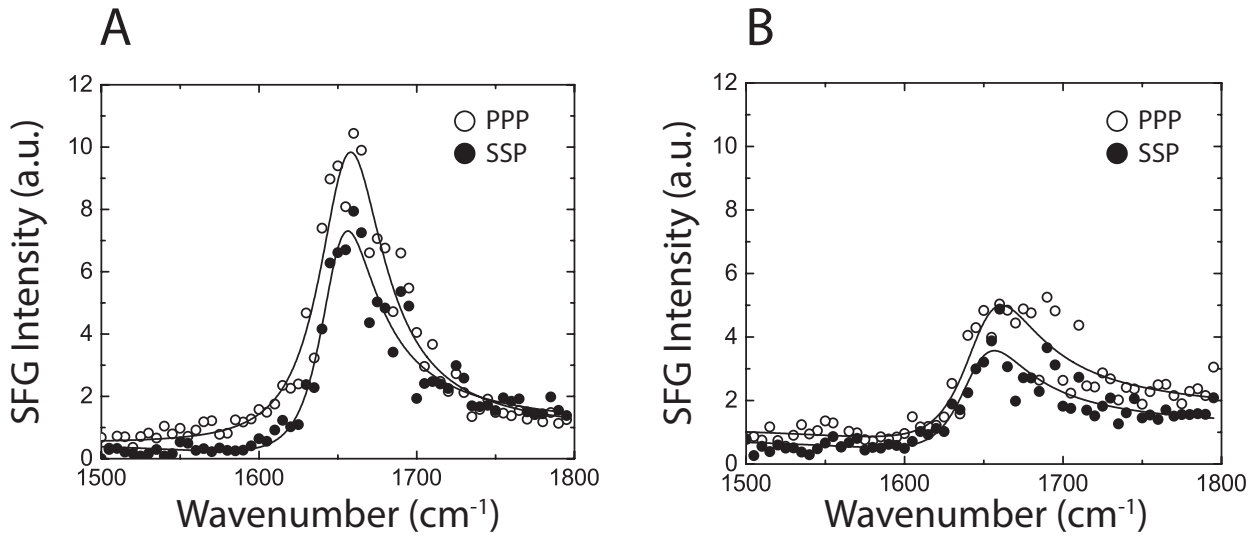

Figure 2.3: Nonspecific Adsorption of MSI-78. (A) By physical adsorption alone, both MSI-78s forms α-helical structure at the hydrophobic OTS/water interface (as seen by the presence of SFG signal at 1650 cm^{-1}). (B) Peptide is weakly bounded, and signal decreases when surface is washed using phosphate buffer.

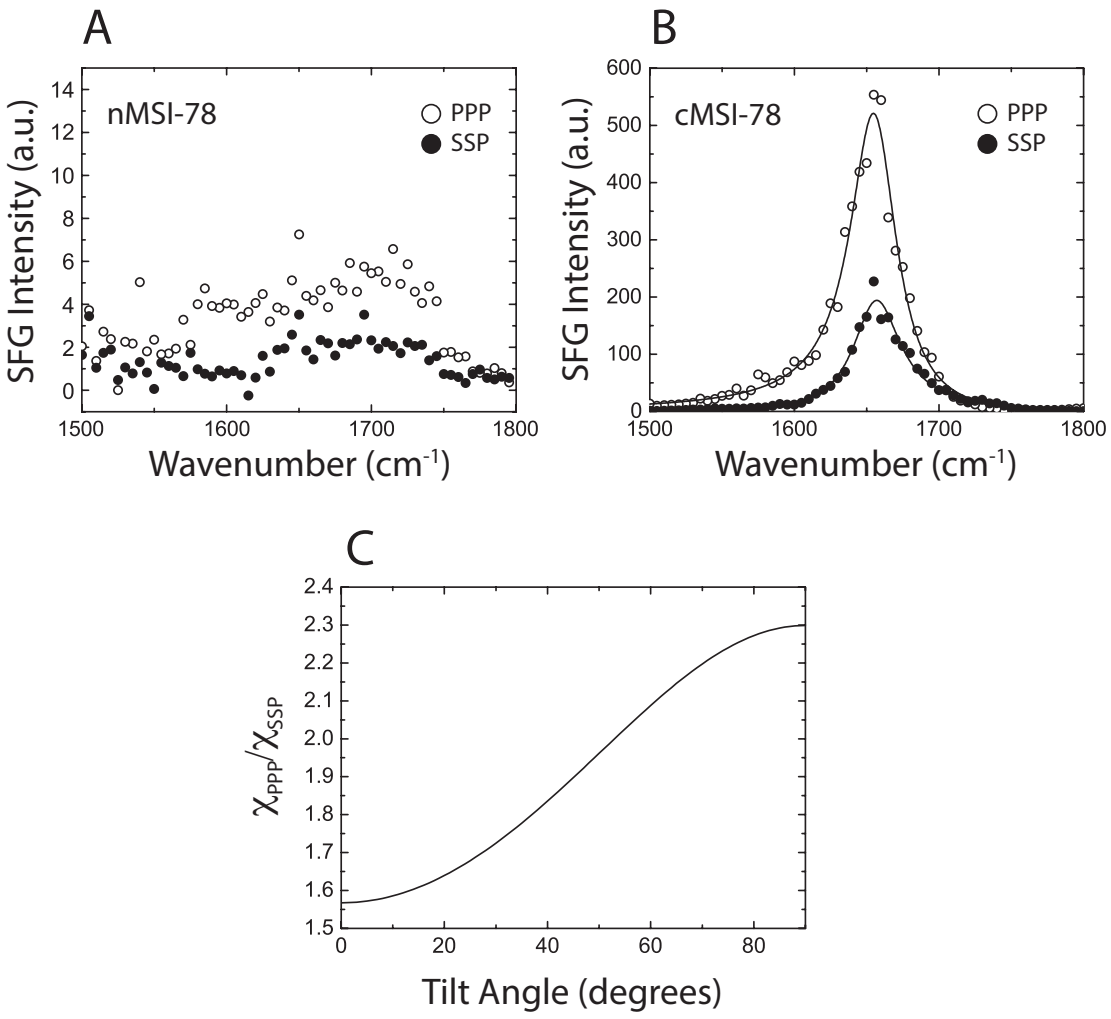

Figure 2.4: Orientation of Chemically Immobilized MSI-78. (A) No signal is measured for n-terminus attachment of MSI-78. (B) A clearly resolved peak at 1650 cm^{-1} is seen for c-terminus attachment. (C) Signal strength ratio as a function of tilt angle. A calculated ratio for cMSI-78 of 1.66 results in a tilt angle of ~29 degrees relative to the surface normal.

The SFG ppp and ssp spectra detected from cysteine modified cMSI-78 was fitted using a standard SFG spectra fitting method [44] as shown in **Fig 2.3** ***A*** and **Equation 1**. The measured χ_{ppp}/χ_{ssp} ratio of the Amide I peak at 1650 cm^{-1} is 1.23, which can be used to deduce the orientation of immobilized nMSI-78 and will be discussed further below.

Due to the nature of non-specific binding, peptide is easily washed away with excess phosphate buffer (**Fig 2.3 *B***). The measured χ_{ppp}/χ_{ssp} ratio from the washed OTS surface does not change significantly; its value is approximately 1.20.

2.3.2 Orientations of Surface-Immobilized MSI-78

Once a surface helical structure was established for non-specific binding of a hydrophobic SAM, SFG spectra were collected from chemically immobilized nMSI-78 and cMSI-78 on alkyne-silane + azide-EG3-maleimide SAMs. This combination of SAM+linker allowed for a stable chemical surface, easy maleimide attachment via well-defined click chemistry, and a triethylene glycol (EG3) unit to minimize physical adsorption.

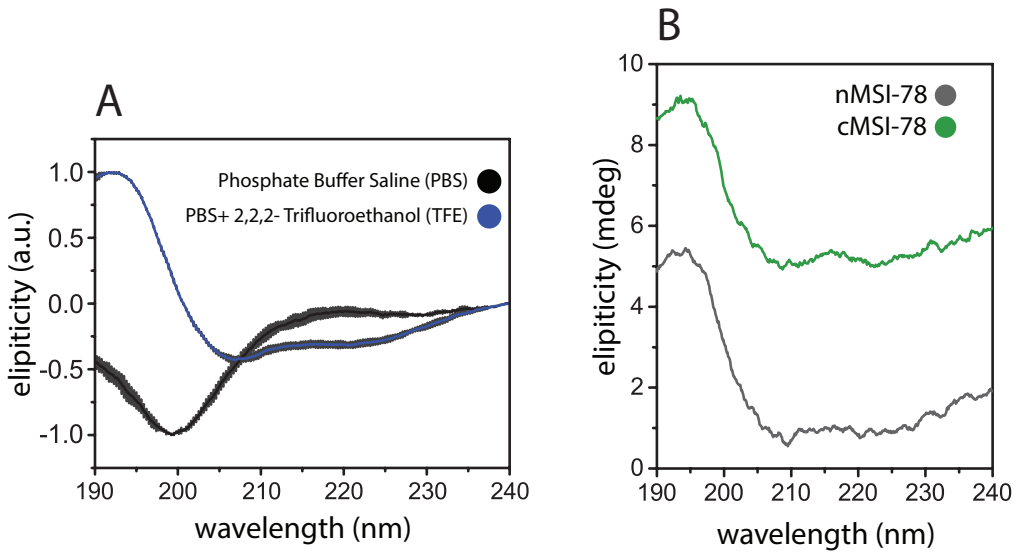

Figure 2.5: Secondary Structure of MSI-78 Measured by Circular Dichroism. (A) Solution CD spectra indicate characteristic lineshapes for random coil (MSI-78 measured in PBS) and α-helix (with the addition of TFE). (B) Surface immobilization of MSI-78 by either termini show peptide adopts α-helical structure at the SAM surface.

After a 2 h reaction of the maleimide SAM with either cysteine-modified nMSI-78 or cMSI-78, the SAM surface was rinsed using phosphate buffer, followed by a rinse using SDS to remove physically adsorbed peptides and phosphate buffer for a final cleaning of the surface. SFG spectra were then collected from both immobilized peptides on SAM in contact with a phosphate buffer solution. An SFG Amide I peak centered at ~1650 cm^{-1} was detected (**Fig 2.4 *B***) originating from the α–helical conformation of immobilized cMSI-78.

As shown in **Fig 2.4 *A***, no discernible SFG signal can be detected under either ppp or ssp polarization combinations from nMSI-78 after surface immobilization. From the parameters that define the origin of SFG signal, the lack of signal seen in nMSI-78 indicates that either the immobilized peptide molecules (1) have a random coil conformation or (2) they adopt an α–helical structure but with the helix axis running parallel to the surface. This will be further studied below using CD spectroscopy.

For c-terminally immobilized MSI-78 (**Fig 2.4 *B***), SFG results show a well-defined signal with peak center at 1650 cm^{-1} indicating α–helical structure at the interface. Calculating the SFG signal strength ratio between the ssp and ppp polarization combinations results in a ratio of 1.66. Under the assumption of a delta-distribution of orientations (all measured peptides adopt an identical tilt angle to the surface normal), we see that cMSI-78 tilts 23° with respect to the surface normal (**Fig 2.4 *C***).

2.3.3 Secondary Structure of and Surface nMSI-78 and cMSI-78.

To further conclude the origins of SFG signal from chemically immobilized nMSI-78, circular dichroism (CD) spectra of surface-immobilized nMSI-78 and cMSI-78 were taken. Bulk and surface CD spectra of cysteine-modified MSI-78 (nMSI-78 and cMSI-78) at room temperature are shown in **Fig 2.5 *A***. Both cysteine-derivatives of MSI-78 adopt a random coil conformation in aqueous buffer solution (their spectra are averaged into the plot shown in panel A). In the presence of a helix promoter such as 2,2,2-trifluoroethanol (TFE), MSI-78 in solution adopts an α–helical conformation. After surface coupling through the reaction of the terminal cysteine group with surface maleimide group, the immobilized cysteine derivatives of MSI-78 exhibited an α–helical conformation, as characterized by the double minima at 207 and 222 nm in the CD spectra (**Fig. 2B**).

It is concluded that nMSI-78 through CD spectroscopy, readily adopts an α–helical conformation at abiotic SAM surfaces. From this, SFG results of nMSI-78 point to this peptide having helical structure but with the helix backbone running parallel to the surface.

2.3.4 Coarse-Grained Molecular Dynamics Simulation of Immobilized MSI-78.

In order to provide a more detailed understanding of physical origins of different orientations of immobilized nMSI-78 and cMSI-78 observed in this research, The Brooks Lab at the University of Michigan performed coarse-grained molecular dynamics simulations. As stated in **Section 2.2.6**, we use χ_s of 1.5 for the slightly hydrophilic maleimide SAM surface and the tethering length was approximated to be 5.8 Å based on the length of the amino acid cysteine. In the simulation, no external force to constrain the helical structure was used other than the native contacts of the initial helical structure which are defined by the Go-like protein model.

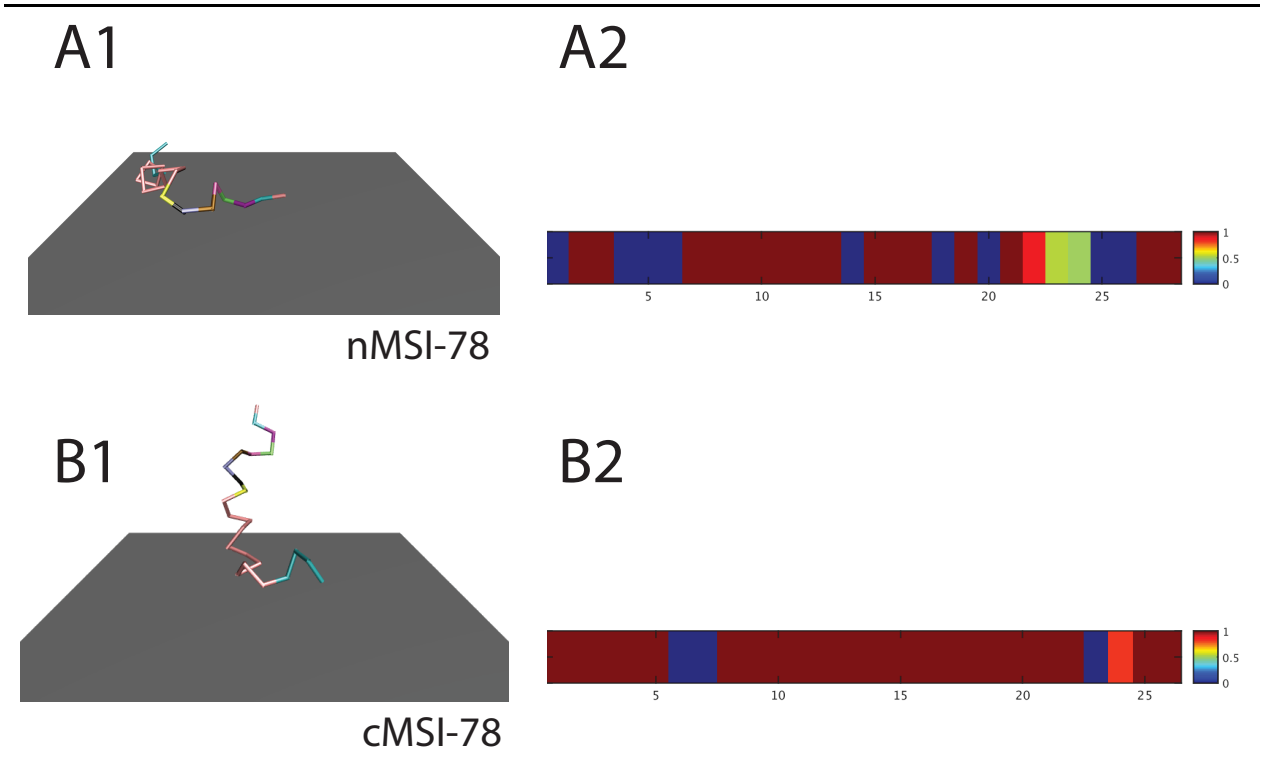

Figure 2.6: Coarse-Grained Simulation Results of Tethered MSI-78. (A1) nMSI-78 and (B1) cMSI-78 immobilized on a maleimide-terminated SAM exposed to phosphate buffer solution. (A2,B2) Assessment of native contacts shows peptides maintain helical form independent of orientation. Simulated results well recapitulate the experimentally deduced peptide orientations.

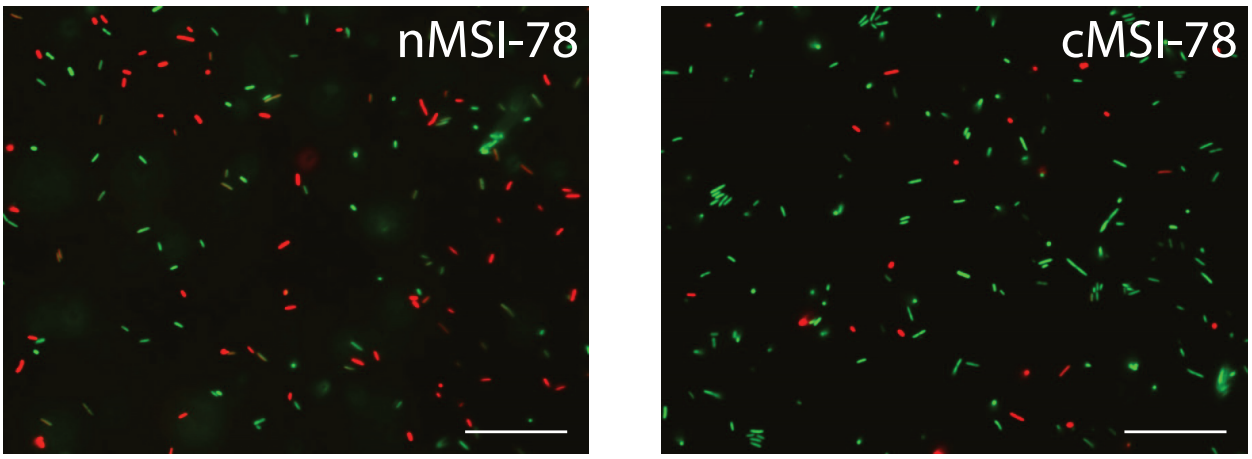

Figure 2.7: Antibacterial Tests of Surface Immobilized MSI-78. Representative micrographs of MSI-78 antibacterial tests against *E. coli*.

Simulation results of both nMSI-78 and cMSI-78 are shown in **Fig 2.6**. Generally, the maleimide surface is only slightly hydrophobic which has a favorable interaction with the hydrophobic c-terminal end of MSI-78. Therefore, as seen in **Fig 2.6** ***A1*** and ***B1***, the hydrophobic c-terminal end readily interacts with the maleimide surface, however the amphipathic nature of the rest of the peptide (in the case of cMSI-78) is well accommodated in the surrounding solution. This results in a peptide that stands up relative to the surface and agrees with SFG results. Likewise, the n-terminus MSI-78 has strong affinity with the maleimide surface due to its hydrophobic c-terminus serving as an anchor for the untethered side of nMSI-78. This results in a peptide that lies down on the surface which agrees with SFG results of nMSI-78.

To confirm helicity for both peptides, the native contacts were monitored for both simulations and can be seen in **Fig 2.6** ***A2*** and ***B2***. The presence of most native

contacts in the peptide indicate that structure is conserved independent of peptide orientation further confirming both SFG and CD results.

2.3.5 Antibacterial Activity of Immobilized MSI-78.

To summarize our understanding of surface behaviors of chemically immobilized MSI-78, antimicrobial activity tests were performed against *Escherichia coli* (*E. coli*) for both analogues of surface-bound MSI-78. The LIVE/DEAD bacteria assay uses two separate fluorescence dyes, SYTO 9 and propidium iodide (PI), both of which are nucleic acid staining dyes. SYTO 9, having a green fluorescence emission wavelength, is a small dye molecule that can pass through live cell bacterial membranes. This color indicates cells that are alive. PI is a dye that must transport through large pores induced by AMPs such as MSI-78. Presence of this dye indicates cells which have compromised cell membranes and are presumed “dead”.

Antibacterial properties of chemically immobilized nMSI-78 and cMSI-78 were found to be quite different (**Fig 2.7**) and counterintuitive to previous SFG, CD, and coarse-grained simulation results. After a 60 minute exposure, both AMP surface captured similar amounts of bacteria, however nMSI-78 was able to kill more adsorbed bacteria than cMSI-78. Initial evidence points to an environmental role of AMP activity, but more will be discussed in the text below.

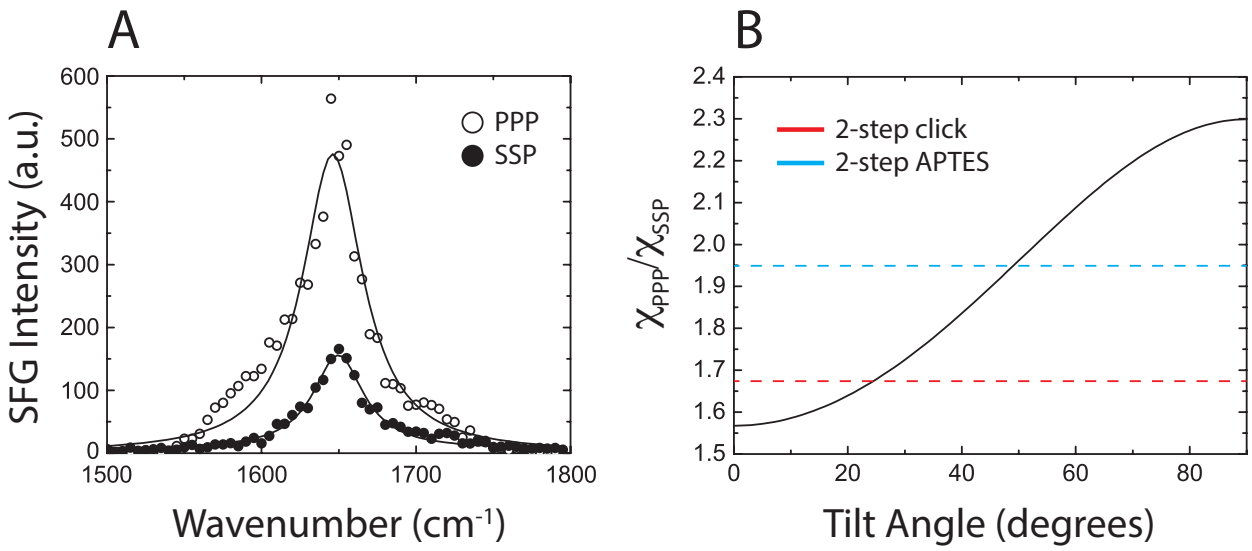

Figure 2.8: MSI-78 Immobilized to 2-Step APTES SAM. (A) Cysteine-modified cMSI-78 shows good chemical attachment with this SAM. (B) Comparison of peptide orientation between each 2-step SAM.

2.3.6 Other Unique Abiotic Surfaces

Among other potential surfaces used in peptide attachment, investigating cost-effective, easy to manufacture functionality is important for maximizing the ubiquity of these biomaterials. Among those are a compliment to the already discussed 2-step click SAM; a 2-step SAM using an APTES-NHS reaction, as well as a maleimide-functionalized polymer which can be easily deposited using chemical vapor deposition (CVD).

Fig 2.8 shows the results of cMSI-78 attached to a maleimide surface prepared by a 2-step SAM via an APTES-NHS reaction. This SAM, in contrast to the 2-step click SAM, is a low-cost alternative, which may provide a solution to functional surfaces that cost significantly less than some other alternatives. SFG results show not only a peak centered at 1650 cm^{-1}, indicative of alpha-helix, but also a shoulder at 1630 cm^{-1},

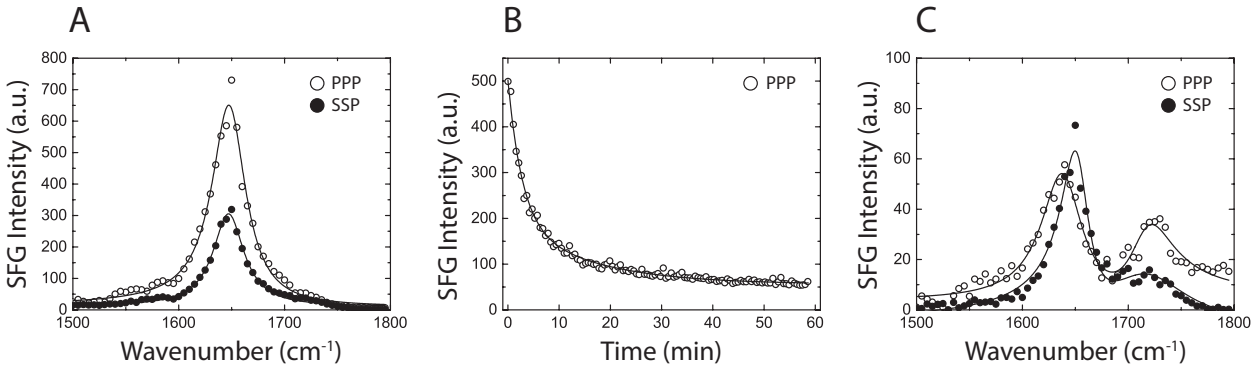

Figure 2.9: Reversible Thiol Reaction on Dibromomaleimide CVD Polymer. (A) Peptide attachment on DBM polymer. (B) With excess TCEP, SFG signal decreases (C) Resulting signal after peptide is removed.

originating from the free maleimide on the surface. This shoulder is clearly resolved and does not interfere with orientation calculations. In comparison to 2-step click SAMs, cMSI-78 tilts more towards the surface (**Fig 2.8 *B***) on 2-step APTES SAM.

A dibromomaleimide-functionalized polymer prepared with CVD also shows good peptide attachment (**Fig 2.9 *A***). Dibromomaleimide (DBM) participates in a reversible thiol reaction with cysteine. In excess TCEP (5 mM; 1000x greater than peptide concentration), a reducing agent used to minimize disulfide bonds between free MSI-78 in solution, cMSI-78 is removed from the surface as TCEP breaks the thiol/maleimide bond and releases MSI-78 from the surface (**Fig 2.9 *B***). SFG spectra decrease significantly after the addition of excess TCEP (**Fig 2.9 *C*)**.

2.4 Discussion

With the use of surface-sensitive spectroscopies, the knowledge about the structures of peptides immobilized on surfaces was gained. MSI-78, with its native mutations,

allowed for a unique platform to a variety of surfaces including those of self-assembled monolayers and polymers.

Much of what we understand about antimicrobial peptides (AMPs) has been based on solution studies [13,15,17,21]. Previous studies indicated that wild-type MSI-78 adopts a random coil conformation in aqueous buffer solution but forms an α–helical conformation in the presence of lipid vesicles [28]. Recent studies have investigated tethered peptides, but with a limited number of surfaces [14,74], or with a number of other techniques [12,75].

Our first experiments focused on physical adsorption using octadecyltrichlorosilaine (OTS) SAMs. Similar to environments seen in the lipid bilayers of target cellular/bacterial membranes, MSI-78 freely adopted an α-helical conformation on OTS. The orientation of a surface-immobilized α–helical peptide can be defined by a tilt angle θ, which represents the angle between the principal axis of the helical peptide and the surface normal. This tilt angle θ can be determined by measuring the χ_{ppp}/χ_{ssp} ratio of SFG Amide I signal of the helix, the details of which have been reported previously [44-47]. The dependence of the χ_{ppp}/χ_{ssp} ratio on the helix orientation angle for MSI-78 is plotted in **Fig 2.8 *B***. SFG ppp and ssp spectra detected from MSI-78 were fitted using a standard SFG spectra fitting method [44] as shown in **Fig 2.3** and **Equation 2.1**. The measured χ_{ppp}/χ_{ssp} ratio of the Amide I peak at 1650 cm^{-1} is 1.23, which is

below the measured χ_{ppp}/χ_{ssp} values for a single distribution in orientation (δ-distribution, **Fig 2.4 *C***). This is to be expected, since there likely is no preferred orientation for MSI-78 in OTS and peptides can freely adopt any orientation adsorbed on the SAM. As was expected, signal decreased when the surface was washed with excess phosphate buffer.

Unlike OTS, all chemically functionalized surfaces used in this study were predominately either hydrophilic, or marginally hydrophobic. Yet, both nMSI-78 and cMSI-78 adopted α-helical conformations as seen from both SFG (**Fig 2.4 *B*)** and CD (**Fig 2.5 *B***). Upon chemical attachment to the maleimide-functionalized surface, MSI-78 looses significant entropy and free energy favored the enthalpy of folding. As a result, even in phosphate buffer (where MSI-78 should assume a random coil structure), this peptide is predominately helical at the surface.

Although MSI-78 has helix structure after surface immobilization via either attachment position (n- or c-terminus), the measured orientations are quite different. While c-terminally tethered MSI-78 shows clear resolvable signal with a measured orientation value of ~20°, no discernable SFG signal is measured for nMSI-78 chemically immobilized to 2-step click SAM surfaces (**Fig 2.4 *A***). Because of the limitations of SFG (discussed in **Section 1.2.5**), this result has three possibilities: (1) there is no peptide on the surface, (2) this peptide adopts a random coil structure (since only preferentially ordered Amide I can generate SFG signal), or (3) MSI-78 lies down on the surface. Two other supplementary techniques, circular dichroism spectroscopy, and coarse-grained

molecular dynamics simulations were used.

Results of circular dichroism (CD) measurements on surface bound MSI-78 indicate that both peptide analogues immobilized via different termini exhibit α-helical structure (**Fig 2.5 *B***), by comparing the CD structures of free peptide in buffer solution and in 2,2,2-trifluoroethanol (TFE) (**Fig 2.5 *A***). Performing molecular dynamics simulations on chemically immobilized MSI-78 also supports results from SFG.

Surface chemistry may have an important role in peptide orientation, but not necessarily secondary structure. In the case of all three functionalized surfaces; 2-step click SAM, 2-step APTES SAM, and dibromomaleimide polymer, each calculated orientation was different. The calculated χ_{ppp}/χ_{ssp} ratio of the Amide I peak at 1650 cm^{-1} for each surface is 1.79, 1.95, and 1.21 respectively. These ratios (using **Fig 2.8 *B***) correspond to angles (relative to the surface normal) of 36°, 49°, and out of range, respectively. Again, because dibromomaleimide (DBM) is less ordered, this could potentially lead to MSI-78 having multiple orientations.

In searching for a more applicable surface, our focus shifted to other potential chemical attachment schemes. The use of a different 2-step SAM, even though ultimately led to a different peptide orientation, is a cost-effective alternative to 2-step SAMs using click chemistry. Likewise, polymer coatings via CVD are ideal for practical applications because such polymers can be deposit on any substrates. More importantly, the use of DBM as a reversible surface (**Fig 2.9**) has great potential in biomolecule delivery, or

situations where you need peptide both attached and removed from the same surface.

Antibacterial testing provides a direct measure of how attachment ultimately decides biomolecule activity. Initially, it was our hypothesis that nMSI-78, a peptide which lies down on maleimide surfaces, would have less activity than cMSI-78, a peptide that stands up on maleimide. Due to the orientation of the peptide, the number of available cysteines for chemical attachment would be lower for nMSI-78 since lying down would block or prevent peptide from accessing those cysteines that nMSI-78 was covering. Likewise, a peptide lying down would also have less access to a pathogen such as *E. coli*, since its flat conformation (depending on the attractive forces of the maleimide surface itself) would have a more difficult time interacting with bacteria. Results of the bacteria test however were opposite our original hypothesis. Although counterintuitive to our initial hypothesis, an ability for a peptide to interact and kill a pathogen (such as *E. coli*) may be dependent on factors such as local environment and attachment point rather than peptide orientation ultimately determining activity. A peptide in aqueous media, the experimental conditions in SFG and CD, may only have solvent or surface interactions, which would affect peptide orientation. On the other hand, the amphipathic environment of an *E. coli* bacterial cell membrane is much different than aqueous environment. As a result, peptides may easily interact with the surface, and peptide attachment point may be the only factor governing activity. It will take activity testing with other surfaces and conditions to ultimately answer this question.

2.5 Conclusion

Anti-microbial peptides (AMPs) have enormous potential in areas of antibiotics, pathogen identification, and cancer therapy. When these unique molecules are intelligently tethered to solid supports, these functionalized materials become even more important for next generation biosensors or bioactive textiles, just to name a few. Understanding the surface conformation and orientation of these biomolecules is critical, and the use of sum frequency generation (SFG) spectroscopy in combination with circular dichroism (CD) spectroscopy, molecular dynamics simulations, and antibacterial testing, has helped understand interaction behaviors at a molecular level.

In this study, an antimicrobial peptide, MSI-78, was tethered to an abiotic solid support via different termini using cysteine maleimide coupling. Using an *in situ* surface sensitive technique such as SFG, we observed that although both peptides form α–helix secondary structures on the surface when tethered, they have very different orientations. N-terminally labeled MSI-78 (nMSI-78) lies down on maleimide-terminated surfaces whereas c-terminally labeled MSI-78 (cMSI-78) stands up. Secondary structure on abiotic surfaces was confirmed by the use of circular dicroism (CD) spectroscopy and peptide orientation was supported by molecular dynamics simulations.

Activity testing was performed on both peptides in order to see how tethering site and orientation determine antibiotic activity against *E. coli* bacteria. Results support the idea that tethering site impacts activity and may not depend on orientation in aqueous environment. In an investigation into more cost-effective or easily processable surfaces

for peptide attachment, we looked at a 2-step SAM via APTES/NHS reaction as well as a dibromomaleimide polymer. We see different and unique behavior for each, and further testing (including antibacterial testing) are important to better understand their surface-tethering behavior.

This *in situ* information helps rationalize how we may design better and more active surfaces. In short, the use of noninvasive spectroscopies was necessary, due to the limited sizes of the sample itself, to accurately describe its behavior.

2.6 References

[1] Magin, C.M.; Cooper, S.P.; Brennan, A.B. Non-Toxic Antifouling Strategies. *Materials Today*, **2010**, *13*, 36–44.

[2] Robert Pelton. Bioactive Paper Provides a Low-Cost Platform for Diagnostics. *Trends Anal Chem*, **2009**, *28*, 925–942.

[3] Gill, I. Bio-Doped Nanocomposite Polymers: Sol−Gel Bioencapsulates. *Chem Mater*, **2001**, *13*, 3404–3421.

[4] Wilson, C.J.; Clegg, R.E.; Leavesley, D.I.; Pearcy, M.J. Mediation of Biomaterial–Cell Interactions by Adsorbed Proteins: a Review. *Tissue Eng*, **2005**, *11*, 1–18.

[5] Cui, H.; Webber, M.J.; Stupp, S.I. Self-Assembly of Peptide Amphiphiles: From Molecules to Nanostructures to Biomaterials. *Biopolymers*, **2010**, *94*, 1–18.

[6] Jung, J.P.; Gasiorowski, J.Z.; Collier, J.H. Fibrillar Peptide Gels in Biotechnology and Biomedicine. *Biopolymers*, **2010**, *94*, 49–59.

[7] Ansari, S.A.; Husain, Q. Potential Applications of Enzymes Immobilized on/in Nano Materials: a Review. *Biotechnol Adv*, **2012**, *30*, 512–523.

[8] Tan, I.S.; Lee, K.T. Immobilization of Beta-Glucosidase From Aspergillus Niger on Kappa-Carrageenan Hybrid Matrix and Its Application on the Production of Reducing Sugar From Macroalgae Cellulosic Residue. *Bioresource Technology*, **2015**, *184*, 386–394.

[9] Sheldon, R.A.; van Pelt, S. Enzyme Immobilisation in Biocatalysis: Why, What, and How. *Chem Soc Rev*, **2013**, *42*, 6223–6235.

[10] Glinel, K.; Jonas, A.M.; Jouenne, T.; Leprince, J.; Galas, L.; Huck, W.T.S. Antibacterial and Antifouling Polymer Brushes Incorporating Antimicrobial Peptide. *Bioconjugate Chem*, **2009**, *20*, 71–77.

[11] Wark, A.W.; Lee, J.; Kim, S.; Faisal, S.N.; Lee, H.J. Bioaffinity Detection of Pathogens on Surfaces. *J Ind Eng Chem*, **2010**, *16*, 169–177.

[12] Bagheri, M.; Beyermann, M.; Dathe, M. Immobilization Reduces the Activity of Surface-Bound Cationic Antimicrobial Peptides with No Influence Upon the Activity Spectrum. *Antimicrob Agents Ch*, **2009**, *53*, 1132–1141.

[13] Hancock, R.E.W.; Sahl, H.-G. Antimicrobial and Host-Defense Peptides as New Anti-Infective Therapeutic Strategies. *Nat Biotechnol*, **2006**, *24*, 1551–1557.

[14] North, S.H.; So, C.; Fears, K.; Taitt, C.R. Chemoselective Surface Attachment of Antimicrobial Peptides and Its Effects on Interfacial Behavior. In; SPIE, **2014**; Vol. 9112, pp. 911213–1–911213–8.

[15] Giangaspero, A.; Sandri, L.; Tossi, A. Amphipathic Alpha Helical Antimicrobial Peptides. *Eur J Biochem*, **2001**, *268*, 5589–5600.

[16] Yeaman, M.R.; Yount, N.Y. Mechanisms of Antimicrobial Peptide Action and Resistance. *Pharmacol Rev*, **2003**, *55*, 27–55.

[17] Brogden, K.A. Antimicrobial Peptides: Pore Formers or Metabolic Inhibitors in Bacteria? *Nat Rev Micro*, **2005**, *3*, 238–250.

[18] Yang, P.; Ramamoorthy, A.; Chen, Z. Membrane Orientation of MSI-78 Measured by Sum Frequency Generation Vibrational Spectroscopy. *Langmuir*, **2011**, *27*, 7760–7767.

[19] Sato, H.; Feix, J.B. Peptide–Membrane Interactions and Mechanisms of Membrane Destruction by Amphipathic A-Helical Antimicrobial Peptides. *Biochim Biophys Acta*, **2006**, *1758*, 1245–1256.

[20] Nguyen, L.T.; Haney, E.F.; Vogel, H.J. The Expanding Scope of Antimicrobial Peptide Structures and Their Modes of Action. *Trends in Biotechnology*, **2011**, *29*, 464–472.

[21] Zasloff, M. Magainins, a Class of Antimicrobial Peptides From *Xenopus* Skin: Isolation, Characterization of Two Active Forms, and Partial cDNA Sequence of a Precursor. *P Natl Acad Sci*, **1987**, *84*, 5449–5453.

[22] Lee, D.-K.; Brender, J.R.; Sciacca, M.F.M.; Krishnamoorthy, J.; Yu, C.; Ramamoorthy, A. Lipid Composition-Dependent Membrane Fragmentation and Pore-Forming Mechanisms of Membrane Disruption by Pexiganan (MSI-78). *Biochemistry*, **2013**, *52*, 3254–3263.

[23] Gottler, L.M.; Ramamoorthy, A. Strucutre, Membrane Orientation, Mechanism, and Function of Pexiganan - a Highly Potent Antimicrobial Peptide Designed From Maganin. *Biochim Biophys Acta*, **2009**, *1788*, 1680–1686.

[24] Hallock, K.J.; Lee, D.-K.; Ramamoorthy, A. MSI-78, an Analogue of the Magainin Antimicrobial Peptides, Disrupts Lipid Bilayer Structure via Positive Curvature Strain. *Biophys J*, **2003**, *84*, 3052–3060.

[25] Suzuki, Y.; Buer, B.C.; Al-Hashimi, H.M.; Marsh, E.N.G. Using Fluorine Nuclear Magnetic Resonance to Probe Changes in the Structure and Dynamics of Membrane-Active Peptides Interacting with Lipid Bilayers. *Biochemistry*, **2011**, *50*, 5979–5987.

[26] Marsh, E.N.G.; Buer, B.C.; Ramamoorthy, A. Fluorine—a New Element in the Design of Membrane-Active Peptides. *Mol Biosyst*, **2009**, *5*, 1143–1145.

[27] Gottler, L.M.; Lee, H.-Y.; Shelburne, C.E.; Ramamoorthy, A.; Marsh, E.N.G. Using Fluorous Amino Acids to Modulate the Biological Activity of an Antimicrobial Peptide. *ChemBioChem*, **2008**, *9*, 370–373.

[28] Ramamoorthy, A.; Thennarasu, S.; Lee, D.-K.; Tan, A.; Maloy, L. Solid-State NMR Investigation of the Membrane-Disrupting Mechanism of Antimicrobial Peptides MSI-78 and MSI-594 Derived From Magainin 2 and Melittin. *Biophys J*, **2006**, *91*, 206–216.

[29] Buer, B.C.; Chugh, J.; Al-Hashimi, H.M.; Marsh, E.N.G. Using Fluorine Nuclear Magnetic Resonance to Probe the Interaction of Membrane-Active Peptides with the Lipid Bilayer. *Biochemistry*, **2010**, *49*, 5760–5765.

[30] Santos, O.; Kosoric, J.; Hector, M.P.; Anderson, P.; Lindh, L. Adsorption Behavior of Statherin and a Statherin Peptide Onto Hydroxyapatite and Silica Surfaces by *In Situ* Ellipsometry. *J Colloid Interface Sci*, **2008**, *318*, 175–182.

[31] Cambell, C.T.; Kim, G. SPR Microscopy and Its Applications to High-Throughput Analyses of Biomolecular Binding Events and Their Kinetics. *Biomaterials*, **2007**, *28*, 2380–2392.

[32] Mozsolits, H.; Aguilar, M.-I. Surface Plasmon Resonance Spectroscopy: an Emerging Tool for the Study of Peptide-Membrane Interactions. *Biopolymers*, **2002**, *66*, 3–18.

[33] Vanea, E.; Simon, V. XPS Study of Protein Adsorption Onto Nanocrystalline Aluminosilicate Microparticles. *Appl Surf Sci*, **2011**, *257*, 2346–2352.

[34] Baugh, L.; Weidner, T.; Baio, J.E.; Nguyen, P.-C.T.; Gamble, L.J.; Stayton, P.S.; Castner, D.G. Probing the Orientation of Surface-Immobilized Protein G B1 Using ToF-SIMS, Sum Frequency Generation, and NEXAFS Spectroscopy. *Langmuir*, **2010**, *26*, 16434–16441.

[35] Henry, M.; Dupont-Gillain, C.; Bertrand, P. Conformation Change of Albumin Adsorbed on Polycarbonate Membranes as Revealed by ToF-SIMS. *Langmuir*, **2003**, *19*, 6271–6276.

[36] Wagner, M.S.; McArthur, S.L.; Shen, M.; Horbett, T.A.; Castner, D.G. Limits of Detection for Time of Flight Secondary Ion Mass Spectrometry (ToF-SIMS) and X-Ray Photoelectron Spectroscopy (XPS): Detection of Low Amounts of Adsorbed Protein. *J Biomater Sci, Polym Ed*, **2002**, *13*, 407–428.

[37] Groß, P.C.; Zeppezauer, M. Infrared Spectroscopy for Biopharmaceutical Protein Analysis. *J Pharm Biomed Anal*, **2010**, *53*, 29–36.

[38] Sharon, M.; Oren, Z.; Shai, Y.; Anglister, J. 2D-NMR and ATR-FTIR Study of the Structure of a Cell-Selective Diastereomer of Melittin and Its Orientation in Phospholipids. *Biochemistry*, **1999**,

38, 15305–15316.

[39] Chittur, K.K. FTIR/ATR for Protein Adsorption to Biomaterial Surfaces. *Biomaterials*, **1998**, *19*, 357–369.

[40] Tatulian, S.A.; Jones, L.R.; Reddy, L.G.; Stokes, D.L.; Tamm, L.K. Secondary Structure and Orientation of Phospholamban Reconstituted in Supported Bilayers From Polarized Attenuated Total Reflection FTIR Spectroscopy. *Biochemistry*, **1995**, *34*, 4448–4456.

[41] Wen, Z.-Q.; Li, G.; Ren, D. Detection of Trace Melamine in Raw Materials Used for Protein Pharmaceutical Manufacturing Using Surface-Enhanced Raman Spectroscopy (SERS) with Gold Nanoparticles. *Appl Spectrosc*, **2011**, *65*, 514–521.

[42] Zhu, X.; Suhr, H.; Shen, Y.R. Surface Vibrational Spectroscopy by Infrared-Visible Sum Frequency Generation. *Phys Rev B*, **1987**, *35*, 3047–3050.

[43] Lambert, A.G.; Davies, P.B.; Neivandt, D.J. Implementing the Theory of Sum Frequency Generation Vibrational Spectroscopy: a Tutorial Review. *Appl Spectrosc Rev*, **2005**, *40*, 103–145.

[44] Nguyen, K.T.; Le Clair, S.V.; Ye, S.; Chen, Z. Orientation Determination of Protein Helical Secondary Structures Using Linear and Nonlinear Vibrational Spectroscopy. *J Phys Chem B*, **2009**, *113*, 12169–12180.

[45] Liu, Y.; Ogorzalek, T.L.; Yang, P.; Schroeder, M.M.; Marsh, E.N.G.; Chen, Z. Molecular Orientation of Enzymes Attached to Surfaces Through Defined Chemical Linkages at the Solid–Liquid Interface. *J Am Chem Soc*, **2013**, *135*, 12660–12669.

[46] Yang, P.; Glukhova, A.; Tesmer, J.J.G.; Chen, Z. Membrane Orientation and Binding Determinants of G Protein-Coupled Receptor Kinase 5 as Assessed by Combined Vibrational Spectroscopic Studies. *PLoS ONE*, **2013**, *8*, e82072–11.

[47] Nguyen, K.T.; Le Clair, S.V.; Ye, S.; Chen, Z. Molecular Interactions Between Magainin 2 and Model Membranes *In Situ*. *J Phys Chem B*, **2009**, *113*, 12358–12363.

[48] Chen, H.-Y.; Lahann, J. Surface Patterning Strategies for Microfluidic Applications Based on Functionalized Poly-*P*-Xylylenes. *Bioanalysis*, **2010**, *2*, 1717–1728.

[49] Ross, A.; Durmaz, H.; Cheng, K.; Deng, X.; Liu, Y.; Oh, J.; Chen, Z.; Lahann, J. Selective and Reversible Binding of Thiol-Functionalized Biomolecules on Polymers Prepared via Chemical Vapor Deposition Polymerization. *Langmuir*, **2015**, A–G.

[50] Shen, Y.R. Surface Properties Probed by Second-Harmonic and Sum-Frequency Generation. *Nature*, **1989**, *337*, 519–525.

[51] Zhuang, X.; Miranda, P.B.; Kim, D.; Shen, Y.R. Mapping Molecular Orientation and Conformation at Interfaces by Surface Nonlinear Optics. *Phys Rev B*, **1999**, *59*, 12632–12640.

[52] Chen, Z.; Shen, Y.R.; Somorjai, G.A. Studies of Polymer Surfaces by Sum Frequency Generation Vibrational Spectroscopy. *Annu Rev Phys Chem*, **2002**, *53*, 437–465.

[53] Fu, L.; Liu, J.; Yan, E.C.Y. Chiral Sum Frequency Generation Spectroscopy for Characterizing Protein Secondary Structures at Interfaces. *J Am Chem Soc*, **2011**, *133*, 8094–8097.

[54] Xiao, D.; Fu, L.; Liu, J.; Batista, V.S.; Yan, E.C.Y. Amphiphilic Adsorption of Human Islet Amyloid Polypeptide Aggregates to Lipid/Aqueous Interfaces. *J Mol Bio*, **2012**, *421*, 537–547.

[55] Kim, J.; Cremer, P.S. Elucidating Changes in Interfacial Water Structure Upon Protein Adsorption. *ChemPhysChem*, **2001**, *2*, 543–546.

[56] Kim, G.; Gurau, M.; Kim, J.; Cremer, P.S. Investigations of Lysozyme Adsorption at the Air/Water and Quartz/Water Interfaces by Vibrational Sum Frequency Spectroscopy. *Langmuir*, **2002**, *18*, 2807–2811.

[57] Kim, J.; Kim, G.; Cremer, P.S. Investigations of Polyelectrolyte Adsorption at the Solid/Liquid Interface by Sum Frequency Spectroscopy: Evidence for Long-Range Macromolecular

Alignment at Highly Charged Quartz/Water Interfaces. *J Am Chem Soc*, **2002**, *124*, 8751–8756.

[58] Roy, S.; Covert, P.A.; FitzGerald, W.R.; Hore, D.K. Biomolecular Structure at Solid–Liquid Interfaces as Revealed by Nonlinear Optical Spectroscopy. *Chem Rev*, **2014**, *114*, 8388–8415.

[59] Kim, J.; Somorjai, G.A. Molecular Packing of Lysozyme, Fibrinogen, and Bovine Serum Albumin on Hydrophilic and Hydrophobic Surfaces Studied by Infrared−Visible Sum Frequency Generation and Fluorescence Microscopy. *J Am Chem Soc*, **2003**, *125*, 3150–3158.

[60] Onorato, R.M.; Yoon, A.P.; Lin, J.T.; Somorjai, G.A. Adsorption of Amino Acids and Dipeptides to the Hydrophobic Polystyrene Interface Studied by SFG and QCM: the Special Case of Phenylalanine. *J Phys Chem C*, **2012**, *116*, 9947–9954.

[61] McCrea, K.; Parker, J.S.; Chen, P.; Somorjai, G. Surface Structure Sensitivity of High-Pressure CO Dissociation on Pt(557), Pt(100) and Pt(111) Using Sum Frequency Generation Surface Vibrational Spectroscopy. *Surf Sci*, **2001**, *494*, 238–250.

[62] Lu, X.; Shephard, N.; Han, J.; Xue, G.; Chen, Z. Probing Molecular Structures of Polymer/Metal Interfaces by Sum Frequency Generation Vibrational Spectroscopy. *Macromolecules*, **2008**, *41*, 8770–8777.

[63] Lu, X.; Xue, G.; Wang, X.; Han, J.; Han, X.; Hankett, J.; Li, D.; Chen, Z. Directly Probing Molecular Ordering at the Buried Polymer/Metal Interface 2: Using P-Polarized Input Beams. *Macromolecules*, **2012**, *45*, 6087–6094.

[64] Ye, S.; Nguyen, K.T.; Boughton, A.P.; Mello, C.M.; Chen, Z. Orientation Difference of Chemically Immobilized and Physically Adsorbed Biological Molecules on Polymers Detected at the Solid/Liquid Interfaces *In Situ*. *Langmuir*, **2010**, *26*, 6471–6477.

[65] Ye, S.; Li, H.; Wei, F.; Jasensky, J.; Boughton, A.P.; Yang, P.; Chen, Z. Observing a Model Ion Channel Gating Action in Model Cell Membranes in Real Time in Situ: Membrane Potential Change Induced Alamethicin Orientation Change. *J Am Chem Soc*, **2012**, *134*, 6237–6243.

[66] Yatawara, A.K.; Tiruchinapally, G.; Bordenyuk, A.N.; Andreana, P.R.; Benderskii, A.V. Carbohydrate Surface Attachment Characterized by Sum Frequency Generation Spectroscopy. *Langmuir*, **2009**, *25*, 1901–1904.

[67] Wang, J.; Even, M.A.; Chen, X.; Schmaier, A.H.; Waite, J.H.; Chen, Z. Detection of Amide I Signals of Interfacial Proteins *In Situ* Using SFG. *J Am Chem Soc*, **2003**, *125*, 9914–9915.

[68] Chen, X.; Wang, J.; Sniadecki, J.J.; Even, M.A.; Chen, Z. Probing A-Helical and B-Sheet Structures of Peptides at Solid/Liquid Interfaces with SFG. *Langmuir*, **2005**, *21*, 2662–2664.

[69] Ding, B.; Chen, Z. Molecular Interactions Between Cell Penetrating Peptide Pep-1 and Model Cell Membranes. *J Phys Chem B*, **2012**, *116*, 2545–2552.

[70] Wei, S.; Knotts, T.A. A Coarse Grain Model for Protein-Surface Interactions. *J Chem Phys*, **2013**, *139*, 095102–095112.

[71] Karanicolas, J.; Brooks, C.L., III. Integrating Folding Kinetics and Protein Function: Biphasic Kinetics and Dual Binding Specificity in a WW Domain. *P Natl Acad Sci*, **2004**, *101*, 3432–3437.

[72] Karanicolas, J.; Brooks, C.L., III. The Structural Basis for Biphasic Dinetics in the Folding of the WW Domain From a Formin-Binding Protein: Lessons for Protein Design? *P Natl Acad Sci*, **2003**, *100*, 3954–3959.

[73] Wei, Y.; Latour, R.A. Benchmark Experimental Data Set and Assessment of Adsorption Free Energy for Peptide−Surface Interactions. *Langmuir*, **2009**, *25*, 5637–5646.

[74] Li, Y.; Wei, S.; Wu, J.; Jasensky, J.; Xi, C.; Li, H.; Xu, Y.; Wang, Q.; Marsh, E.N.G.; Brooks, C.L., III; Chen, Z. Effects of Peptide Immobilization Sites on the Structure and Activity of Surface-Tethered Antimicrobial Peptides. *J Phys Chem C*, **2015**, *119*, 7146–7155.

[75] Onaizi, S.A.; Leong, S.S.J. Tethering Antimicrobial Peptides: Current Status and Potential Challenges. *Biotechnol Adv*, **2011**, *29*, 67–74.

CHAPTER 3: Development of Broadband Coherent Anti-Stokes Raman Scattering (CARS) Microscopy for Live-Cell Imaging and Singular Value Decomposition (SVD) for Image Analysis

Portions of this chapter have been adapted from the following reference:

Khmaladze A, **Jasensky J**, Price E, Zhang C, Boughton AP, Han XF, Seeley E, Liu X, Banaszak Holl MM, Chen Z. Hyperspectral Imaging and Characterization of Live Cells by Broadband Coherent Anti-Stokes Raman Scattering (CARS) Microscopy with Singular Value Decomposition (SVD) Analysis. *Appl. Spectrosc.* **2014**, 68(10):1116-1122.

3.1 Introduction

Raman microscopy has provided a direct way of imaging unstained, live cells with chemical selectivity and without the need for fixation. The Raman process originates from an inelastic scattering event between photon and chemical bond, where energy transfer occurs, either from the bond to the photon, or visa versa. Since different bonds not only have different strengths, but are also tether different molecules, most chemical groups have unique Raman signals. This not only helps generate imaging contrast (based on molecular vibrations of these molecules), but also is noninvasive, since the imaging molecules are inherent to the biological cell or tissue.

Because of its unique imaging capability, Raman has been implemented in a variety of biomedical applications such as DNA and glucose detection [1,2], tumor diagnostics [3,4], microendoscopy [5], as well as tissue [6,7] and single-cell imaging [8]. Infrared (IR) imaging, another microscopy based in imaging vibrational content, often is not ideal

for such applications, since it is prone to high water absorption (often a critical component of biological systems) and has poor spatial resolution.

Despite of its advantages, Raman scattering also has its limitations. Spontaneous Raman scattering, which was previously referred to as “Raman scattering” is non-directional, so emission of signal is isotropic. This often results in long acquisition times and is not practical for sensitive samples [9,10]. This limits potential applications of spontaneous Raman microscopy in dynamic living systems and samples sensitive to external perturbation.

Such limitations can be circumvented by using multi-photon, vibrational coherent anti-Stokes Raman scattering (CARS) microscopy [11,12]. The development of CARS has improved upon the limitations of spontaneous Raman therefore making it feasible to image living samples without the need for cellular fixation or exogenous labels that may perturb the observed system [13].

As discussed in **Section 1.3**, coherent anti-Stokes Raman scattering is a nonlinear optical process involving three input photons and one outgoing photon. These three input photons drive molecular vibrations and force vibrational resonators in the sample to oscillate in phase. The resulting effect is that all signal photons scatter directionally, making signal collection much more efficient. CARS intensity is greatly enhanced when the frequency difference between the pump and Stokes beams, the two beams required for the CARS process, matches the frequency of a Raman resonance [14]. Therefore,

by recording this intensity as a function of the frequency difference between pump and Stokes wavelengths and as a function of sample position, it is possible to obtain spectroscopic information visually, by monitoring the distribution of a particular chemical across a live cell or tissue.

Here, we employ a broadband CARS technique, where spectrally narrow pump beam is coupled with spectrally broad Stokes pulse (see **Fig 3.1**). As a result, multiple Raman transitions are excited within the bandwidth of the Stokes pulse and probed with the narrow probe beam, which makes it possible to generate an entire CARS spectrum in one acquisition. When this technique is used together with a scanning microscope, an image can be acquired wherein each pixel contains the entire vibrational spectrum at that point, forming a hyperspectral CARS image.

In order to extract chemical profiles consisting of multiple spectral peaks, data mining techniques must be used. Examples such as principal component analysis [15-17], hierarchical cluster analysis [18], classical least-squares analysis [19], and singular value decomposition analysis [20-22] have been used in a variety of biological/polymer-based systems. Singular value decomposition (SVD) was, in our case, the most appropriate technique for assigning image pixels to regions of different chemical composition, because it did so without requiring prior knowledge of the spectra of the pure components.

Our device and analysis methods are well suited for qualitative studies that seek to

determine regions of different chemical composition within a cell. We demonstrate several practical applications of our hyperspectral CARS imaging technique to unlabeled biological systems. We also demonstrate the feasibility to use CARS imaging to distinguish different chemical compositions in noisy images, even when the spectra for the pure compounds would share similar or overlapping peak centers that could not be distinguished using single-wavelength imaging.

3.2 Device Design

Our experimental setup is schematically illustrated in **Fig 3.1**. The pump and Stokes beams required to drive the CARS process originate from a single Ti:Sapphire (Spectra Physics) tunable oscillator operating at 800 nm, ~150 fs, and 80 MHz, and a photonic crystal fiber (PCF, NKT Photonics), respectively.

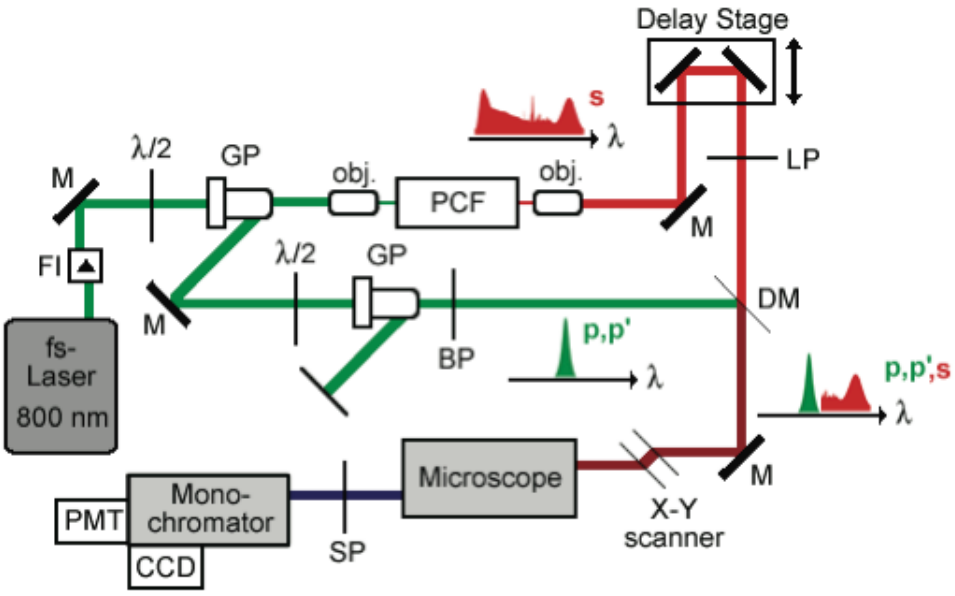

Figure 3.1: Schematic of CARS Design. FI: Faraday Isolator, GP: Glan-Taylor Prism, BP/LP/SP: band/long/short pass filter, DM: dichroic mirror, PCF: photonic crystal fiber. A single laser source provides a narrowband pump pulse (green) as well as broadband Stokes pulse (red) using a PCF. With a broadband source, two methods of detection were used for live cell imaging: univariate (with PMT) and multivariate (with CCD) CARS imaging.

The measured oscillator bandwidth full-width at half max (FWHM) is around 12 nm at its operating wavelength. This bandwidth is the determining factor in the observed spectral resolution of CARS. Unfortunately, this is too large to visualize any spectral features and must be narrowed. This is achieved by a 3 nm bandpass filter, which optimized our spectra resolution to ~50 cm^{-1}. The spectral width of the Stokes beam, however, must be large enough to capture all relevant chemical information in the sample. The broadband Stokes beam, and corresponding PCF, are some of the main components required for hyperspectral CARS imaging [23-27].

In order to generate CARS signal, both pump and Stokes beams must have spatial and temporal alignment. When this condition is met, both beams are phase matched [11]. Spatial alignment is achieved by both a long-pass filter and a dichroic mirror; the combination of these two elements pass the infrared (IR) component of the Stokes beam (required for CARS), and reflect the lower wavelength pump beam. As for temporal alignment, this is achieved by passing the Stokes beam through a delay line; a physical delay forces a temporal delay and matches the path length of the pump beam.

For tight focusing required for CARS signal generation and effective sample illumination, we used a 40x objective, standard or water immersion, and an x,y galvanometer scanner (Thorlabs). The power measured at the sample was 6 mW. A condenser lens collected the forward CARS signal. After the remaining pump and Stokes light was filtered out, the signal was sent to a spectrometer (Oriel MS257 with

adjustable entrance and exit slits), which housed both a photomultiplier (PMT) detector used for single-wavelength imaging and a charge-coupled device (CCD) camera for multi-wavelength spectral acquisition. The optical system is designed in such a way that the scanning mirror is imaged onto an entrance slit of the spectrometer, eliminating the need for descanning the signal beam. A set of Labview programs were developed to control laser scanning, collect the CARS signal from both PMT and CCD detectors, and analyze the hyperspectral data.

Photomultiplier-based image and spectral acquisition was performed similarly to any traditional scanning microscope system: The intensity on the PMT was read at a particular wavelength by adjusting the position of the diffraction grating inside the monochromator. The second monochromator port hosted a CCD camera (Oriel InstaSpec X model 78237), which permitted simultaneous detection within a broad (800 cm^{-1}) spectral range. The location of this spectral range could be adjusted by moving the grating.

Thus, our broadband CARS setup is capable of acquiring hyperspectral CARS images in two ways. The first is a PMT-based detection method, which acquires a sequence of CARS images at different wavelengths. If we are interested in a CARS spectrum at a particular point, it can be subsequently reconstructed from the stack of the different wavelength images by recording the intensity at this point as a function of wavelength/wavenumber.

The second method is based on the simultaneous detection of a portion of the spectrum by a CCD camera, coupled with point-by-point x,y laser scanning. Since for our setup the CARS signals at different wavelengths are generated simultaneously by scanning the beam over the sample and recording the entire spectrum at each point, we acquired a hyperspectral image of the sample. After the spectra for all image points have been acquired, this 3D data set can then be displayed as a series of images corresponding to individual wavelengths/wavenumbers.

Due to the strong, first-order Rayleigh scattering of the laser beams from the sample, by placing a photodiode at the exit of the scanning microscope, it was possible to produce an optical scanning image of the sample simultaneously with the CARS image [28]. This optical scanning image has the same spatial resolution as the CARS image (around 500 nm), and the depth of focus was experimentally measured to be 1 μm.

3.3 Hyperspectral Data Analysis

The goal for data analysis in broadband CARS is to identify each independent chemical profile of a given sample. Often biological samples consist of many biomolecules (e.g. DNA [29,30], sugar [31], and lipid [32]) or localized chemical structures (e.g. atherosclerosis plaques [16,33,34] or cancer [35]). Procedures such as k-means clustering [36] and principle component analysis [17], are less tolerant to noise and often require more assumptions. In contrast, singular value decomposition [22] does not need prior knowledge of chemical composition and provided consistent results across all experiments.

Singular value decomposition (SVD) can be understood with three different viewpoints. On the one hand, we can see it as a method for transforming correlated variables into a set of uncorrelated ones that better expose the various relationships among the original data items. At the same time, SVD is a method for identifying and ordering dimensions along which data points exhibit the most variation. This ties in to the third way of viewing SVD (and the one that ties in with our objective the best), which is that once we have identified where the most variation is, it is possible to find the best approximation of the original data points using fewer dimensions. This, in essence, allows us to identify unique repeating structures in our data (i.e. chemical components) and visualize their distribution in the original image.

Mathematically, we see that SVD takes the form of:

$$M = U\Sigma V^* \tag{3.1}$$

where M is the ensemble of measured spectra (input data), U is the rotation from new to old basis (component spectra), Σ is a matrix of diagonal singular values (how often a single component spectra occurs, and V^* is measured spectra in the new basis (component images). Elements of **Equation (3.1)** will be discussed in the next section with an application of SVD in analyzing a polymer composite.

In practice, SVD was run on raw, unprocessed hyperspectral imaging data arranged as an array of *m* variables x *n* spectra, using the “economy-sized” SVD implementation in MATLAB R2011a. The resulting right and left singular vectors can respectively be

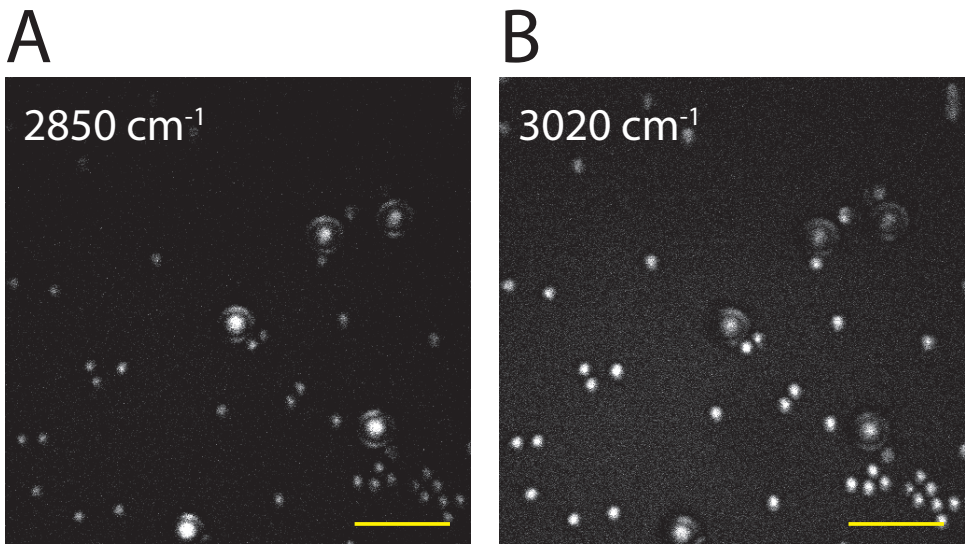

Figure 3.2: Single-Wavelength Images of Polymer Beads. CARS images acquired at (A) 2850 cm^{-1} and (B) 3020 cm^{-1}. Images show bright, localized regions corresponding to large PMMA beads and smaller PS spheres. The different sizes of beads lead to the apparent rings on PMMA, as these larger particles are not entirely in focus while PS is being imaged. Scale bars 20 μm.

---

described as component lineshapes and weighted contributions of all components to each spectrum in the dataset. Since each pixel from a single image contains repeating spectral features, the first several component lineshapes generated from SVD describe all vibrational content in the system, and from this, these component lineshapes often resemble those that would be obtained from constituent chemical components.

3.4 Applications of SVD on Hyperspectral CARS Data

3.4.1 Polymer Bead Mixtures.

Our first proof-of-method experiments were to demonstrate clear identification and separation of two distinct chemical components, polystyrene (PS) and poly(methyl methacrylate) (PMMA) within the same CARS image.

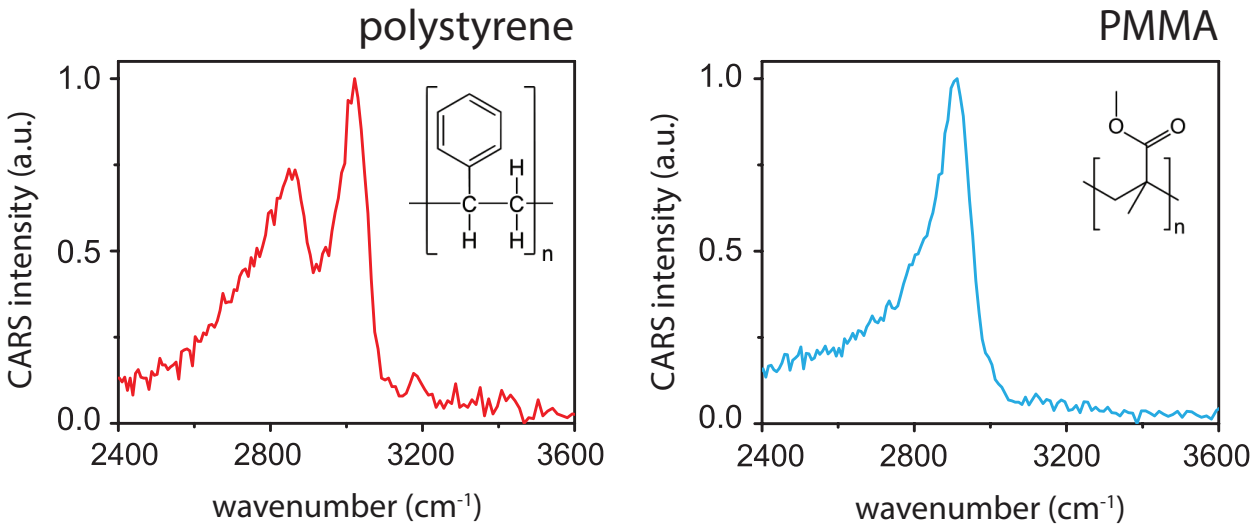

Figure 3.3: CARS Spectra of PS and PMMA. PS and PMMA have overlapping spectral features between them making single-wavelength CARS imaging difficult. Chemical structures added for clarity.

3.4.1.1 Materials and Methods.

A mixture of polymer beads was prepared by mixing aqueous suspensions of 3 μm polystyrene (PS) (Sigma-Aldrich) and 8 μm poly(methyl methacrylate) (PMMA) microspheres (Fluka Analytical). Mixtures were plated on glass slides and dried before imaging.

3.4.1.2 Results and Discussion.

Fig 3.2 shows CARS images of a mixture of poly(methyl methacrylate) and polystyrene beads acquired by PMT detection at the aliphatic CH stretching region of 2850 cm^{-1} (**Fig. 3.2 *A***) and the aromatic CH stretching region at 3020 cm^{-1} (**Fig. 3.2 *B***). As expected, PS produces signal at both the aliphatic and aromatic CH stretching regions (**Fig 3.3**), limiting the ability of single-intensity measurements.

Alternately, CCD detection allows for obtaining spectral information for each point. Images acquired at only a single wavelength may show bright or dark spots due to factors other than a change in chemical composition. Within the image frame, the intensity of the pump/probe or Stokes beam may vary, producing an uneven distribution of CARS signal even if the sample is uniform. For example, as shown in **Fig 3.2**, the edges of the beads appear dimmer than the center due to the sample's geometry (a change in the orientation of the bead surface with respect to the scanning beams). For the above reasons, a single-wavelength CARS image contains both chemical and optical information. Finally, it is also affected by the interference between the on- and off-resonance signals, as well as non-resonant contribution of the cover slip and/or medium.

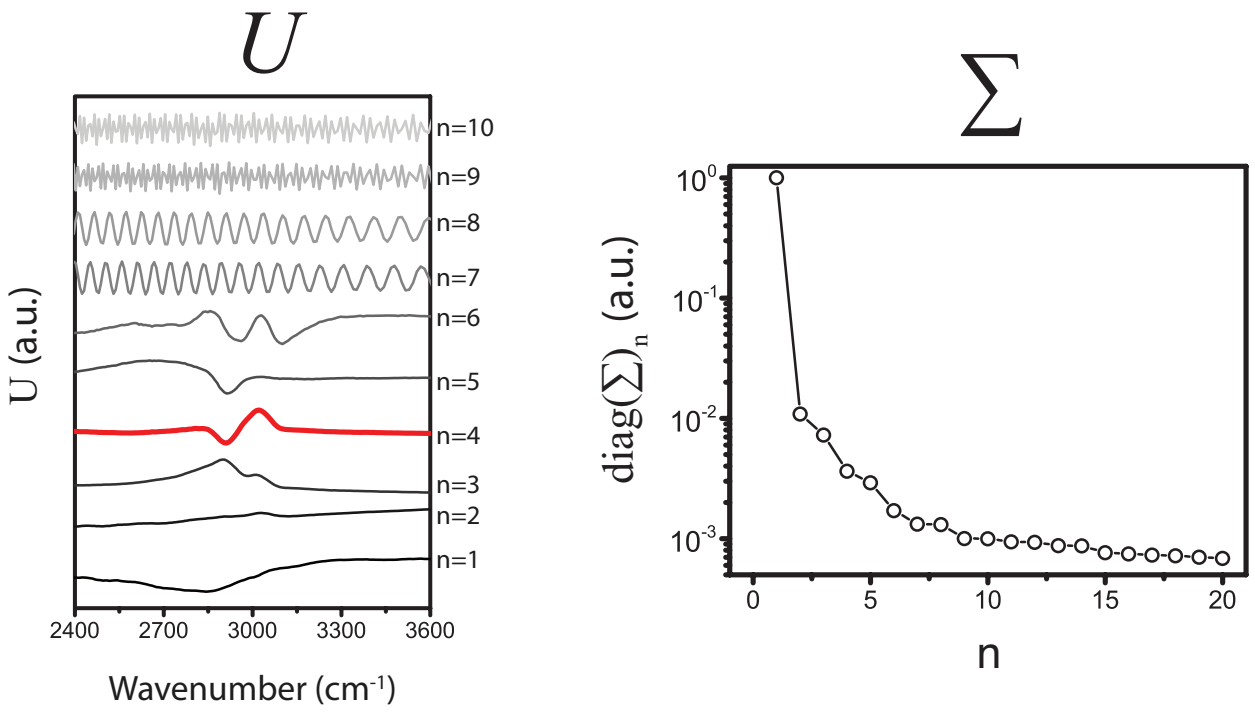

Figure 3.4: SVD Elements. Component spectra (U) and component weighting (sigma) for PS/PMMA mixture. Component 4 shows the best image spatial contrast when plotted against original image. Only first 6 of 22500 components contain non-noise features, and after component 5, occurrence of higher "n" components is minimal.

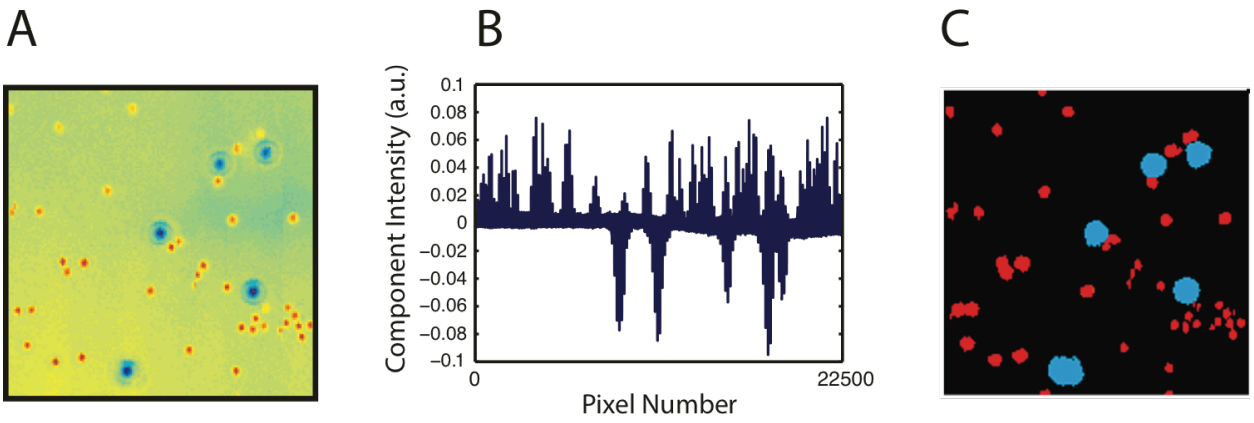

Figure 3.5: Chemical Identification via SVD. (A) Component 4 plotted against the original CARS image uniquely identifies PS from PMMA from background. (B) Looking at component intensity (weighting) across each pixel allows user to set threshold values. (C) Resulting image after thresholds are set. All three components are separately identified.

Hyperspectral imaging allows decoupling of the chemical and optical information via comparison of overall spectral line shapes in different regions, thus enabling more detailed and accurate classification of the chemical composition of the sample. Running SVD produces two pieces of information: (1) component spectra (U) which are the new orthogonal basis vectors (minimal components that show maximum variation), as well as (2) the singular values (the frequency at which each component occurs). By inspection, it is clear that of the 22500 spectral components, for every pixel in the image, only the first 6 contain non-noise features. Therefore, all other components can be ignored. Moreover, there is a significant decline in the frequency of observed components past n=6, and therefore is further justification of negligible contributions for these components.

Component 4, highlighted in red in **Fig 3.4**, shows similarity to the spectral signatures of PS and PMMA. When this component is plotted against the original image (**Fig 3.5 *A***),

we can see clear separation between each polymer. This is verified by the size difference between PS and PMMA, which removes uncertainty in SVD-based identification. When the component intensity is plotted across each pixel (**Fig 3.5 *B***), this separation between polymers is also apparent. From this piece of data, threshold values can be set, and a tricolor image can be generated highlighting each component more clearly (**Fig 3.5 *C***).

3.4.2 Live Cell CARS Imaging.

Since CARS microscopy is an ideal tool for noninvasive live cell imaging, our next goal was to identify lipid droplets in cell types known to readily accumulate lipid. More details

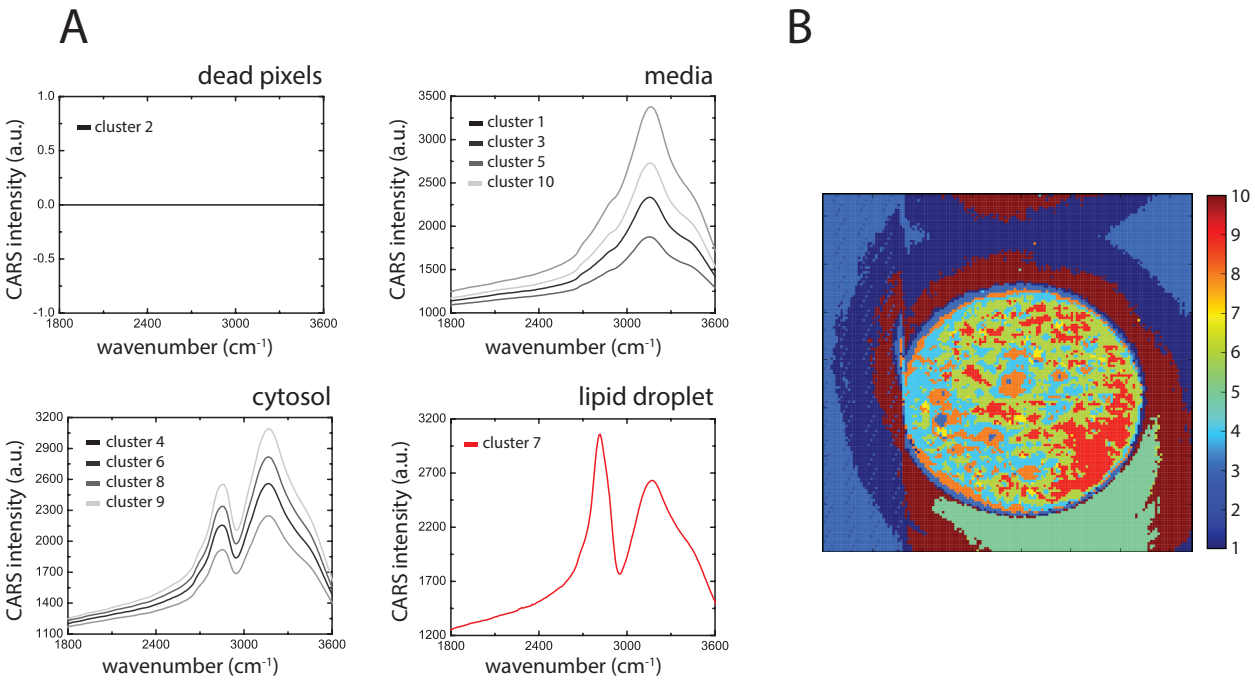

Figure 3.6: K-Means Clustering Analysis on Live Cell Images. (A) Representative spectra from each of the 10 clusters. Different regions of the image have varying amounts of CH (2850 cm^{-1}) and OH (3100 cm^{-1}). It was only after 10 clusters that k-means was able to identify a component representative of lipid (component 7). Clusters are not based on shape; same lineshape but different intensity is grouped into a different cluster. (B) K-means clusters superimposed on top of original CARS image. Color bar identifies k-means clusters.

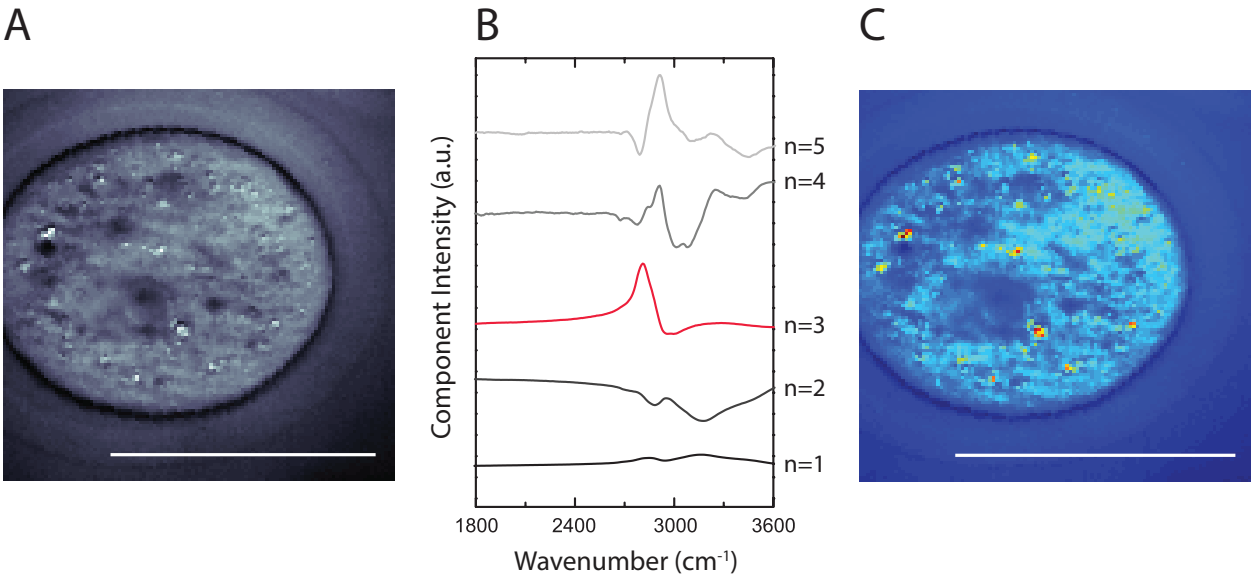

Figure 3.7: SVD Analysis on Live Cells. (A) CARS image of a live oocyte. (B) After running SVD, component spectra are plotted. Component 3 shows the most similarity to the lipid droplet spectrum. (C) Component 3 plotted against the original image recovers lipid signal seen in (A). Scale bar 50 μm.

---

of the cells and the biological significance of their lipid can be found in **Chapter 4**.

3.4.2.1 Materials and Methods .

Details of oocyte collection and preparation can be found in **Section 4.2**.

3.4.2.2 Results and Discussion.

In order to assess the best data mining technique for live-cell imaging for non-ideal conditions (large noise and non-uniform sample illumination), both k-means clustering and SVD were compared in their ability to accurately identify lipid content in mouse oocytes. Overall, we were searching for a method that accurately identifies only unique chemical spectra in hyperspectral images of multiple chemical compositions. K-means clustering is a technique which partitions *n* number of observations (in this case,

spectra) into *k* clusters. These clusters are defined and represented by their mean. Any spectra features including peak centers, peak heights, etc. will be variables that k-means clustering will consider. Details of SVD and it's implementation in hyperspectral CARS data sets are discussed in **Chapter 4**.

Fig 3.6 depicts representative results of k-means clustering from a typical oocyte image under normal imaging conditions. Unfortunately, due to the quality of CARS data, k-means clustering required 10 cluster assignments in order to identify pixels as lipids; here we define lipid droplets as pixels which have a stronger peak at the CH stretching region (2850 cm^{-1}) in comparison to the OH stretching region (3100 cm^{-1}).

Spectral signatures in **Fig 3.6** ***A*** show similar peak shapes, and only their intensity differs. Those peaks are grouped according to shape and identified as either pixels with no information (dead pixels), media, cytosol, or lipid droplet. An image representing all 10 clusters is shown in **Fig 3.6** ***B***.

As demonstrated in this example, k-means clustering did not produce a concise result when image quality is moderately high. The biggest disadvantage of k-means clustering is its inability to identify components by peak shape only; intensity variation is factored into the selection of clusters.

For comparison, the same oocyte and data set were analyzed by SVD. Results of this are shown in **Fig 3.7**. The original CARS image (**Fig 3.7** ***A***) does show bright, localized

signal at various locations in the cell, indicating lipid droplets. The resulting SVD component spectra (**Fig 3.7** ***B***) highlight spectral features similar to those seen in the cluster assignments from **Fig 3.6**. Choosing the component that best represents lipid droplet (n=3) and plotting that against **Fig 3.7** ***A*** (shown in **Fig 3.7** ***C***) produces an image nearly identical in how lipids are visualized. Even for more noise-heavy data, SVD was still able to accurately identify lipid droplets better than k-means clustering.

3.5 Conclusion

In conclusion, broadband CARS microscopy is a unique tool with promising applications in noninvasive analysis. Its ability to image with chemical contrast and without the need for cellular fixation or harsh labeling is ideal in nonterminal studies where delicate samples are often needed for further testing. The use of a photonic crystal fiber and CCD detection makes hyperspectral CARS imaging possible, and singular value decomposition was the best method we found for image analysis and independently identifying important chemical species. It is this technology that we will use to answer important biological questions about the importance of lipid and its role in cellular homeostasis as well as a biomarker for cell health.

3.6 References

[1] Berger, A.J.; Itzkan, I.; Feld, M.S. Feasibility of Measuring Blood Glucose Concentration by Near-Infrared Raman Spectroscopy. *Spectrochim Acta A Mol Biomol Spectrosc*, **1997**, *53*, 287–292.

[2] Cao, Y.C.; Jin, R.; Mirkin, C.A. Nanoparticles with Raman Spectroscopic Fingerprints for DNA and RNA Detection. *Science*, **2002**, *297*, 1536–1540.

[3] Huang, Z.; McWilliams, A.; Lui, H.; McLean, D.I.; Lam, S.; Zeng, H. Near-Infrared Raman Spectroscopy for Optical Diagnosis of Lung Cancer. *Int J Cancer*, **2003**, *107*, 1047–1052.

[4] Nijssen, A.; Bakker Schut, T.C.; Heule, F.; Caspers, P.J.; Hayes, D.P.; Neumann, M.H.A.; Puppels, G.J. Discriminating Basal Cell Carcinoma From Its Surrounding Tissue by Raman Spectroscopy. *J Invest Dermatol*, **2002**, *119*, 64–69.

[5] Shim, M.G.; Wong Kee Song, L.-M.; Marcon, N.E.; Wilson, B.C. *In Vivo* Near-Infrared Raman Spectroscopy: Demonstration of Feasibility During Clinical Gastrointestinal Endoscopy. *Photochem Photobiol*, **2000**, *72*, 146–150.

[6] Khmaladze, A.; Ganguly, A.; Kuo, S.; Raghavan, M.; Kainkaryam, R.; Cole, J.H.; Izumi, K.; Marcelo, C.L.; Feinberg, S.E.; Morris, M.D. Tissue-Engineered Constructs of Human Oral Mucosa Examined by Raman Spectroscopy. *Tissue Eng Pt C-Meth*, **2013**, *19*, 299–306.

[7] Marzec, K.M.; Kochan, K.; Fedorowicz, A.; Jasztal, A.; Chruszcz-Lipska, K.; Dobrowolski, J.C.; Chlopicki, S.; Baranska, M. Raman Microimaging of Murine Lungs: Insight Into the Vitamin a Content. *Analyst*, **2015**, *140*, 2171–2177.

[8] Rusciano, G.; Pesce, G.; Salemme, M.; Selvaggi, L.; Vaccaro, C.; Sasso, A.; Carotenuto, R. Raman Spectroscopy of *Xenopus Laevis* Oocytes. *Methods*, **2010**, *51*, 27–36.

[9] Krafft, C.; Ramoji, A.A.; Bielecki, C.; Volger, N.; Meyer, T.; Akimov, D.; Rösch, P.; Schmitt, M.; Dietzek, B.; Petersen, I.; Stallmach, A.; Popp, J. A Comparative Raman and CARS Imaging Study of Colon Tissue. *J Biophotonics*, **2009**, *2*, 303–312.

[10] Cui, M.; Bachler, B.R.; Ogilvie, J.P. Comparing Coherent and Spontaneous Raman Scattering Under Biological Imaging Conditions. *Opt Lett*, **2009**, *34*, 773–775.

[11] Zumbusch, A.; Holtom, G.R.; Xie, X.S. Three-Dimensional Vibrational Imaging by Coherent Anti-Stokes Raman Scattering. *Phys Rev Lett*, **1999**, *82*, 4142–4145.

[12] Cheng, J.-X.; Xie, X.S. Coherent Anti-Stokes Raman Scattering Microscopy: Instrumentation, Theory, and Applications. *J Phys Chem B*, **2004**, *108*, 827–840.

[13] Zipfel, W.R.; Williams, R.M.; Christie, R.; Nikitin, A.Y.; Hyman, B.T.; Webb, W.W. Live Tissue Intrinsic Emission Microscopy Using Multiphoton-Excited Native Fluorescence and Second Harmonic Generation. *P Natl Acad Sci*, **2003**, *100*, 7075–7080.

[14] Tolles, W.M.; Nibler, J.W.; McDonald, J.R.; Harvey, A.B. A Review of the Theory and Application of Coherent Anti-Stokes Raman Spectroscopy (CARS). *Appl Spectrosc*, **1977**, *31*, 253–271.

[15] Lin, C.-Y.; Suhalim, J.L.; Nien, C.L.; Miljković, M.D.; Diem, M.; Jester, J.V.; Potma, E.O. Picosecond Spectral Coherent Anti-Stokes Raman Scattering Imaging with Principal Component Analysis of Meibomian Glands. *J Biomed Opt*, **2011**, *16*, 021104–1–021104–9.

[16] Lim, R.S.; Suhalim, J.L.; Miyazaki-Anzai, S.; Miyazaki, M.; Levi, M.; Potma, E.O.; Tromberg, B.J. Identification of Cholesterol Crystals in Plaques of Atherosclerotic Mice Using Hyperspectral CARS Imaging. *J Lipid Res*, **2011**, *52*, 2177–2186.

[17] Wold, S.; Esbensen, K.; Geladi, P. Principal Component Analysis. *Chemometr Intell Lab*, **1987**, *2*, 37–52.

[18] Arora, R.; Petrov, G.I.; Yakovlev, V.V. Hyperspectral Coherent Anti-Stokes Raman Scattering

Microscopy Imaging Through Turbid Medium. *J Biomed Opt*, *16*, 021116–1–021116–8.

[19] Lee, Y.J.; Moon, D.; Migler, K.B.; Cicerone, M.T. Quantitative Image Analysis of Broadband CARS Hyperspectral Images of Polymer Blends. *Anal Chem*, **2011**, *83*, 2733–2739.

[20] Masia, F.; Glen, A.; Stephens, P.; Borri, P.; Langbein, W. Quantitative Chemical Imaging and Unsupervised Analysis Using Hyperspectral Coherent Anti-Stokes Raman Scattering Microscopy. *Anal Chem*, **2013**, *85*, 10820–10828.

[21] Khmaladze, A.; Jasensky, J.; Price, E.; Zhang, C.; Boughton, A.P.; Han, X.; Seeley, E.; Liu, X.; Banaszak Holl, M.M.; Chen, Z. Hyperspectral Imaging and Characterization of Live Cells by Broadband Coherent Anti-Stokes Raman Scattering (CARS) Microscopy with Singular Value Decomposition (SVD) Analysis. *Appl Spectrosc*, **2014**, *68*, 1116–1122.

[22] Klema, V.C.; Laub, A.J. The Singular Value Decomposition: Its Computation and Some Applications. *IEEE T Automat Contr*, **1980**, *25*, 164–176.

[23] Kee, T.W.; Cicerone, M.T. Simple Approach to One-Laser, Broadband Coherent Anti-Stokes Raman Scattering Microscopy. *Opt Lett*, **2004**, *29*, 2701–2703.

[24] Parekh, S.H.; Lee, Y.J.; Aamer, K.A.; Cicerone, M.T. Label-Free Cellular Imaging by Broadband Coherent Anti-Stokes Raman Scattering Microscopy. *Biophys J*, **2010**, *99*, 2695–2704.

[25] van Vacano, B.; Meyer, L.; Motzkus, M. Rapid Polymer Blend Imaging with Quantitative Broadband Multiplex CARS Microscopy. *J Raman Spectrosc*, **2007**, *38*, 916–926.

[26] Kano, H.; Hamaguchi, H.-O. *In-Vivo* Multi-Nonlinear Optical Imaging of a Living Cell Using a Supercontinuum Light Source Generated From a Photonic Crystal Fiber. *Opt Express*, **2006**, *14*, 2798–2804.

[27] Camp, C.H., Jr; Lee, Y.J.; Heddleston, J.M.; Hartshorn, C.M.; Walker, A.R.H.; Rich, J.N.; Lathia, J.D.; Cicerone, M.T. High-Speed Coherent Raman Fingerprint Imaging of Biological Tissues. *Nat Photonics*, **2014**, *8*, 627–634.

[28] Khmaladze, A.; Kim, M. Design and Imaging Properties of a Laser Scanning Microscope with a Position-Sensitive Detector. *J Mod Optic*, **2008**, *55*, 2785–2796.

[29] Uzunbajakava, N.; Lenferink, A.; Kraan, Y.; Volokhina, E.; Vrensen, G.; Greve, J.; Otto, C. Nonresonant Confocal Raman Imaging of DNA and Protein Distribution in Apoptotic Cells. *Biophys J*, **2003**, *84*, 3968–3981.

[30] Chung, C.-Y.; Boik, J.; Potma, E.O. Biomolecular Imaging with Coherent Nonlinear Vibrational Microscopy. *Annu Rev Phys Chem*, **2013**, *64*, 77–99.

[31] Evans, C.L.; Xie, X.S. Coherent Anti-Stokes Raman Scattering Microscopy: Chemical Imaging for Biology and Medicine. *Annu Rev Anal Chem*, **2008**, *1*, 883–909.

[32] Brackmann, C.; Norbeck, J.; Åkeson, M.; Bosch, D.; Larsson, C.; Gustafsson, L.; Enejder, A.M.K. CARS Microscopy of Lipid Stores in Yeast: the Impact of Nutritional State and Genetic Background. *J Raman Spectrosc*, **2009**, *40*, 748–756.

[33] Wang, H.-W.; Fu, Y.; Huff, T.B.; Le, T.T.; Wang, H.; Cheng, J.-X. Chasing Lipids in Health and Diseases by Coherent Anti-Stokes Raman Scattering Microscopy. *Vib Spectrosc*, **2009**, *50*, 160–167.

[34] Matthäus, C.; Dochow, S.; Bergner, G.; Lattermann, A.; Romeike, B.F.M.; Marple, E.T.; Krafft, C.; Dietzek, B.; Brehm, B.R.; Popp, J. *In Vivo* Characterization of Atherosclerotic Plaque Depositions by Raman-Probe Spectroscopy and in Vitro Coherent Anti-Stokes Raman Scattering Microscopic Imaging on a Rabbit Model. *Anal Chem*, **2012**, *84*, 7845–7851.

[35] Gao, L.; Hammoudi, A.A.; Li, F.; Thrall, M.J.; Cagle, P.T.; Chen, Y.; Yang, J.; Xia, X.; Fan, Y.; Massoud, Y.; Wang, Z.; Wong, S.T.C. Differential Diagnosis of Lung Carcinoma with Three-Dimensional Quantitative Molecular Vibrational Imaging. *J Biomed Opt*, **2012**, *17*, 066017–1–066017–11.

[36] Selim, S.Z.; Ismail, M.A. K-Means-Type Algorithms: a Generalized Convergence Theorem and Characterization of Local Optimality. *IEEE Trans Pattern Anal Mach Intell*, **1984**, *6*, 81–87.

CHAPTER 4: Live-Cell Quantification of Mammalian Oocyte Cytosolic Lipid Content Using Nonlinear Vibrational Microscopy

The content of this chapter will be included into the following reference:

Jasensky J, Boughton AP, Khmaladze A, Ding J, Zhang C, Swain JE, Smith GW, Chen Z, Smith GD. Live-Cell Quantification of Mammalian Oocyte Cytosolic Lipid Content Using Nonlinear Vibrational Microscopy. **2015**, in preparation.

4.1 Introduction

Lipid droplets are ubiquitous structures found in nearly all cells [1]. Despite their established roles as facilitators for intercellular storage, energy availability, and membrane regulation, the idea of lipid droplets as essential cellular organelles has largely been neglected, and their importance in homeostasis and cellular function has only recently been addressed [1]. In cell systems such as the mammalian oocyte, intracellular lipids are found in various quantities [2,3], sizes [4,5], and compositions [4,6], and are a contributing factor in many aspects of oocyte physiology.

Cytosolic lipids, along with sugar substrates such as glucose, are a crucial source of endogenous energy for early oogenesis and subsequent embryogenesis [7-12], and such a demand in lipids for energy usage is seen not only in oocytes with a large amount of cytosolic lipid [13,14], but even in species where intracellular lipid content is low [7,15]. Evidence of this association can be seen in energy-consuming events such as meiosis. Meiotic progression causes a decrease in cytosolic lipid content [12,16,17]

and is accompanied by an increase in lipolysis [18]. When fatty acid metabolism is inhibited, blastocyst development rates decline [8]. Furthermore, enhancing fatty acid breakdown by the addition of L-carnitine to the culture medium during *in vitro* maturation significantly improves oocyte development [14,15].

Lipid content, while playing an important role in the growth and development of mammalian oocytes, is quantitatively inversely related to oocyte cryosurvival [19]. Components of the cell that control membrane fluidity and/or regulate water/cryoprotectant exchange impact dynamics of the freezing/vitrification process and influence mechanical stresses experienced by the cell [20]. The cell composition effect is especially important for oocytes that have a large cell volume and creates unique problems for successful cryopreservation. The physical damage as well as the biochemical stress caused by lipid during cryopreservation leads to very low embryo survival rates [21-25]. Recent work reporting strategies of improving cryosurvival demonstrate that delipation of porcine oocytes by either cytosolic extrusion or removal significantly improves their survival rate [19]. In addition, culturing embryos in the presence of compounds that reduce cytoplasmic lipid content improves cryotolerance [26,27].

To date, excellent work has been done to quantitatively summarize lipid content [6,28-31], composition [4,16,32-36], and behavior of lipid droplets [3,5,9,37] in both oocytes and embryos of various mammalian species, but the methods used come at the cost of cell lysis [29,32,33], fixation [4,16,34-36], or invasive labeling [5,6,9,28,31,37]. A few

recent studies have focused on using spontaneous Raman spectroscopy to chemically map fixed Metaphase II oocytes [38], as well as track biochemical progressions in embryogenesis [39]. Although Raman spectroscopy is inherently non-invasive, the long imaging times associated with spontaneous Raman inhibit live-cell imaging and hinder this technology's progression to clinical application. Due to the necessity of lipids for mammalian oocyte overall health, and the conditions in which many oocytes are used for non-terminal studies, there is need for a fast, live-cell noninvasive method to quantify cytosolic lipids. Such a technique would be useful not only for studying fundamental oocyte biology, but also for assessment and prediction of developmental competence in assisted reproductive technologies.

To this end, we explored a non-invasive method for the quantification of lipid in oocytes using coherent anti-Stokes Raman scattering (CARS) microscopy. CARS microscopy is a type of vibrational microscopy, capable of determining qualitative and quantitative information about molecular signatures and their distributions (details of our instrument are outlined in **Chapter 3**) [40]. This particular design implements a broadband excitation source allowing for both single-wavelength image acquisition, which generates CARS-PMT images, as well as a full spectra data set per pixel, or CARS-CCD images. Because CARS is a coherent process, acquisition times can be kept short for either method- entire images can be acquired within seconds to minutes, which is ideal for live samples that are highly sensitive to external stresses and are needed for continued development [41]. By determining total lipid content and lipid distributions based on CH stretching signals at 2850 cm^{-1}, a reliable, noninvasive assay can be

developed to measure intra-oocyte lipid content allowing for selection of cells based on predetermined criteria for maximal growth and survival.

4.2 Materials and Methods

4.2.1 Oocyte Collection/Preparation.

Oocyte samples were collected and prepared by our collaborator, Professor Gary Smith's research group in Department of Obstetrics and Gynecology, Physiology, and Urology at the University of Michigan. All animal procedures described within were reviewed and approved by The University Committee on Use and Care of Animals at the University of Michigan and were performed in accordance with the Guiding Principles for the Care and Use of Laboratory Animals. Human oocytes were obtained from the University of Michigan Center for Reproductive Medicine and were immature, unusable in an *in vitro* fertilization treatment cycle, and would otherwise have been discarded. Proposed use of otherwise discarded, de-identified, human oocytes was reviewed by the University of Michigan Medical School Institutional Review Board-Medicine (IRBMED #2001-0479) and considered "not regulated". Unless stated otherwise, all chemicals were used as received.

4.2.1.1 Murine Wild Type Oocytes.

Mouse meiotically incompetent germinal vesicle intact (GVI) oocytes were collected from female CF-1 mice (Harlan) at day 11-13 (d0=birth) by manually rupturing of pre-antral follicles. Oocytes were denuded and washed by repeatedly mouth pipetting in human tubal fluid + Hepes media (HTFH; Irvine Scientific) supplemented with 0.3%

bovine serum albumin (BSA; Fisher Scientific). Mouse meiotically competent GVI oocytes were collected from antral follicles of female CF-1 mice at day 21 after 42-44h 5IU equine chorionic gonadotropin (eCG; Sigma Aldrich) stimulation. The cumulus-enclosed oocytes were isolated by manually rupturing antral follicles, then denuded and washed in HTFH/0.3% BSA supplemented with 40 μM isobutylmethylxanthine (IBMX; Sigma Aldrich) to maintain meiotic arrest. Mouse metaphase I (MI) and metaphase II (MII) oocytes were collected at 7 h and 18 h culture after removal of IBMX, respectively.

4.2.1.2 Non-Murine Oocytes.

Bovine germinal vesicle (GV) stage oocytes were collected by aspiration from slaughterhouse ovaries, washed and placed into maturation media as previously described [42]. Oocytes were then matured in a 38.5°C incubator (5% CO_2, 5% O_2, 90% N_2) with 100% humidity for 14 h or 22 h to isolate MI and MII oocytes, respectively. Porcine oocytes were collected from slaughtered gilts by aspiration and then washed and placed in oocyte maturation media [42].

4.2.1.3 Murine ob/ob Oocytes.

Ten-week-old mouse ob/ob females were used for oocyte collection without hormone stimulation. Mouse meiotically incompetent and competent GVI oocytes were collected from pre-antral and antral follicles of the ovaries, respectively. Meiotically competent GVI oocytes from ob/ob females were transferred to center-well dishes containing HTF/0.3% BSA and cultured at 37°C in 5% CO_2 incubator for 18h yielding MII oocytes.

4.2.1.4 Pre-Imaging Oocyte Handling.

In preparation for CARS imaging, denuded oocytes for all experiments were quickly rinsed four times in HTFH/40μM IBMX media and placed onto the Poly-L-Lysine (Sigma Aldrich) coated glass-bottom petri dish (Ted Pella) containing 1-2mL HTFH/40μM IBMX media.

4.2.2 Fluorescence Imaging.

Fluorescence microscopy was used to image lipids in oocytes to validate CARS imaging results. In fluorescence imaging experiments, fixed oocytes were stained using Nile Red, a solvatochromatic dye [43] and counterstained with Hoechst33342 (Sigma). Meiotic stage was verified with Hoechst stain of DNA. Nile Red has been used previously to quantitatively assess lipid content in bovine oocytes [6,28,31,44]. Briefly, oocytes from porcine, bovine, murine, and human were adhered to Poly-L-Lysine coated coverslips and fixed overnight using 2% paraformaldehyde.

Fixed oocyte samples were triple washed with 1xPBS next day, stained with 100 nM Nile Red (Sigma) for 20 min at room temperature, then washed one time with 1xPBS and then stained with Hoechst33342 (5 μg/ml, Sigma) for 10 min. After Hoechst staining, oocyte samples were triple washed with 1xPBS, mounted in 90% glycerol with anti-fading reagent and analyzed via confocal microscopy. Confocal fluorescence imaging was performed at either the University of Michigan Single-Molecule Analysis in Real-Time (SMART) Center or Microscopy and Imaging Analysis Laboratory (MIL). Fixed, stained, and mounted oocyte confocal fluorescence images were taken using a

water immersion objective (Olympus, 60x 1.2 NA). Excitation source was tuned to 488 nm for Nile Red visualization as well as 405 nm for Hoechst visualization.

4.2.3 CARS Imaging.

Fig. 3.1 shows the schematic of our broadband CARS setup (see **Chapter 3** and reference [45] for a detailed description). Briefly, CARS is a third-order nonlinear optical process involving two laser beams: photons with frequencies ω_p and ω_S (pump and Stokes respectively), interact with the sample and generate a coherent optical signal at the anti-Stokes frequency ($2\omega_p - \omega_S$). Image contrast arises from the variations in chemical composition within the sample. Each individual chemical component has a unique Raman frequency, which consequently generates a chemical image for each unique species. In this way, image contrast is generated without perturbation to the sample (e.g., without the need to attach fluorescence labels). The pump and Stokes beams required to drive the CARS process originate from a single Ti:Sapphire (Spectra Physics) tunable oscillator operating at 800 nm, ~150 fs, and 80 MHz, and a photonic crystal fiber (PCF, NKT Photonics), respectively.

The resulting Stokes beam generated from the PCF is spectrally broad, which simultaneously excites all Raman vibrational modes in a sample. This allows our system to have the capability for both single wavelength detection by a photomultiplier tube (PMT), selecting only a single Raman frequency to collect, as well as broadband detection by a charge-coupled device (CCD) camera, collecting a large spectral window (~800 cm^{-1}). Methods of image analysis will be discussed in the **Section 4.2.4** and

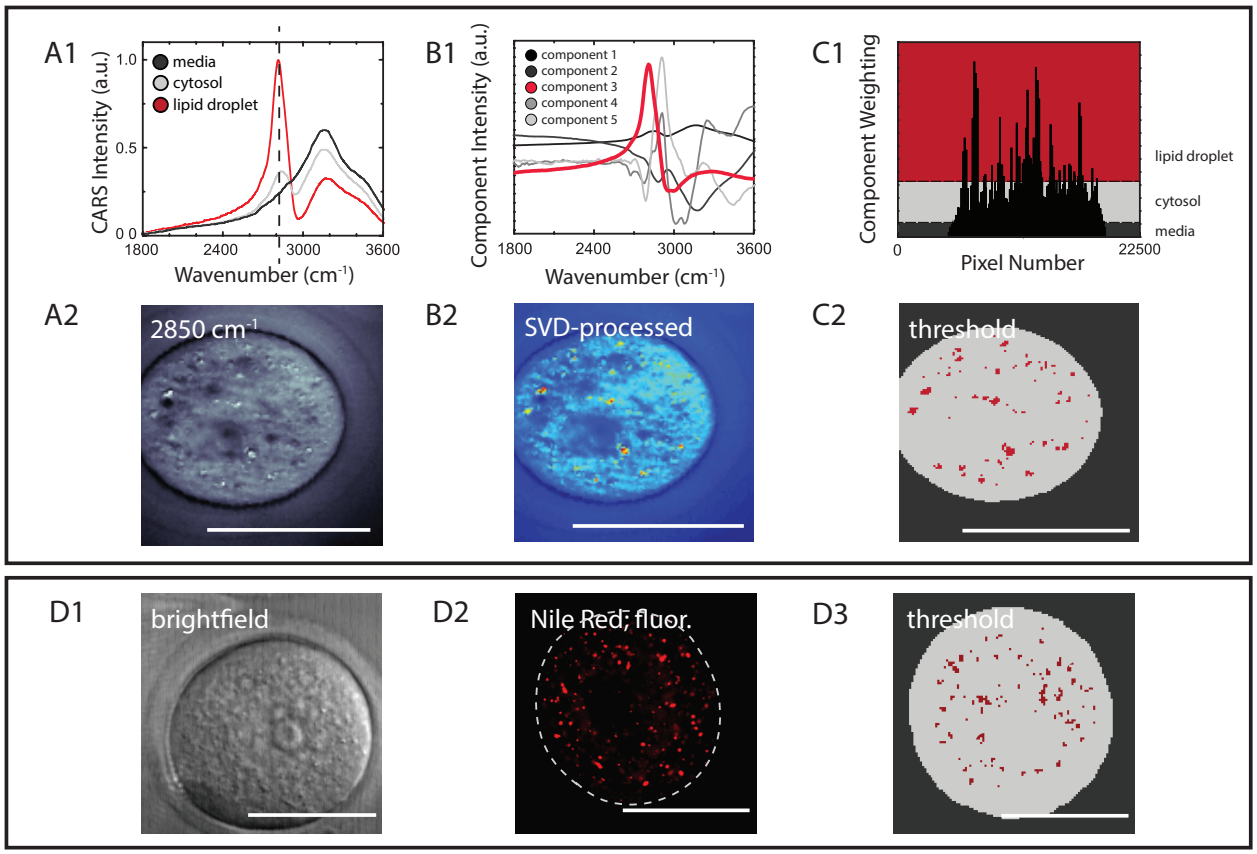

Figure 4.1: Multivariate Lipid Analysis and Droplet Identification. (A1,A2) Based on spectral signatures of various locations around the image, lipid droplets are defined as having large contributions of CH and lower amounts of OH. When reconstructing the data at 2850 cm^{-1}, we see visual conformation of lipid droplets. (B1,B2) After running SVD and choosing a component with a similar spectral lineshape, a component overlay is generated, matching A2. (C1,C2) Plotting the weightings of a particular component allows for cutoffs to be assigned, and a threshold image is generated. (D1-D3) Qualitative comparisons of brightfield, fluorescence by Nile Red, and CARS are shown. Scale bars 50 μm.

---

illustrated in **Fig. 4.1** and **4.2**.

All CARS imaging was done at room temperature (20°C) using a water-immersion objective (Olympus, 40x, 0.65 NA). Single-wavelength images were generated by observing CARS signal at 2850 cm^{-1} corresponding to CH_2 lipid signature. All oocyte images were generated at the equatorial position of the cell, the z-position where the zona pellucida was sharpest in the microscope binocular. The laser power at the sample

was ~6 mW and imaging times were 4 min per oocyte for CARS-PMT imaging and 20 min for CARS-CCD imaging. CARS signal generated from the sample was collected (in forward direction) by a condenser lens, and after the remaining pump and Stokes light was filtered out by a shortpass filter, was sent to a spectrometer (Oriel MS257) for acquisition by either imaging device.

4.2.4 Image Analysis.

Quantification of cytosolic lipid content requires the ability to: (1) accurately identify each lipid pixel in the CARS image as predominantly containing contributions of CH, and (2) from this identification, calculate the percentage of cell area containing lipid. Both single (CARS-PMT) and multi-wavelength (CARS-CCD) detection methods require independent methods of analysis to extract and calculate cross-sectional lipid percentage. Those methods are discussed below.

4.2.4.1 Multivariate: Singular Value Decomposition (SVD).

Multiplex images captured by the CCD camera contain the entire CARS vibrational spectrum at every pixel. In order to accurately identify lipid droplets in multivariate images, singular value decomposition (SVD) was implemented. The goal of SVD is to identify the most meaningful basis to re-express a data set, such as identifying the fewest number of unique spectra that make up all spectra within an entire image. Unlike similar procedures such as k-means clustering and principle component analysis, SVD is more noise-tolerant and requires fewer assumptions. It provided consistent results across all experiments.

In practice, SVD was run on raw, unprocessed hyperspectral imaging data arranged as an array of *m* variables x *n* spectra, using the "economy-sized" SVD implementation in MATLAB R2011a. The resulting right and left singular vectors can respectively be described as component lineshapes and weighted contributions of all components to each spectrum in the dataset. Since each pixel from a single image contains repeating spectral features, the first several component lineshapes generated from SVD generally describe all vibrational content in the system, and from this, these component lineshapes often resemble those of constituent chemical components. Reference unprocessed spectra (**Fig. 4.1** ***A1***) of three distinct regions typical of the chemical content found in oocytes show relative contributions of CH (lipid, 2850 cm^{-1}) and OH (water, 3200 cm^{-1}). It was found that media (the region outside of the oocyte) lacks

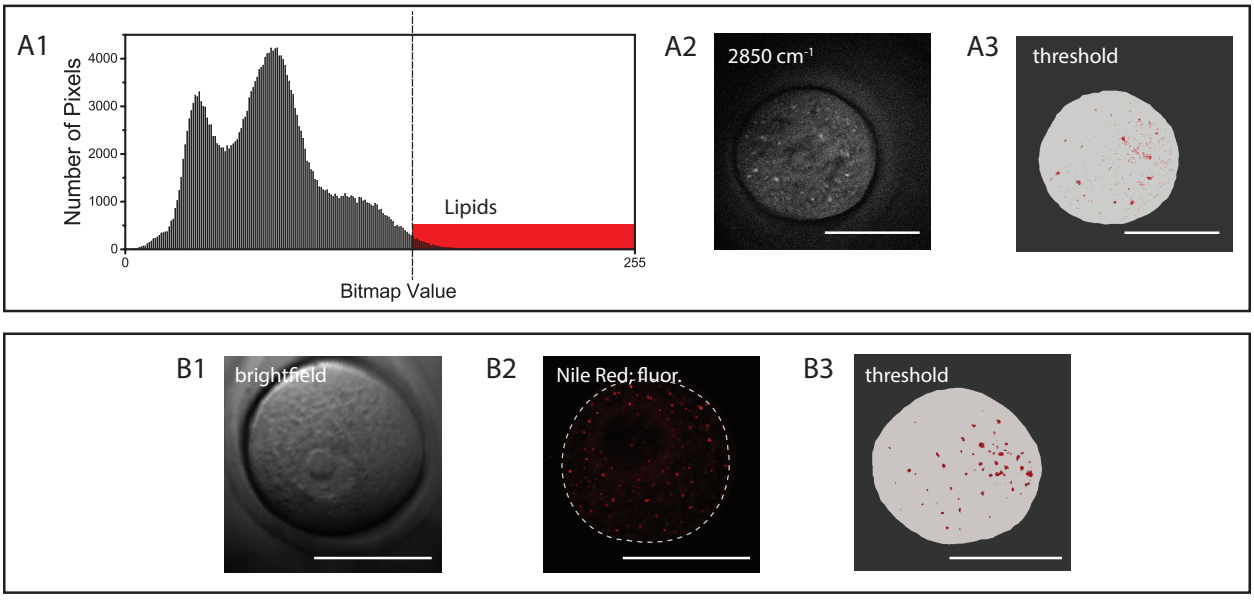

Figure 4.2: Univariate Lipid Analysis and Droplet Identification. (A1-A3) Lipid droplets in single-wavelength images are identified via intensity-based thresholding. Plotting pixels by increasing intensity and setting a cutoff results in a threshold image which looks similar to that seen for CARS imaging at 2850 cm^{-1}. (B1-B3) Qualitative comparisons between brightfield, fluorescence imaging with Nile Red, and CARS microscopy. Scale bar 50 µm.

strong contributions of lipid, therefore mostly signals are attributable to liquid water. Likewise, lipid droplets (regions of dense lipid concentration) show large CH signal intensity; such signals are from the CH_2 groups mostly contained in the lipid alkyl chains. From SVD, we are able to characterize and label each lipid droplet by choosing the component lineshape most closely representing reference spectra generated from pure components consisting of lipid (**Fig. 4.1** ***B1***). Once a single component has been identified as best representing a lipid chemical signature (a predominant signal at 2850 cm^{-1}), the contribution of the given component is plotted across each pixel (**Fig. 4.1** ***C1***) within the original image (**Fig. 4.1** ***A2***) to facilitate visual inspection of the data (**Fig 4.1** ***B2***). Lipid droplets were assigned based on choosing cutoffs for the pixels with sufficient contribution of lipid signal. Pixels with a smaller, but nonzero, lipid contribution are identified as cytosol. Once these components are identified a tricolor image is generated (**Fig. 4.1** ***C2***) and lipid content can be calculated as the ratio of pixels identified as lipid over all pixels identified as the oocyte or:

$$\text{oocyte lipid droplets (\% of visible cell area)} = \frac{\#\,pixels_{\text{lipid}}}{\#\,pixels_{\text{lipid}} + \#\,pixels_{\text{cell}}} \qquad (4.1)$$

4.2.4.2 Univariate: Intensity-Based Thresholding.

For PMT images, information from each pixel is given as a single intensity value, or the CARS intensity at a single wavelength. For this type of data set, intensity-based thresholding is required for lipid identification since it is known that image contrast comes from the difference in lipid amount per pixel. A GUI-based interface was developed in MATLAB (The MathWorks, Natick) to identify pixels from the image that

are lipid droplets. A top-hat filter and Weiner denoising filter were used to remove artifacts due to inhomogeneous illumination and strong pixel-to-pixel variation in the image, respectively. Once all filters were applied, a threshold value is determined that identifies all highest-intensity pixels as lipid droplets (**Fig. 4.2** ***A1***). Metrics to define an appropriate threshold value included a side-by-side comparison of threshold-generated image to original CARS-PMT image (**Fig. 4.2** ***A2*** and ***A3***). After a sufficient overlap of identified pixels was determined (in most cases, although dependent on each data set, was around the strongest 10% of pixels), lipid content was calculated in an identical manner using **Equation (4.1)**.

4.3 Results

4.3.1 CARS Microscopy for Live Oocyte Imaging.

A combination broadband and narrowband CARS system was designed for use in lipid droplet identification and quantification in live mammalian oocytes; details of this setup, its features, and subsequent image analysis are presented in Chapter 3 and Section 4.2. Because of their varied cellular chemistry and surrounding media, illumination with different wavelengths produces different chemical maps of the same live oocyte. When input light is tuned to match the OH stretching vibrational mode (3100 cm^{-1}), that indicative of water, CARS signal is shown diffuse and homogenous throughout and around the oocyte. When tuned to the CH stretching vibration (2850 cm^{-1}), bright localized signal is seen, which can be identified as cytosolic lipid droplets (**Fig. 4.3**).

Although **Figure 4.3** is an example of single-wavelength CARS imaging and the

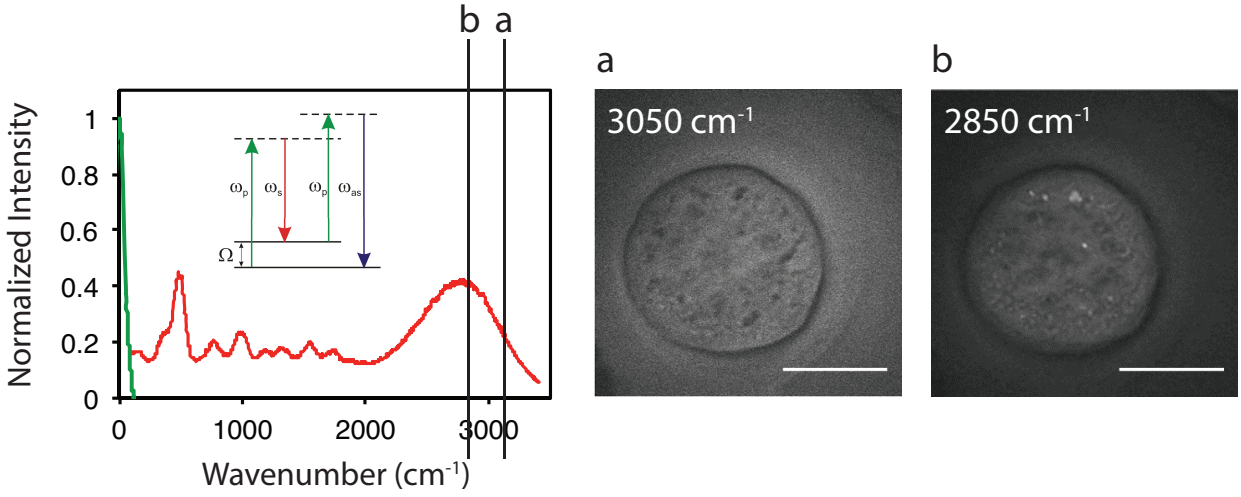

Figure 4.3: Chemical Mapping in Live Oocytes. Broadband CARS imaging, as seen in the energy diagram, requires input light of at least two unique frequencies. When the frequency of the Stokes bream is varied (red) different chemical distributions can be visualized. (a) Water signal (3100 cm^{-1}) shows diffuse signal through the oocyte and surrounding media. (b) Lipid signal (2850 cm^{-1}) is bright and localized. Scale bar 50 μm.

resulting micrographs are chemical distributions of independent chemical species, our input light is broadband (red) which results in the ability to image several different chemistries inherent in the sample simultaneously not often seen in assay-driven CARS microscopy using PMT detection and single wavelength imaging.

4.3.2 Lipid Droplet Identification Using CARS-CCD.

Our first experiments were to validate not only CARS microscopy as a noninvasive imaging tool for live oocytes, but also assess its ability to qualitatively identify lipid droplets similar to well-established techniques such as fluorescence microscopy. Spectral signatures (**Fig 4.1 *A1***) of oocytes collected via charged-coupled device (CCD) contain the presence of both CH (lipid) and OH (water) signals in different ratios corresponding to various regions of the micrograph; isolating only the CH intensity at 2850 cm^{-1} produces an image that highlights lipid droplets (**Fig 4.1 *A2***).

Results of SVD analysis reveal that the first several component spectra mimic chemical components found in **Fig 4.1 *A1***. Choosing the component that most closely represents lipid (**Fig 4.1 *B1***, component 3) and processing the image (**Fig 4.1 *B2***), more of which is explained in Section 3.3 and 4.2, produces an image similar to **Fig 4.1 *A1***. Setting appropriate cutoffs results in a threshold image, lipids identified, and similar to that in **Fig 4.1 *A2***. This threshold image is then used for subsequent lipid droplet quantification.

Comparisons between three different imaging modalities: brightfield, fluorescence imaging with fixed/stained oocytes using Nile Red, and live-cell CARS imaging of germinal vesicle intact (GVI) meiotically competent (MeC) oocytes (**Fig 4.1 *D***) show that not only is brightfield imaging lacking in chemical contrast, but that qualitatively both fluorescence and CARS microscopy identify lipid similarly.

4.3.3 Lipid Droplet Identification Using CARS-PMT.

With both multivariate (CCD) and univariate (PMT) imaging capabilities, our next objective was to compare lipid droplet identification in PMT imaging to that seen with fixed and stained oocytes. Unlike CCD hyperspectral data sets, PMT images contain a single intensity value per pixel. Therefore, the proper method for lipid identification, intensity-based thresholding, looks for those pixels that have the strongest CARS intensity (**Fig. 4.2 *A1***), or in the top 60%. Once identified, a composite threshold image is generated (**Fig 4.2 *A3***) and cross-referenced with lipid signatures at 2850 cm^{-1} (**Fig. 4.2 *A2***).

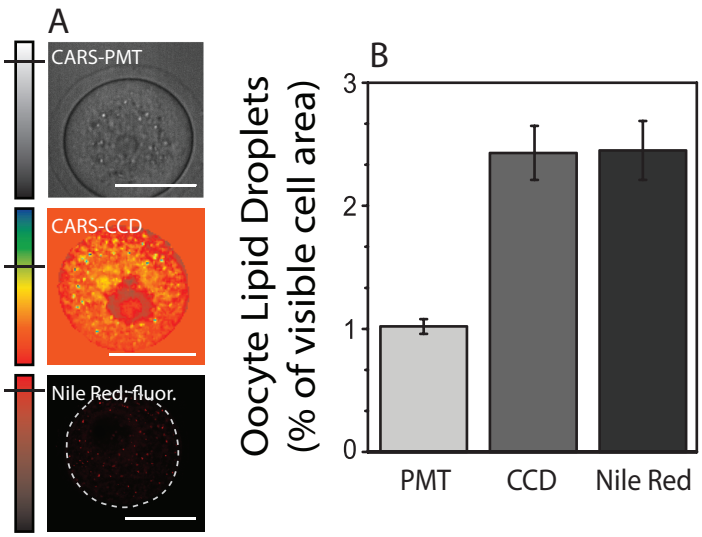

Figure 4.4: Lipid Droplet Quantification. (A) Representative micrographs of each imaging modality. Black indicator lines on color bars indicate where thresholding value is set. (B) Quantification results show good agreement with all three techniques. Scale bar 50 μm.

Fig 4.2 ***B*** shows the comparison of brightfield imaging to two chemically specific microscopies. **Fig 4.2** ***B1*** shows no chemical information while **Fig 4.2** ***B2*** and ***B3*** identify similar distributions of lipid droplets with fluorescence of fixed/stained oocytes and CARS of live oocytes.

4.3.4 Quantification of Lipid Droplets in CARS and Fluorescence Microscopy.

Calculated lipid content in all three imaging modalities: CARS-PMT (n=15), CARS-CCD (n=18), and Nile Red fluorescence imaging (n=10), show smiliarlity. Representative micrographs of each technique are shown in **Fig 4.4** ***A*** with thresholding values indicated on the colorbars with black lines.

CARS, a third-order nonlinear optical process, suffers from nonresonant background.

Details of this have been covered in Section 3.2 and will be elaborated upon in the Discussion section below. CARS-PMT suffers from this background the most and likewise underestimates the amount of lipid as compared to CARS-CCD. In spite of a strong nonresonant background, imaging times for CARS-PMT (2-4 minutes) are much more conducive to live oocyte imaging as compared to CARS-CCD (20 mintues) and were subsequently used as the primary noninvasive imaging technique.

4.3.5 Cross-Species Comparison of Lipid Content in Mammalian Oocytes.

Porcine (n=10), bovine (n=10), murine (n=7), and human (n=3) Metaphase I (MI) oocytes were used for our development of lipid quantification in mammalian oocytes using univariate CARS lipid analysis, CARS-PMT. Univariate CARS images collected of all 4 species demonstrated similar lipid droplet morphology and distribution when

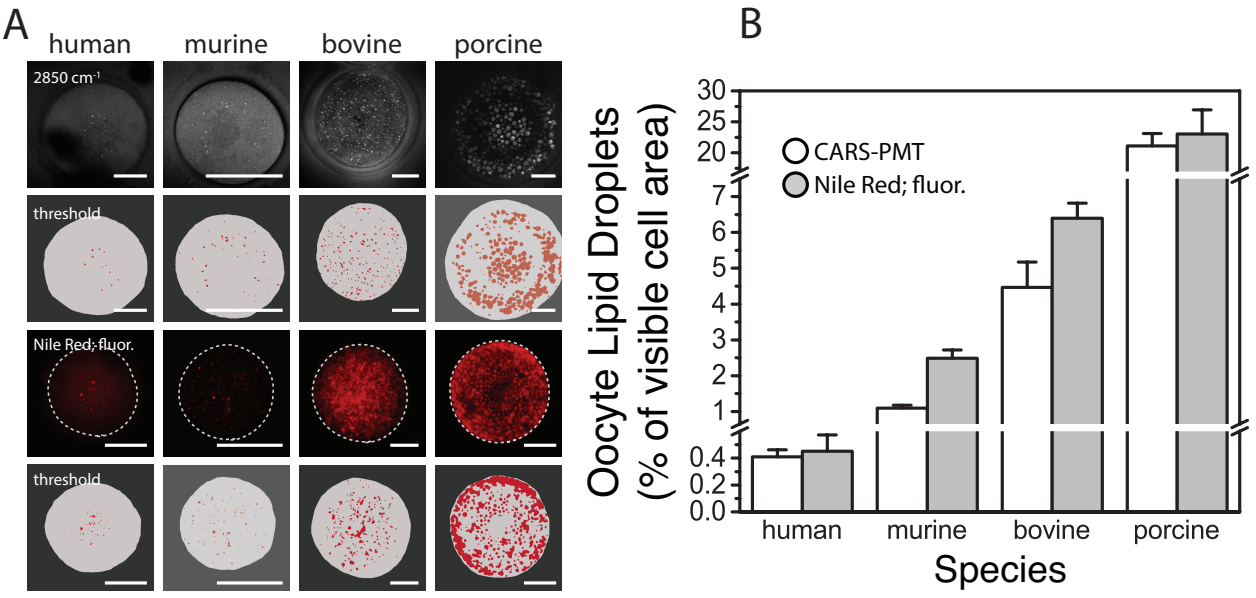

Figure 4.5: Lipid Droplet Quantification Across Mammalian Oocyte Species. (A) Representative micrographs of both CARS-PMT and Nile Red fluorescence with their respective thresholded images. (B) Quantification results show good agreement between fluorescence and CARS. Scale bar 50 μm.

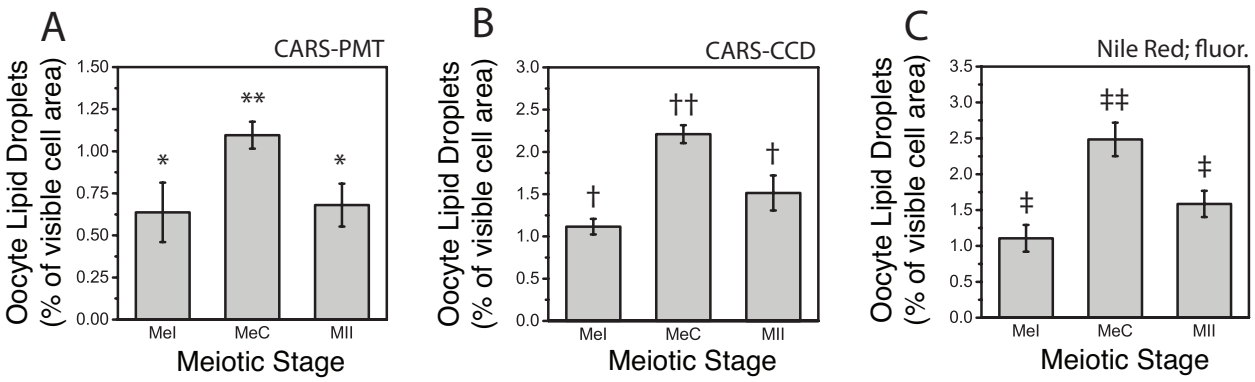

Figure 4.6: Lipid Content in Meiosis. All three imaging modalities capture identical trends, an increase in lipid content as oocytes gain meiotic competence and a decrease in lipid content as oocytes resume meiosis.

compared to fluorescence images fixed/stained with Nile Red (**Fig 4.5 *A***), and most importantly, percentages calculated with live-cell CARS-PMT are well correlated with fluorescence microscopy using a Pearson's correlation calculation (R=0.92; **Fig 4.5 *B***). Quantitatively, cytosolic lipid content using CARS imaging measured in porcine, bovine, murine, and human oocytes are 21.1±2.0%, 4.5±0.9%, 1.1±0.1%, and 0.4±0.04% ($p<0.05$; **Fig 4.5 *B***), respectively, which agrees with trends stated previously [29]. Additionally, this technology allowed the first-ever quantification of lipids in living human oocytes (**Fig. 4.5 *A***).

4.3.6 Oocyte Growth and Development.

CARS microscopy was used to quantify cytosolic lipid content in murine oocytes through oogenesis, based on non-survival studies suggesting an association of intracellular lipid and oocyte growth and development [7,10,15]. The use of broadband CARS microscopy by CCD and PMT-based detection (CARS-CCD and CARS-PMT, respectively) allowed for live-cell imaging of oocyte growth from germinal vesicle intact

meiotically incompetent (MeI) oocytes to germinal vesicle intact meiotically competent (MeC) oocytes, as well as the first meiotic progression to Metaphase II (MII). The details on analysis and lipid quantification of broadband CARS images detected using both techniques have been outlined in the Section 3.3 and **Fig 4.2** and **4.3**.

Live-cell imaging results using both CARS-PMT and CARS-CCD showed an increase in cytosolic lipid content as oocytes gain meiotic competence in preparation for the energy-consuming events of meiosis (CARS-PMT: MeI:0.6±0.1%; MeC:1.1±0.1%, $p<0.05$) (CARS-CCD: MeI:1.1±0.1%; MeC:2.2±0.2%, $p<0.01$). As oocytes resumed

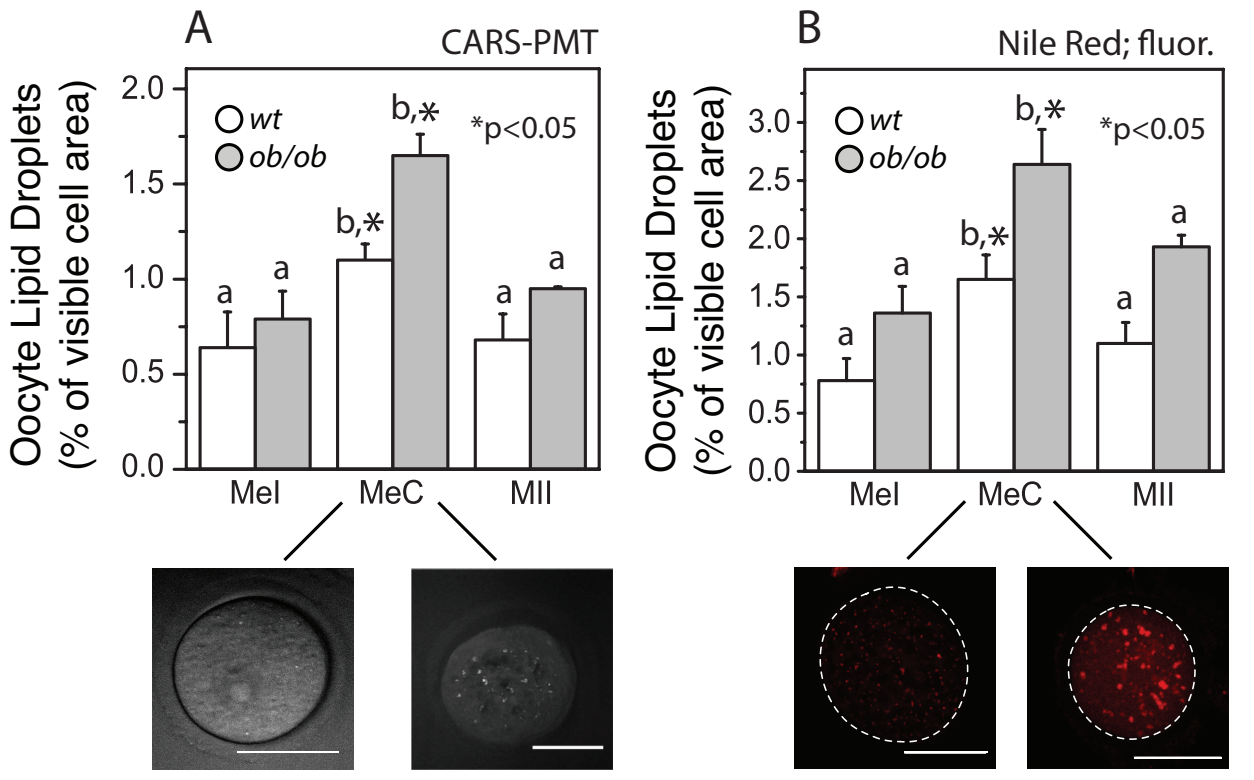

Figure 4.7: Lipid Content in Metabolic Disorder. Lipid droplet amount is markedly larger in all 3 developmental stages addressed with both (A) CARS-PMT and (B) Nile Red fluorescence. Significance was seen in MeC oocytes. Scale bar 50 μm.

meiosis and matured to Metaphase II, cytoplasmic lipids significantly decreased (CARS-PMT: MII 0.7±0.2%, $p<0.05$) (CARS-CCD: MII:1.5±0.2%, $p<0.01$), as demonstrated in **Fig 4.6**. Differences were confirmed in fixed/stained oocytes (MeI:1.1±0.2%; MeC:2.5±0.2%; MI:1.5±0.2%, $p<0.01$) using Nile Red.

4.3.7 Cytosolic Lipid Content in Metabolic Disorder.

Fig 4.7 shows the quantification of lipid content during oocyte growth and acquisition of meiotic competence (MeI to MeC transition) and resumption of oocyte meiosis (development to MII) using live-cell univariate CARS and fixed-cell fluorescence imaging. Mice exhibiting obesity caused by a mutation that inhibits production of leptin hormone (ob/ob) showed a marked increase in cytosolic lipid content for all three meiotic states (MeI, MeC, and MII) with significance seen in MeC oocytes. These oocytes also demonstrate a similar behavior in lipid usage through growth and development as seen in wild type oocytes. Representative CARS-PMT (**Fig 4.7 *A***) and fluorescence (**Fig 4.7 *B***) images of both wild type and ob/ob mice are shown.

The phenotypical response seen in oocytes of mothers who present metabolic disorder is a unique result with potential clinical impact, highlighting both the role of lipid as an intrinsic biomarker and the specific utility of CARS imaging. Differences in lipid content that vary within one donor's population may have significance on which oocytes have the best chance for survival.

4.4 Discussion

For the identification and quantification of cytosolic lipid content in live cells, coherent anti-Stokes Raman scattering (CARS) microscopy has demonstrated value in determining the dependence on lipid in oocyte physiology and homeostasis. Its noninvasive and label-free characteristics make it a promising tool for non-terminal studies on mammalian oocytes. We feel that, as a new technology in the field of reproduction, CARS microscopy has overcome many technological difficulties with live-cell chemical analysis.

Lipid as a dynamic organelle is becoming increasingly important as an intrinsic biomarker for oocyte health assessment. The role of this macromolecule role in energy and homeostasis allows techniques such as CARS microscopy to have predictive power for rational decision making regarding many areas of oocyte biology and reproductive therapies. Previous literature from several groups in oocyte lipid biology [9,12,15] have concluded that lipid is a necessity for successful embryogenesis. CARS microscopy, as shown in **Fig 4.6**, has the ability to distinguish changes in lipid content for three important points in oocyte growth and development. More importantly, oocytes that are morphologically similar, in the case of MeI and MeC oocytes, have the ability to be chemically distinguishable. These results become increasingly important when considering oocytes with low lipid content and in turn developing a meaningful method of which to monitor changes in this lipid content. This quantifiable difference between oocytes has potential in fertility preservation where few numbers of oocytes are often the norm, and decisions about the best outcome for survival for all oocytes can be made easier by a technique such as CARS microscopy.

Both CARS-CCD and CARS-PMT live-cell imaging are capable of identifying changes in cytosolic lipid content that match fluorescence staining of fixed cells in terminal studies. Although CARS-CCD imaging is faster than spontaneous Raman imaging [46,47], it is much slower compared to CARS-PMT imaging. CARS-CCD has value in its ability to elucidate a more complete chemical profile and can be used where oocytes must stay alive, but are not used for non-terminal studies.

Using fixed oocytes and non-viable staining, past studies have demonstrated that oocyte lipid content of different species vary significantly [4,12,29]. Imaging mammalian oocytes allowed for the opportunity to quantify the similarities in lipid quantification between both fluorescence and CARS. Several species of mammalian oocytes ranging from murine to porcine have varying amounts of cytosolic lipid, with all of these species having been measured by invasive methods such as staining [6], gas chromatography [29], and mass spectrometry [32]. The above quantitative values were generated from live oocyte CARS-PMT images collected within seconds to minutes, which is advantageous when dealing with cells that are highly sensitive to environmental perturbations that would compromise fertilization, embryogenesis, and/or establishment of a pregnancy. With the large lipid content seen in oocytes of species such as bovine and porcine, a method for quantifying such a biomarker would be invaluable for improving cryosurvival.

Benefits of a live-cell technique can been seen for domestic species. Species with

known difficulties in successful oocyte cryopreservation (e.g. bovine and porcine oocytes) have seen dedicated research in the goal for increasing survival rates. Chemical treatments such as phenazine ethosulfate have shown to decrease cytosolic lipid content [27], and ultimately enhance cryopreservation success. With the advent of CARS microscopy in such context, tailor-made treatments can hope to improve cryosurvival without comprising oocyte viability due to fixation or external labeling.

Results from this study demonstrate that not only does CARS microscopy have the ability to quantify lipid content in live oocytes, but these finding emphasize the importance of energy substrate accumulation during oocyte growth and cytosolic lipid reduction during energetically demanding processes such as meiosis. In addition, MeI and MeC oocytes, although morphologically similar, can be identified independently by their cytosolic lipid content. Such differences in lipid content, although small, were resolvable using this live-cell technique.

Strong correlations exist that link obesity to infertility, yet the causative factors are poorly understood [48]. While many factors contribute to fertility, the relationship of body composition to oocyte cytosolic lipid content has not been previously addressed. CARS-PMT imaging was further used to measure intracellular lipid content of oocytes from mice exhibiting obesity.

As the miniaturization and cost reduction of the major components of CARS microscopy

such as the laser, optical components, and detection system continue, opportunities for clinical analysis become a possibility. For metabolic diseases, CARS microscopy can further be used to correlate the causative factors that link obesity to infertility. In doing so, fertility preservation can also be enhanced with the induction of CARS microscopy.

4.5 Conclusion

Cytosolic lipids are a unique, yet essential resource for all mammalian cells, and their functions span a great range of cellular processes, some of which include energy supplementation. In search of a noninvasive method for accurate assessment and quantification of cytosolic lipid content, CARS microscopy has been found to be a valuable tool for single, live cell imaging. In conclusion, we have demonstrated that this technique can be used to quantify lipid content from living oocytes across a variety of species, including human, and with sensitivity capable of identifying intra-oocyte lipid changes in relation to body composition and during developmental events that are energy-consuming. There is still much to be learned about the role of lipids in cells, and the measurements made possible by using CARS can lead to greater insights into between cytosolic lipids, cellular energy homeostasis/consumption, and development biology. Additionally, because this live-cell technology would not hinder further oocyte development, future studies could investigate clinical applications in oocyte and embryo selection for human assisted reproductive technologies. As an example, because lipid content in oocytes/embryos is inversely related to cryosurvival [49], one can envision live-cell CARS utility in rational-decision-making in applications of oocyte/embryo cryopreservation for fertility preservation and/or infertility treatments. Finally, this live-cell

imaging of oocytes/embryos will also influence improvement of genetic gain in domestic species, and advance opportunities and efficiencies in rodent medical-genetic modeling.

4.6 References

[1] Walther, T.C.; Farese, R.V., Jr. The Life of Lipid Droplets. *Biochim Biophys Acta*, **2009**, *1791*, 459–466.

[2] Niu, Y.; Wang, C.; Xiong, Q.; Yang, X.; Chi, D.; Li, P.; Liu, H.; Li, J.; Huang, R. Distribution and Content of Lipid Droplets and Mitochondria in Pig Parthenogenetically Activated Embryos After Delipation. *Theriogenology*, **2015**, *83*, 131–138.

[3] Watanabe, T.; Thayil, A.; Jesacher, A.; Grieve, K.; Débarre, D.; Wilson, T.; Booth, M.; Srinivas, S. Characterisation of the Dynamic Behaviour of Lipid Droplets in the Early Mouse Embryo Using Adaptive Harmonic Generation Microscopy. *BMC Cell Biol*, **2010**, *11*, 38.

[4] McEvoy, T.G.; Coull, G.D.; Broadbent, P.J.; Hutchinson, J.S.; Speake, B.K. Fatty Acid Composition of Lipids in Immature Cattle, Pig and Sheep Oocytes with Intact Zona Pellucida. *J Reprod Fertil*, **2000**, *118*, 163–170.

[5] Castaneda, C.A.; Kaye, P.; Pantaleon, M.; Phillips, N.; Norman, S.; Fry, R.; D'Occhio, M.J. Lipid Content, Active Mitochondria and Brilliant Cresyl Blue Staining in Bovine Oocytes. *Theriogenology*, **2013**, *79*, 417–422.

[6] Romek, M.; Gajda, B.; Krzysztofowicz, E.; Kepczynski, M.; Smorąg, Z. New Technique to Quantify the Lipid Composition of Lipid Droplets in Porcine Oocytes and Pre-Implantation Embryos Using Nile Red Fluorescent Probe. *Theriogenology*, **2011**, *75*, 42–54.

[7] Dunning, K.R.; Cashman, K.; Russell, D.L.; Thompson, J.G.; Norman, R.J.; Robker, R.L. Beta-Oxidation Is Essential for Mouse Oocyte Developmental Competence and Early Embryo Development. *Biol Reprod*, **2010**, *83*, 909–918.

[8] Downs, S.M.; Mosey, J.L.; Klinger, J. Fatty Acid Oxidation and Meiotic Resumption in Mouse Oocytes. *Mol Reprod Dev*, **2009**, *76*, 844–853.

[9] Sturmey, R.G.; O'Toole, P.J.; Leese, H.J. Fluorescence Resonance Energy Transfer Analysis of Mitochondrial:Lipid Association in the Porcine Oocyte. *Reproduction*, **2006**, *132*, 829–837.

[10] Ferguson, E.M.; Leese, H.J. A Potential Role for Triglyceride as an Energy Source During Bovine Oocyte Maturation and Early Embryo Development. *Mol Reprod Dev*, **2006**, *73*, 1195–1201.

[11] Sturmey, R.G.; Reis, A.; Leese, H.J.; McEvoy, T.G. Role of Fatty Acids in Energy Provision During Oocyte Maturation and Early Embryo Development. *Reprod Dom Anim*, **2009**, *44*, 50–58.

[12] Sturmey, R.G.; Leese, H.J. Energy Metabolism in Pig Oocytes and Early Embryos. *Reproduction*, **2003**, *126*, 197–204.

[13] Sutton-McDowall, M.L.; Feil, D.; Robker, R.L.; Thompson, J.G.; Dunning, K.R. Utilization of Endogenous Fatty Acid Stores for Energy Production in Bovine Preimplantation Embryos. *Theriogenology*, **2012**, *77*, 1632–1641.

[14] Somfai, T.; Kaneda, M.; Akagi, S.; Watanabe, S.; Haraguchi, S.; Mizutani, E.; Dang-Nguyen, T.Q.; Geshi, M.; Kikuchi, K.; Nagai, T. Enhancement of Lipid Metabolism with L-Carnitine During *In Vitro* Maturation Improves Nuclear Maturation and Cleavage Ability of Follicular Porcine Oocytes. *Reprod Fertil Dev*, **2011**, *23*, 912–920.

[15] Dunning, K.R.; Akison, L.K.; Russell, D.L.; Norman, R.J.; Robker, R.L. Increased Beta-Oxidation and Improved Oocyte Developmental Competence in Response to L-Carnitine During Ovarian *In Vitro* Follicle Development in Mice. *Biol Reprod*, **2011**, *85*, 548–555.

[16] Ferguson, E.M.; Leese, H.J. Triglyceride Content of Bovine Oocytes and Early Embryos. *J Reprod Fertil*, **1999**, *116*, 373–378.

[17] Paczkowski, M.; Schoolcraft, W.B.; Krisher, R.L. Fatty Acid Metabolism During Maturation Affects Glucose Uptake and Is Essential to Oocyte Competence. *Reproduction*, **2014**, *148*,

429–439.

[18] Cetica, P.; Pintos, L.; Dalvit, G.; Beconi, M. Activity of Key Enzymes Involved in Glucose and Triglyceride Catabolism During Bovine Oocyte Maturation *In Vitro*. *Reproduction*, **2002**, *124*, 675–681.

[19] Hara, K.; Abe, Y.; Kumada, N.; Aono, N.; Kobayashi, J.; Matsumoto, H.; Sasada, H.; Sato, E. Extrusion and Removal of Lipid From the Cytoplasm of Porcine Oocytes at the Germinal Vesicle Stage: Centrifugation Under Hypertonic Conditions Influences Vitrification. *Cryobiology*, **2005**, *50*, 216–222.

[20] Isachenko, V.; Soler, C.; Isachenko, E.; Perez-Sanchez, F.; Grishchenko, V. Vitrification of Immature Porcine Oocytes: Effects of Lipid Droplets, Temperature, Cytoskeleton, and Addition and Removal of Cryoprotectant. *Cryobiology*, **1998**, *36*, 250–253.

[21] Nagashima, H.; Kashiwazaki, N.; Ashman, R.J.; Grupen, C.G.; Nottle, M.B. Cryopreservation of Porcine Embryos. *Nature*, **1995**, *374*, 416–416.

[22] Li, R.; Lai, L.; Wax, D.; Hao, Y.; Murphy, C.N.; Rieke, A.; Samuel, M.; Linville, M.L.; Korte, S.W.; Evans, R.W.; Turk, J.R.; Kang, J.X.; Witt, W.T.; Dai, Y.; Prather, R.S. Cloned Transgenic Swine via *In Vitro* Production and Cryopreservation. *Biol Reprod*, **2006**, *75*, 226–230.

[23] Du, Y.; Zhang, Y.; Li, J.; Kragh, P.M.; Kuwayama, M.; Ieda, S.; Zhang, X.; Schmidt, M.; Bøgh, I.B.; Purup, S.; Pedersen, A.M.; Villemoes, K.; Yang, H.; Bolund, L.; Vajta, G. Simplified Cryopreservation of Porcine Cloned Blastocysts. *Cryobiology*, **2007**, *54*, 181–187.

[24] Nagashima, H.; Kashiwazaki, N.; Ashman, R.J.; Grupen, C.G.; Seamark, R.F.; Nottle, M.B. Removal of Cytoplasmic Lipid Enhances the Tolerance of Porcine Embryos to Chilling. *Biol Reprod*, **1994**, *51*, 618–622.

[25] Esaki, R.; Ueda, H.; Kurome, M.; Hirakawa, K.; Tomii, R.; Yoshioka, H.; Ushijima, H.; Kuwayama, M.; Nagashima, H. Cryopreservation of Porcine Embryos Derived From *In Vitro*-Matured Oocytes. *Biol Reprod*, **2004**, *71*, 432–437.

[26] Sudano, M.J.; Paschoal, D.M.; da Silva Rascado, T.; Magalhães, L.C.O.; Crocomo, L.F.; Lima-Neto, J.F.; da Cruz Landim-Alvarenga, F. Lipid Content and Apoptosis of *In Vitro*-Produced Bovine Embryos as Determinants of Susceptibility to Vitrification. *Theriogenology*, **2011**, *75*, 1211–1220.

[27] Barceló-Fimbres, M.; Seidel, G.E., Jr. Effects of Fetal Calf Serum, Phenazine Ethosulfate and Either Glucose or Fructose During *In Vitro* Culture of Bovine Embryos on Embryonic Development After Cryopreservation. *Mol Reprod Dev*, **2007**, *74*, 1395–1405.

[28] Genicot, G.; Leroy, J.L.M.R.; Van Soom, A.; Donnay, I. The Use of a Fluorescent Dye, Nile Red, to Evaluate the Lipid Content of Single Mammalian Oocytes. *Theriogenology*, **2005**, *63*, 1181–1194.

[29] Loewenstein, J.E.; Cohen, A.I. Dry Mass, Lipid Content and Protein Content of the Intact and Zona-Free Mouse Ovum. *J Embryol Exp Morphol*, **1964**, *12*, 113–121.

[30] Hsieh, C.-S.; Chen, S.-U.; Lee, Y.-W.; Yang, Y.-S.; Sun, C.-K. Higher Harmonic Generation Microscopy of *In Vitro* Cultured Mammal Oocytes and Embryos. *Opt Express*, **2008**, *16*, 11574–11588.

[31] Van Soom, A.; Leroy, J.L.M.R.; Genicot, G.; Donnay, I. Evaluation of the Lipid Content in Bovine Oocytes and Embryos with Nile Red: a Practical Approach. *Reprod Dom Anim*, **2005**, *40*, 76–78.

[32] Ferreira, C.R.; Pirro, V.; Eberlin, L.S.; Hallett, J.E.; Cooks, R.G. Developmental Phases of Individual Mouse Preimplantation Embryos Characterized by Lipid Signatures Using Desorption Electrospray Ionization Mass Spectrometry. *Anal Bioanal Chem*, **2012**, *404*, 2915–2926.

[33] Coull, G.D.; Speake, B.K.; Staines, M.E.; Broadbent, P.J.; McEvoy, T.G. Lipid and Fatty Acid Composition of Zona-Intact Sheep Oocytes. *Theriogenology*, **1998**, *49*, 179.

[34] Kim, J.Y.; Kinoshita, M.; Ohnishi, M.; Fukui, Y. Lipid and Fatty Acid Analysis of Fresh and Frozen-Thawed Immature and *In Vitro* Matured Bovine Oocytes. *Reproduction*, **2001**, *122*, 131–138.

[35] Homa, S.T.; Racowsky, C.; McGaughey, R.W. Lipid Analysis of Immature Pig Oocytes. *J Reprod Fertil*, **1986**, *77*, 425–434.

[36] Menezo, Y.; Renard, J.-P.; Delobel, B.; Pageaux, J.-F. Kinetic Study of Fatty Acid Composition of Day 7 to Day 14 Cow Embryos. *Biol Reprod*, **1982**, *26*, 787–790.

[37] Sun, Q.Y.; Wu, G.M.; Lai, L.; Park, K.W.; Cabot, R.; Cheong, H.T.; Day, B.N.; Prather, R.S.; Schatten, H. Translocation of Active Mitochondria During Pig Oocyte Maturation, Fertilization and Early Embryo Development *In Vitro*. *Reproduction*, **2001**, *122*, 155–163.

[38] Wood, B.R.; Chernenko, T.; Matthäus, C.; Diem, M.; Chong, C.; Bernhard, U.; Jene, C.; Brandli, A.A.; McNaughton, D.; Tobin, M.J.; Trounson, A.; Lacham-Kaplan, O. Shedding New Light on the Molecular Architecture of Oocytes Using a Combination of Synchrotron Fourier Transform-Infrared and Raman Spectroscopic Mapping. *Anal Chem*, **2008**, *80*, 9065–9072.

[39] Davidson, B.; Spears, N.; Murray, A.; Elfick, A.P.D. The Changing Biochemical Composition and Organisation of the Murine Oocyte and Early Embryo as Revealed by Raman Spectroscopic Mapping. *J Raman Spectrosc*, **2011**, *43*, 24–31.

[40] Lin, C.-Y.; Suhalim, J.L.; Nien, C.L.; Miljković, M.D.; Diem, M.; Jester, J.V.; Potma, E.O. Picosecond Spectral Coherent Anti-Stokes Raman Scattering Imaging with Principal Component Analysis of Meibomian Glands. *J Biomed Opt*, **2011**, *16*, 021104–1–021104–9.

[41] Cheng, J.-X.; Xie, X.S. Coherent Anti-Stokes Raman Scattering Microscopy: Instrumentation, Theory, and Applications. *J Phys Chem B*, **2004**, *108*, 827–840.

[42] Bettegowda, A.; Patel, O.V.; Ireland, J.J.; Smith, G.W. Quantitative Analysis of Messenger RNA Abundance for Ribosomal Protein L-15, Cyclophilin-a, Phosphoglycerokinase, B-Glucuronidase, Glyceraldehyde 3-Phosphate Dehydrogenase, B-Actin, and Histone H2A During Bovine Oocyte Maturation and Early Embryogenesis *In Vitro*. *Mol Reprod Dev*, **2006**, *73*, 267–278.

[43] Greenspan, P.; Fowler, S.D. Spectrofluorometric Studies of the Lipid Probe, Nile Red. *J Lipid Res*, **1985**, *26*, 781–789.

[44] Barceló-Fimbres, M.; Seidel, G.E., Jr. Cross-Validation of Techniques for Measuring Lipid Content of Bovine Oocytes and Blastocysts. *Theriogenology*, **2011**, *75*, 434–444.

[45] Khmaladze, A.; Jasensky, J.; Price, E.; Zhang, C.; Boughton, A.P.; Han, X.; Seeley, E.; Liu, X.; Banaszak Holl, M.M.; Chen, Z. Hyperspectral Imaging and Characterization of Live Cells by Broadband Coherent Anti-Stokes Raman Scattering (CARS) Microscopy with Singular Value Decomposition (SVD) Analysis. *Appl Spectrosc*, **2014**, *68*, 1116–1122.

[46] Baldacchini, T.; He, X.N.; Allen, J.; Black, P.N.; Huang, X.; Huang, H.; Jiang, L.; Lu, Y.F. Coherent Anti-Stokes Raman Scattering and Spontaneous Raman Spectroscopy and Microscopy of Microalgae with Nitrogen Depletion. *Biomed Opt Express*, **2012**, *3*, 2896–2906.

[47] Petrov, G.I.; Arora, R.; Yakovlev, V.V.; Wang, X.; Sokolov, A.V.; Scully, M.O. Comparison of Coherent and Spontaneous Raman Microspectroscopies for Noninvasive Detection of Single Bacterial Endospores. *P Natl Acad Sci*, **2007**, *104*.

[48] Barash, I.A.; Cheung, C.C.; Weigle, D.S.; Ren, H.; Kabigting, E.B.; Kuijper, J.L.; Clifton, D.K.; Steiner, R.A. Leptin Is a Metabolic Signal to the Reproductive System. *Endocrinology*, **1996**, *137*, 3144–3147.

[49] Seidel, G.E., Jr. Modifying Oocytes and Embryos to Improve Their Cryopreservation. *Theriogenology*, **2006**, *65*, 228–235.

CHAPTER 5: Assessment of Acrosome Reaction in Human Spermatozoa Using Nonlinear Vibrational Microscopy

5.1 Introduction

In order to fertilize an oocyte, spermatozoa must undergo capacitation and acrosome reaction (AR) [1]. Capacitation typically occurs in the female reproductive tract and involves biochemical changes in the sperm membrane allowing better binding to the oocyte [2]. When capacitated spermatozoa reach the oocyte, they undergo AR as a response to the zona pellucida of the ovum. The AR involves fusing of the acrosome membrane and the outer membrane of the spermatozoon thereby exposing antigens and the enzymes hyaluronidase and acrosin to the oocyte [3,4]. This makes the spermatozoon capable of penetrating and fertilizing the egg. Spermatozoa that are not able to undergo AR or spermatozoa that prematurely undergo spontaneous AR are not able to fertilize the egg [5,6]. This, among other factors in male infertility, makes up 20% of all cases where male factor is solely responsible, and another 30-40% where male factor is contributory [7].

When couples with male factor infertility are presenting for assisted reproductive technology (ART), semen parameters have an important role in determining the best possible procedure. In cases of oligospermia or azoospermia (with sperm retrieval) the couple will have to undergo intracytoplasmic sperm injection (ICSI) [8]. In theory, only

one spermatozoon per oocyte is needed for injection but the frequency of abnormalities in the sperm increases with increased severity of the male factor infertility. Therefore, it is important to select spermatozoa with sufficient fertilizing capacity and semen parameters are insufficient for determining fertility potential. Of importance in fertilization is the AR and failure of capacitated sperm to undergo AR is associated with lack of fertilization *in vivo* and *in vitro*. Even when performing ICSI, the implantation rate and delivery rate is higher using AR sperm [9,10]. This would encourage the use of AR spermatozoa in ICSI and selecting spermatozoa, which have undergone acrosome reaction and without compromising their vitality, is crucial.

A major problem in the identification of the acrosome reaction of human spermatozoa is that the acrosome loss cannot be observed on living spermatozoa by phase contrast or differential interference contrast microscopy [11]. Currently, acrosome reaction can be determined by an AR assay where processed sperm is treated with calcium ionophore and then fixed and stained with fluorescein isothiocyanate (FITC) labeled *Pisum sativum* agglutinin and analyzed using a standard fluorescence microscope [11]. *Pisum sativum* agglutinin (PSA) has been proposed as an acrosomal stain based on the empirical finding that, when applied on permeabilized spermatozoa, it gives essentially the same staining patterns as an antiserum to the acrosomal enzyme acrosin [12]. Unfortunately, this technique is rather time consuming, and requires fixation and staining, which kills the analyzed spermatozoa and renders them unusable for ICSI or other fertility therapies.

Coherent anti-Stokes Raman scattering (CARS) microscopy promises to be a viable alternative; it's a non-invasive technique that can be performed on live cells and does not require staining. In many areas of biology and life sciences, CARS has been used to identify biomarkers in health and disease, to provide alternatives to biopsies and staining in pathology, and to elucidate the importance of lipids in biology and medicine [13-19]. Using this technique, it could be possible to determine acrosome reaction without harming the analyzed spermatozoa.

The objective of this study is to investigate if CARS can determine AR and to optimize the procedures when using this technique. It will be important to first develop a robust criterion for the identification of AR in human sperm cells using CARS microscopy. Details of system design and development of AR-identifiable criterion will be discussed

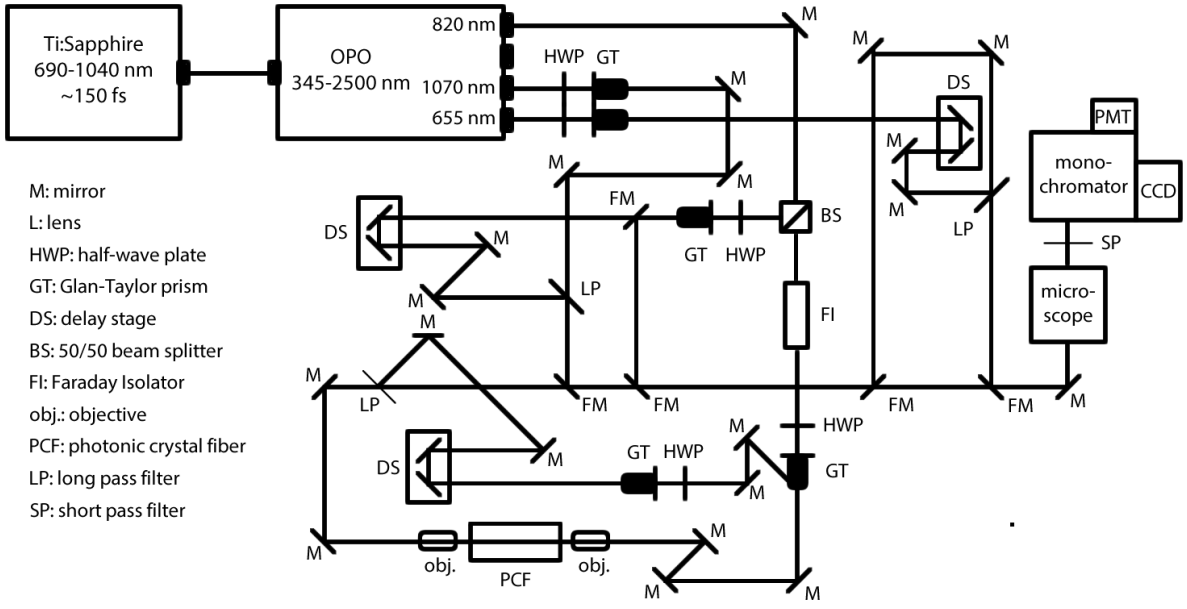

Figure 5.1: Narrowband CARS Schematic. Labels are included to the left of the diagram. All of the elements are present to perform both broadband CARS (with the included PCF) as well as narrowband CARS (with the OPO).

in the sections below.

5.2 Narrowband CARS Microscopy

In **Chapters 3** and **4**, our CARS system implemented a broadband CARS design, making use of a photonic crystal fiber (PCF) to generate a broad Stokes pulse and therefore simultaneously probing several Raman modes simultaneously. However, by spreading the energy for this Stokes pulse over multiple IR wavelengths, the energy per wavelength is limited, and only samples with large concentrations of target molecules are suitable for broadband CARS. Typically, for tissue and large cells (such as oocytes), broadband CARS is a powerful technique as it has the ability to visualize chemical distributions of many different species. However, for smaller cells (such as spermatozoa), this method is not practical.

An optical parametric oscillator (OPO) circumvents the need for a PCF and generates CARS signal by focusing this broadband energy into a single frequency. This will greatly increase the sensitivity of our measurements and facilitate the label-free imaging of lipids in very low concentrations. Our new narrowband CARS design is illustrated in **Fig 5.1**. Our current design incorporates the use of both broadband CARS (via PCF), as well as narrowband CARS (via OPO), all in the same design. These modes are interchangeable and allow the use of imaging the same sample with minimal realignment.

In order to demonstrate the signal enhancement of OPO CARS to that of PCF CARS, we first imaged a polystyrene standard - 3 μm pure polystyrene beads. Their CH-rich content makes them a good standard for CARS, both in their strong signal and for the ability for us to assess morphology and uniform sample illumination.

Fig 5.2 shows our results of comparing polystyrene beads in each of our CARS imaging modalities, PCF and OPO. Each representative picture is a single image generated with each technique. Both samples had the same input power (30 mW of 820 nm, 50 mW of 1070 nm) and were collected with the same detector, and otherwise had identical

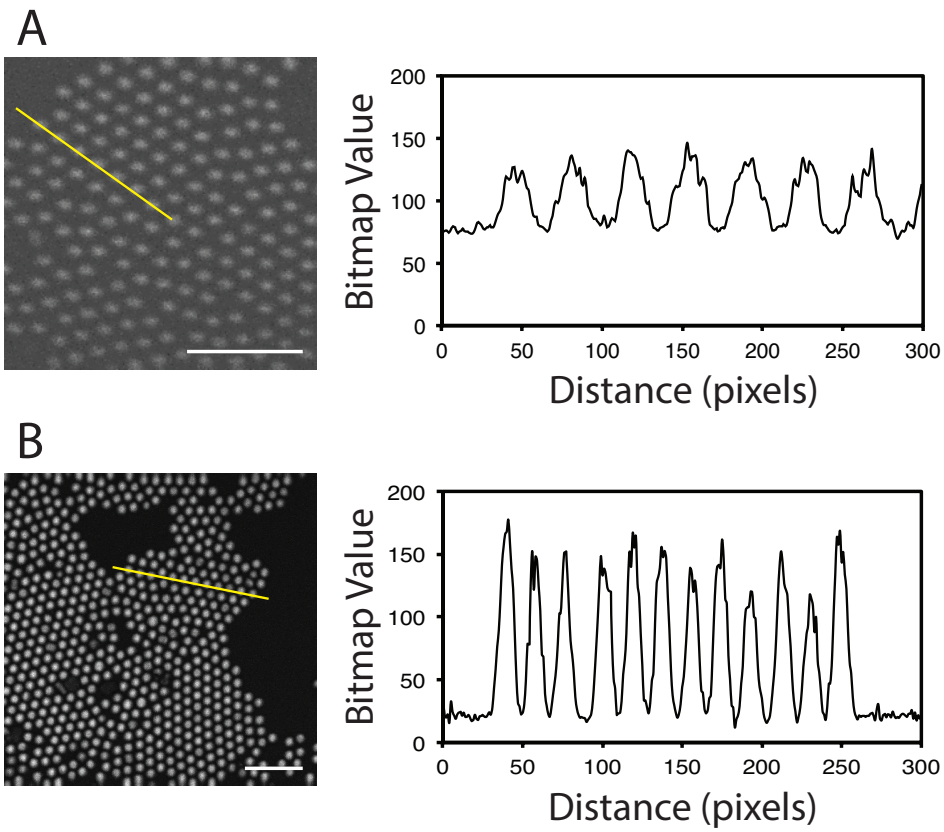

Figure 5.2: Comparison of PCF and OPO using Polystyrene Microspheres. Intensity profiles across each image demonstrate that (A) PCF-generated CARS images both have higher background lower signal-to-noise ratio than their (B) OPO counterparts. Yellow line indicates where intensity profile was measured. Scale bar 20 μm.

sample conditions. Results indicate that images taken using OPO CARS show an increase in the polystyrene bead signals (brighter) and a signal decrease of the background (darker), leading to a substantially higher signal to noise ratio (SNR).

5.3 Biochemical Understanding of Capacitation and the Acrosome Reaction

Capacitation is viewed as a reversible phenomenon which, upon completion, results in a decrease in the net negative surface charge, an efflux of membrane cholesterol, and an influx of calcium between the plasma and outer acrosomal membranes (**Fig 5.3 *B*** and ***C***) [20]. Triggered by the entry of calcium, the acrosome reaction involves phospholipid methylation and phospholipase A2 activation followed by a transient accumulation of unsaturated fatty acids and lysophospholipids implicated in membrane fusion, which occurs during the formation of membrane vesicles in mammalian spermatozoa undergoing the acrosome reaction (**Fig 5.3 *D*** and ***E***). The physiologic mammalian acrosome reaction is a membrane fusion event assumed to be experienced only by those spermatozoa that have been previously capacitated [21].

During sperm capacitation, a large morphological change in the removal and fusion of the outer membrane should be visualized with CARS microscopy. We define these parameters as our basis for criterion in assessing capacitation and acrosome reaction.

5.4 CARS Assessment of Acrosome Reaction

Semen samples were collected, prepared, and AR assay protocols were performed by Christian Jensen in Professor Gary Smith's lab at the University of Michigan.

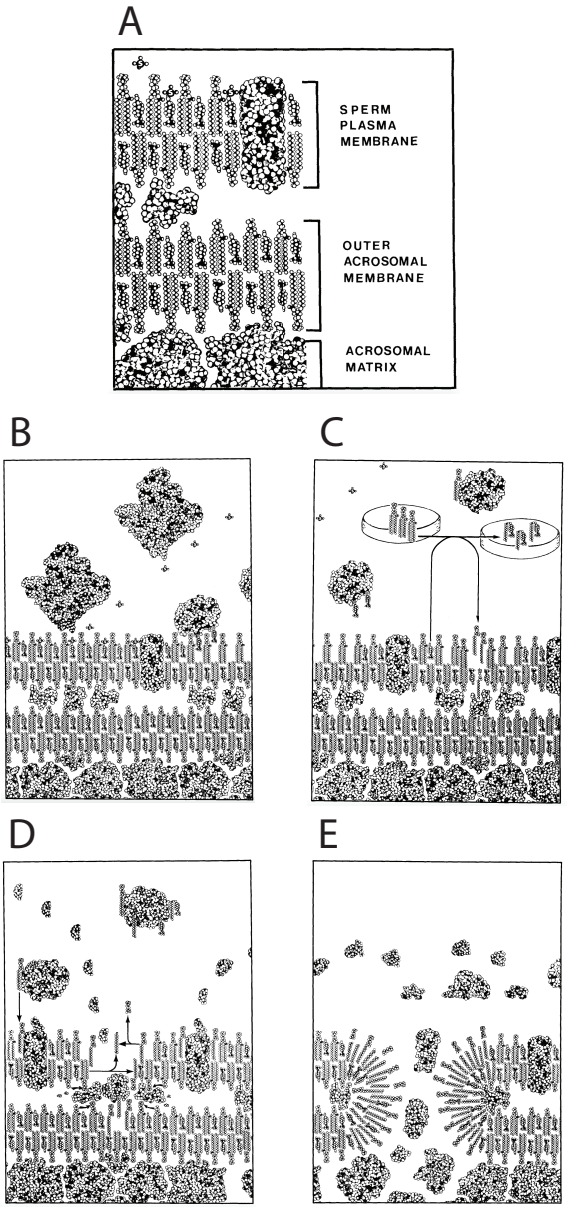

Figure 5.3: Membrane Model for Sperm Capacitation. Capacitation is a complex biochemical process with the ultimate goal of presenting enzymes necessary for AR outside the cell. This is achieved by several steps. (A) Schematic illustrating the various regions within the acrosomal region, and outside the cell. (B) Enzymatic hydrolysis of sulfate moieties covalently linked to membrane-bound sterols. (C) Efflux of those sterols from the outer membrane via several different proteins. (D) Metabolism of the outer membrane. (E) Fusion of the outer membrane with outer acrosomal membrane releasing necessary enzymes for sperm fusion and zona pellucida (ZP) breakdown.

Figure used, with permission, from: Langlais J and Roberts KD. *Gamete Res*, **1985**, *12*, 183–224.

5.4.1 Materials and Methods.

Normozoospermic ejaculates were obtained from the assisted reproductive technology (ART) laboratory at the University of Michigan. Ejaculates were first imaged with CARS microscopy were signal morphology was assessed in samples where AR percentage was not known). Imaging protocols for CARS microscopy can be reviewed in **Chapters 3** and **4**. Sperm samples were finally analyzed using an AR assay where immunofluorescent microscopy with PSA-FITC was used to compare criterion set by CARS to assess AR.

5.4.2 Results and Discussion.

Fig 5.4 illustrates the results of CARS imaging of individual sperm cells and their

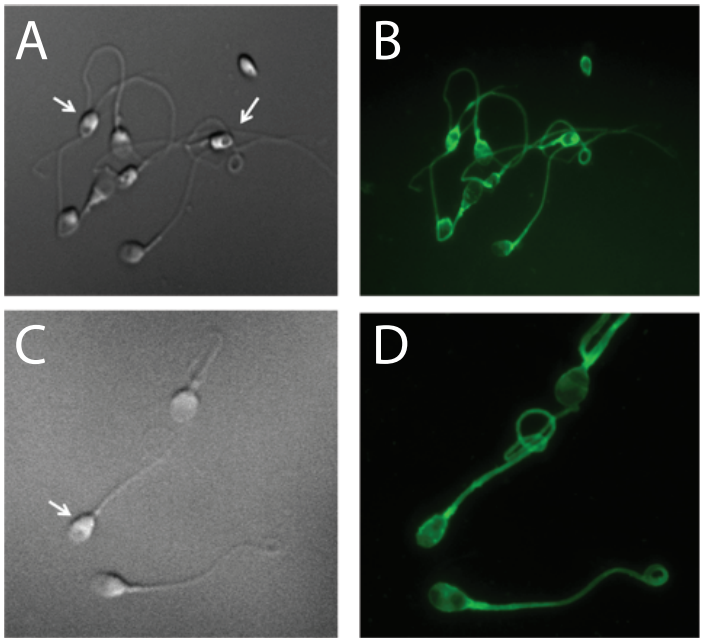

Figure 5.4: CARS Microscopy of Spermatozoa. Representative micrographs of fixed sperm imaged using (A,C) CARS and (B,D) fluorescence. White arrows indicate sperm that have been identified by fluorescence as non-acrosome reacted.

corresponding PSA-FITC images. Due to the high motility of live, healthy sperm cells, all cells were fixed in methanol before imaging. **Fig 5.4** ***A*** and ***C*** are representative CARS micrographs of unlabeled sperm cells, whereas **Fig 5.4** ***B*** and ***C*** show those same sperm cells with PSA-FITC fluorescence labeling. According to AR staining protocol [11], the location of the fluorescence signal indicates the acrosomal status of the cell. Sperm with bright caps (fluorescence at the top of the sperm head) are considered not acrosome reacted, whereas sperm with a dark cap (a lack of fluorescence in the same area) are considered acrosome reacted.

Indicated in white arrows are cells which have been identified using CARS microscopy as non acrosome reacted. According to the biochemical and morphological process that define capacitation and acrosome reaction, the fusion of the sperm plasma membrane with the acrosomal membrane should result in a "removal" of a single lipid bilayer, efflux of sterols such as cholesterol, and overall decrease in CARS signal around the outer periphery of the sperm head. Our criterion for non acrosome reacted sperm was then defined by the presence of an enhanced signal around the top of the sperm head. Those cells indicated with white arrows are those that we believe have expressed this criterion. These results match well with the fluorescence images in **Fig 5.4** ***B*** and ***D***.

With the introduction of narrowband CARS, it is possible to not only view strong signal throughout the sperm head, but even in low lipid areas such as the sperm tail, and outer membrane. From the details discussed in **Section 5.3**, and the results of fluorescence imaging, we see that sperm that have not undergone capacitation (or acrosome

reaction) seem to have brighter signal around the periphery of the acrosomal region.

Since this is a preliminary study into the ability for CARS to accurately identify acrosome reaction in sperm cells, our initial tests utilized fixed sperm cells due to their high motility. Our immediate next step is to perform a blinded study where samples of unknown acrosome percentage will be assessed with CARS microscopy and compared with fluorescence microscopy. Following these experiments, the goal is to transition towards live-cell imaging finding new and unique methods for temporary cell immobilization.

5.5 Conclusion

Due to the large percentages of infertility as a result of contributed male factors, a noninvasive assay to determine sperm health is vital for the success rate improvement of preexisting technologies such as ICSI. Although the reported results are preliminary, and the technology itself is new, the use of narrowband CARS as a method for sperm quality assessment is promising. In comparison to PCF-based CARS microscopy, the use of an OPO significantly increases the sensitivity of CARS signals, which can be seen both in polystyrene microspheres, as well as even smaller features such as the sperm tail with very low concentrations of lipid. Results from the study of AR by CARS support the idea that both capacitation and acrosome reaction are a product of membrane degradation and rearrangement. This can be visualized with narrowband CARS. Upon further refinement of the CARS AR assay, and a demonstration of its accuracy to conventional fluorescence, the transition of CARS towards a viable clinical

assay can be realized.

5.6 Future Research Plan

The preliminary results shown above demonstrate the potential for developing narrowband CARS microscopy for assessment of AR, and these are the first positive steps towards developing meaningful criteria for AR assessment. The following text describes the future important experiments to assess and verify these criteria.

5.6.1 Experimental Design.

Ten normozoospermic ejaculates will be obtained from the assisted reproductive technology (ART) laboratory at the University of Michigan. Ejaculates will be analyzed using an AR assay where the ejaculate is divided into 4 groups based on their treatment with sperm stimulant (SS) and calcium ionophore: (1). Control (-SS,-Ionophore), (2). Ionophore treated (-SS,+Ionophore), (3). SS treated control (+SS,-Ionophore), and (4). SS treated and ionophore treated (+SS,+Ionophore).

On all groups the following experiments will be carried out: (1) determination of the percent of AR spermatozoa using immunofluorescent microscopy, (2) determination of the percent of AR spermatozoa using CARS, and (3) investigation on whether the added chemicals in the AR assay interfere with the CARS signal using CARS to study control samples without any additives.

The 4 slides from the AR assay will be analyzed with CARS in a blinded fashion and the

results from the two procedures will be compared. Through such future studies, we aim to develop and test selection criteria for the assessment of acrosome reaction. These following experiments will determine if the developed criteria from **Section 5.4.2** can accurately identify acrosome reaction in human sperm cells. Following this study, CARS microscopy on live cells will be performed with the hope of assessment and selection of live spermatozoa with successful acrosome reaction.

5.7 References

[1] de Lamirande, E.; Leclerc, P.; Gagnon, C. Capacitation as a Regulatory Event That Primes Spermatozoa for the Acrosome Reaction and Fertilization. *Mol Hum Reprod*, **1997**, *3*, 175–194.

[2] Aitken, R.J.; Nixon, B. Sperm Capacitation: a Distant Landscape Glimpsed but Unexplored. *Mol Hum Reprod*, **2013**, *19*, 785–793.

[3] Yamagata, K.; Murayama, K.; Okabe, M.; Toshimori, K.; Nakanishi, T.; Kashiwabara, S.-I.; Baba, T. Acrosin Accelerates the Dispersal of Sperm Acrosomal Proteins During Acrosome Reaction. *J Biol Chem*, **1998**, *273*, 10470–10474.

[4] Mack, S.; Bhattacharyya, A.K.; Joyce, C.; van der Ven, H.; Zaneveld, L.J. Acrosomal Enzymes of Human Spermatozoa Before and After *In Vitro* Capacitation. *Biol Reprod*, **1983**, *28*, 1032–1042.

[5] Austin, C.R. Observations on the Penetration of the Sperm in the Mammalian Egg. *Aust J Sci Res B*, **1951**, *4*, 581–596.

[6] Chang, M.C. Fertilizing Capacity of Spermatozoa Deposited Into the Fallopian Tubes. *Nature*, **1951**, *168*, 697–698.

[7] Thonneau, P.; Marchand, S.; Tallec, A.; Ferial, M.-L.; Ducot, B.; Lansac, J.; Lopes, P.; Tabaste, J.-M.; Spira, A. Incidence and Main Causes of Infertility in a Resident Population (1,850,000) of Three French Regions (1988-1989). *Hum Reprod*, **1991**, *6*, 811–816.

[8] Nyboe Andersen, A.; Carlsen, E.; Loft, A. Trends in the Use of Intracytoplasmatic Sperm Injection Marked Variability Between Countries. *Hum Reprod Update*, **2008**, *14*, 593–604.

[9] Gianaroli, L.; Magli, M.C.; Ferraretti, A.P.; Crippa, A.; Lappi, M.; Capitani, S.; Baccetti, B. Birefringence Characteristics in Sperm Heads Allow for the Selection of Reacted Spermatozoa for Intracytoplasmic Sperm Injection. *Fertil Steril*, **2010**, *93*, 807–813.

[10] Lacham-Kaplan, O.; Trounson, A. Intracytoplasmic Sperm Injection in Mice: Increased Fertilization and Development to Term After Induction of the Acrosome Reaction. *Hum Reprod*, **1995**, *10*, 2642–2649.

[11] Mendoza, C.; Carreras, A.; Moos, J.; Tesarik, J. Distinction Between True Acrosome Reaction and Degenerative Acrosome Loss by a One-Step Staining Method Using *Pisum Sativum* Agglutinin. *J Reprod Fertil*, **1992**, *95*, 755–763.

[12] Cross, N.L.; Morales, P.; Overstreet, J.W.; Hanson, F.W. Two Simple Methods for Detecting Acrosome-Reacted Human Sperm. *Gamete Res*, **1986**, *15*, 213–226.

[13] Salameh, T.S.; Le, T.T.; Nichols, M.B.; Bauer, E.; Cheng, J.-X.; Camarillo, I.G. An *Ex Vivo* Co-Culture Model System to Evaluate Stromal-Epithelial Interactions in Breast Cancer. *Int J Cancer*, **2013**, *132*, 288–296.

[14] Pliss, A.; Kuzmin, A.N.; Kachynski, A.V.; Prasad, P.N. Biophotonic Probing of Macromolecular Transformations During Apoptosis. *P Natl Acad Sci*, **2010**, *107*, 12771–12776.

[15] Wang, H.-W.; Fu, Y.; Huff, T.B.; Le, T.T.; Wang, H.; Cheng, J.-X. Chasing Lipids in Health and Diseases by Coherent Anti-Stokes Raman Scattering Microscopy. *Vib Spectrosc*, **2009**, *50*, 160–167.

[16] Evans, C.L.; Xu, X.; Kesari, S.; Xie, X.S.; Wong, S.T.C.; Young, G.S. Chemically-Selective Imaging of Brain Structures with CARS Microscopy. *Opt Express*, **2007**, *15*, 12076–12085.

[17] Wang, H.; Fu, Y.; Zickmund, P.; Shi, R.; Cheng, J.-X. Coherent Anti-Stokes Raman Scattering Imaging of Axonal Myelin in Live Spinal Tissues. *Biophys J*, **2005**, *89*, 581–591.

[18] Le, T.T.; Huff, T.B.; Cheng, J.-X. Coherent Anti-Stokes Raman Scattering Imaging of Lipids in Cancer Metastasis. *BMC Cancer*, **2009**, *9*, 42–55.

[19] Masters, B.R. Correlation of Histology and Linear and Nonlinear Microscopy of the Living Human Cornea. *J Biophotonics*, **2009**, *2*, 127–139.

[20] Langlais, J.; Roberts, K.D. A Molecular Membrane Model of Sperm Capacitation and the Acrosome Reaction of Mammalian Spermatozoa. *Gamete Res*, **1985**, *12*, 183–224.

[21] Bedford, J.M. Sperm Capacitation and Fertilization in Mammals. *Biol Reprod Suppl*, **1970**, *2*, 128–158.

CHAPTER 6: Conclusions and Future Outlook

As we look back on the progress of modern analytical methods, we see major advances in the questions we are able to answer. With the introduction of devices such as the modern microscope to the laser, ever-more-exciting technologies are constantly in development and research fields are ever expanding as a result. As a specialized niche in biological and medical research, there is a growing need for noninvasive assays to solve important problems such as the treatment and management of various diseases, and illnesses or the reduction of threat from biological pathogens. In this thesis, two advanced optical analytical techniques, SFG spectroscopy and CARS microscopy, have been applied to study important biophysical processes as well as to determine biological significance.

6.1 Building a Better Surface – Optimizing Surface Behavior

In **Chapter 2**, I focus on understanding the behavior of surface-tethered antimicrobial peptides using sum frequency generation (SFG) spectroscopy. These peptides, among other advantages, have broad-spectrum affinity for bacteria and deter antibiotic resistance. MSI-78, the peptide of interest in this chapter, has potential in the development of biomolecule-based sensors, antibacterial textiles and medical dressings, as well as surfaces designed for pathogen elimination. By chemically

immobilizing MSI-78 via cysteine-maleimide coupling, we observe different behaviors of this surface bound peptide that are immobilization-site dependent. Ultimately, n-terminus attachment had a faster killing response against *E. coli*. This research demonstrated that SFG was the ideal tool for understanding surface behaviors of MSI-78. The peptide itself, only 10 nm in length, is the size of most fluorescence reporting molecules that would tether to this peptide. The tethered fluorescence molecules therefore may affect the behavior of immobilized MSI-78 – This shows the advantage of SFG which is label free. Other techniques, such as XPS, SPR, or AFM are label free, however have specific sample preparation requirement, use high vacuum, or are chemically nonspecific.

The result obtained from this chapter helps guide future work in optimizing surface parameters to promote the activity of surface-bound antimicrobial peptides. Surface chemistry may play a role in determining peptide surface orientation, leading to different peptide surface concentrations and either enhance or limit peptide-peptide interactions. As mentioned in **Chapter 2**, maleimide presents a slightly hydrophilic surface where the more polar c-terminus of the peptide readily interacts with the surface. This ultimately results in nMSI-78 lying down on the surface, but allows for cMSI-78 to stand up. Other techniques to change surface chemistry such as an alkyne surface that participates in click chemistry [1] may be used. Alternatively, altering peptide primary structure by incorporating helix promoting residues such as glycine and proline may help decrease peptide-surface interactions and allow nMSI-78 to stand up.

Such parameters as surface hydrophobicity/hydrophilicy, peptide-peptide interactions, linker chemistry, and other surface properties are just some of the questions that can be addressed using SFG supplemented with other analytical tools. Ultimately, questions about antimicrobial activity must be addressed by correlating observed tethering mechanisms to observed antimicrobial activity.

6.2 Building CARS Microscopy for Biomedical and Clinical Applications

For **Chapters 3**, **4**, and **5**, I focus on the use of noninvasive vibrational microscopy to answer fundamental questions about the roles that lipids play in reproductive health and disease. As an applicable technique in live-cell imaging, coherent anti-Stokes Raman scattering (CARS) microscopy is an ideal tool to aid in alleviating the major issues in infertility and fertility therapy. For these questions, broadband CARS microscopy was developed; its ability to capture chemical information for several unique species is important when assessing complex biological systems. In **Chapter 3**, system development of broadband CARS and data analysis methods using singular value decomposition (SVD) were described. They were extensively used for many research projects to follow.

Since the introduction of solid-state femtosecond laser sources, CARS has developed into a powerful laboratory-based label-free technique [2-5]. Unfortunately, in order for CARS itself to be incorporated into clinical assays, there must be a substantial cost reduction, miniaturization, and decrease in complexity-of-use. Fortunately, there have been many advances, both in system development and applications that open up

opportunities for vibrational imaging in assay-based clinical applications. The invention of fiber-lasers has drastically reduced both the size and cost of CARS light sources [6]. CARS microscopy using fiber-based delivery has also made CARS endoscopy possible [7,8]. It is with these developments that CARS microscopy has seen applications in cancer biology and tissue imaging [9-12]. In the next several years of CARS development, a push toward incorporation into clinic will drive the development of new systems and methods.

6.3 CARS in Oocyte Lipid Assessment

Cytosolic lipids are known to have functional importance for oocytes. CARS, which is most sensitive to lipid, was an ideal tool; its ability to image lipid droplets in several minutes is conducive for live cell imaging. Through this study (and discussed in detail in

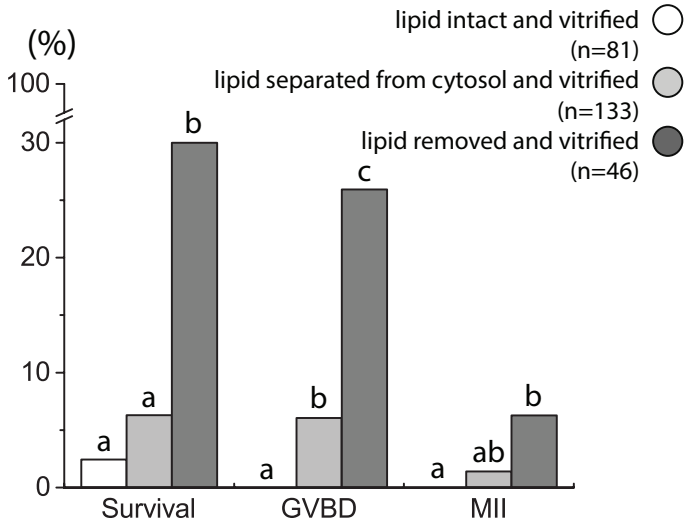

Figure 6.1: Oocyte Lipid Content in Cryosurvival. In porcine oocytes where lipid content is a large percent of overall cell volume, cryosuvival is low. When cytosolic lipids are either separated from the remaining cytosol or removed entirely from the cell, cryosurvival significantly improves.

Figure used, with permission, from: Hara K, Abe Y, Kumada N, Aono N, Kobayashi J, Matsumoto H, Sasada H, and Sato E. *Cryobiology*, **2005**, *50*, 216–222.

Chapter 4), we assessed the ability for CARS to not only identify lipid droplets (with fluorescence microscopy as the imaging standard), but also to uncover the potential for lipid to be used as an intrinsic biomarker for oocyte health. Lipid droplets show importance in oocyte growth and development, and differences in their amount can be associated with diseases such as metabolic syndrome. These are only a few examples of the impact that lipid has on reproductive biology.

Future work will require the assessment of CARS exposure and its effect on oocyte development. More specifically, does exposure of CARS excitation light (regardless of data collection) influence cleavage and blastocyst development? Several factors must be considered when assessing phototoxicity, which include (1) laser power, (2) pulse width, and (3) excitation wavelength [13,14]. Looking forward to applications of CARS in oocyte lipid biology, cryosurvival is inversely correlated to lipid content [15]. Oocytes with large percentage of lipid are difficult to cryopreserve, and development rates are low. When cytosolic lipid content is lowered, cryosurvival improves (**Fig 6.1**) [15]. CARS can therefore be used to assess lipid content noninvasively after treatments that either increase or reduce lipid content such as fetal calf serum or phenazine ethosulfate [16-18].

6.4 Assessment of Acrosome Reaction and DNA Integrity in Live Human Spermatozoa

The acrosome reaction, a necessary biochemical process that allows for the male spermatozoa to enter the oocyte, is one of the general factors associated with male

infertility. Using CARS microscopy, it was determined that this process of acrosome reaction, and the necessary capacitation that precedes it, involve changes in the lipid distribution within the acrosomal area. Details of which are discussed in **Chapter 5**. Current methods for assessing acrosome reaction involve cellular fixation and fluorescence staining. CARS microscopy has clinical value as a noninvasive tool to assess sperm health. This along with other factors such as DNA integrity [19,20] will help transition CARS into a viable diagnostic tool.

Current preliminary studies utilizing CARS microscopy were performed on fixed spermatozoa. Progression towards a live-cell assay is critical in the development of

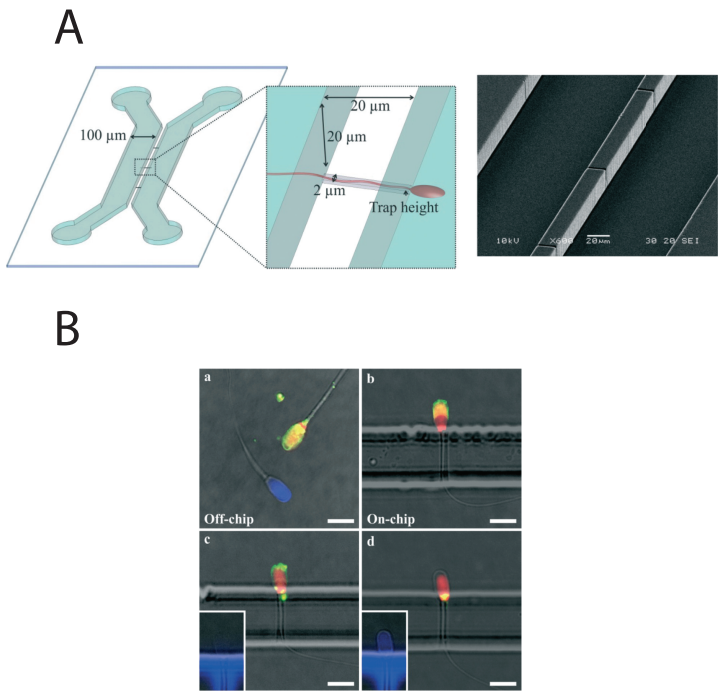

Figure 6.2: Proposed Microfluidic Device for Live Cell Measurements. (A) Microfluidic device capable of trapping single sperm cells in microchannels. These sperm cells can subsequently be assessed by microscopic techniques such as fluorescence or CARS. (B) Assessment of acrosome reaction in single cells by PSA-FITC.

Figure used, with permission, from: de Wagenaar B, Berendsen JTW, Bomer JG, Olthuis W, van den Berg A, Segerink LI. *Lab Chip*, **2015**, *15*, 1294–1301.

CARS microscopy for clinical use. **Fig 6.2** is a microfluidic device designed for the isolation of single sperm cells for microscopic analysis [21]. Other devices based on dielectrophoresis have also been proposed for cell entrapment or increasing local cell concentration [22]. Such a device, in combination with CARS microscopy, will facilitate live-cell assessment of acrosome reaction.

6.5 Conclusion

As label free techniques, vibrational spectroscopy and microscopy have great advantages in biophysical, biological, and medical research. Nonlinear vibrational spectroscopy will keep finding novel applications in basic science and industry-driven research, where noninvasiveness is of the most importance. Just as new techniques are in continuous development, we will also see a steady growth in areas of science and technology that will make them part of their research needs.

6.6 References

[1] Li, Y.; Wei, S.; Wu, J.; Jasensky, J.; Xi, C.; Li, H.; Xu, Y.; Wang, Q.; Marsh, E.N.G.; Brooks, C.L., III; Chen, Z. Effects of Peptide Immobilization Sites on the Structure and Activity of Surface-Tethered Antimicrobial Peptides. *J Phys Chem C*, **2015**, *119*, 7146–7155.

[2] Tolles, W.M.; Nibler, J.W.; McDonald, J.R.; Harvey, A.B. A Review of the Theory and Application of Coherent Anti-Stokes Raman Spectroscopy (CARS). *Appl Spectrosc*, **1977**, *31*, 253–271.

[3] Cheng, J.-X. Coherent Anti-Stokes Raman Scattering Microscopy. *Appl Spectrosc*, **2007**, *61*, 197A–208A.

[4] Evans, C.L.; Xie, X.S. Coherent Anti-Stokes Raman Scattering Microscopy: Chemical Imaging for Biology and Medicine. *Annu Rev Anal Chem*, **2008**, *1*, 883–909.

[5] Pezacki, J.P.; Blake, J.A.; Danielson, D.C.; Kennedy, D.C.; Lyn, R.K.; Singaravelu, R. Chemical Contrast for Imaging Living Systems:Molecular Vibrations Drive Cars Microscopy. *Nat Chem Biol*, **2011**, *7*, 137–145.

[6] Selm, R.; Winterhalder, M.; Zumbusch, A.; Krauss, G.; Hanke, T.; Sell, A.; Leitenstorfer, A. Ultrabroadband Background-Free Coherent Anti-Stokes Raman Scattering Microscopy Based on a Compact Er:Fiber Laser System. *Opt Lett*, **2010**, *35*, 3282–3284.

[7] Shim, M.G.; Wong Kee Song, L.-M.; Marcon, N.E.; Wilson, B.C. *In Vivo* Near-Infrared Raman Spectroscopy: Demonstration of Feasibility During Clinical Gastrointestinal Endoscopy. *Photochem Photobiol*, **2000**, *72*, 146–150.

[8] Balu, M.; Liu, G.; Chen, Z.; Tromberg, B.J.; Potma, E.O. Fiber Delivered Probe for Efficient CARS Imaging of Tissues. *Opt Express*, **2010**, *18*, 2380–2388.

[9] Krafft, C.; Ramoji, A.A.; Bielecki, C.; Volger, N.; Meyer, T.; Akimov, D.; Rösch, P.; Schmitt, M.; Dietzek, B.; Petersen, I.; Stallmach, A.; Popp, J. A Comparative Raman and CARS Imaging Study of Colon Tissue. *J Biophotonics*, **2009**, *2*, 303–312.

[10] Salameh, T.S.; Le, T.T.; Nichols, M.B.; Bauer, E.; Cheng, J.-X.; Camarillo, I.G. An *Ex Vivo* Co-Culture Model System to Evaluate Stromal-Epithelial Interactions in Breast Cancer. *Int J Cancer*, **2013**, *132*, 288–296.

[11] Mitra, R.; Chao, O.; Urasaki, Y.; Goodman, O.B.; Le, T.T. Detection of Lipid-Rich Prostate Circulating Tumour Cells with Coherent Anti-Stokes Raman Scattering Microscopy. *BMC Cancer*, **2012**, *12*, 1–9.

[12] Lim, R.S.; Suhalim, J.L.; Miyazaki-Anzai, S.; Miyazaki, M.; Levi, M.; Potma, E.O.; Tromberg, B.J. Identification of Cholesterol Crystals in Plaques of Atherosclerotic Mice Using Hyperspectral CARS Imaging. *J Lipid Res*, **2011**, *52*, 2177–2186.

[13] Fu, Y.; Wang, H.; Shi, R.; Cheng, J.-X. Characterization of Photodamage in Coherent Anti-Stokes Raman Scattering Microscopy. *Opt Express*, **2006**, *14*, 3942–3951.

[14] Koester, H.J.; Baur, D.; Uhl, R.; Hell, S.W. Ca^{2+} Fluorescence Imaging with Pico- and Femtosecond Two-Photon Excitation: Signal and Photodamage. *Biophys J*, **1999**, *77*, 2226–2236.

[15] Hara, K.; Abe, Y.; Kumada, N.; Aono, N.; Kobayashi, J.; Matsumoto, H.; Sasada, H.; Sato, E. Extrusion and Removal of Lipid From the Cytoplasm of Porcine Oocytes at the Germinal Vesicle Stage: Centrifugation Under Hypertonic Conditions Influences Vitrification. *Cryobiology*, **2005**, *50*, 216–222.

[16] Barceló-Fimbres, M.; Seidel, G.E., Jr. Effects of Fetal Calf Serum, Phenazine Ethosulfate and Either Glucose or Fructose During *In Vitro* Culture of Bovine Embryos on Embryonic Development After Cryopreservation. *Mol Reprod Dev*, **2007**, *74*, 1395–1405.

[17] Abe, H.; Yamashita, S.; Satoh, T.; Hoshi, H. Accumulation of Cytoplasmic Lipid Droplets in

Bovine Embryos and Cryotolerance of Embryos Developed in Different Culture Systems Using Serum-Free or Serum-Containing Media. *Mol Reprod Dev*, **2002**, *61*, 57–66.

[18] Seidel, G.E., Jr. Modifying Oocytes and Embryos to Improve Their Cryopreservation. *Theriogenology*, **2006**, *65*, 228–235.

[19] Sánchez, V.; Redmann, K.; Wistuba, J.; Wübbeling, F.; Burger, M.; Oldenhof, H.; Wolkers, W.F.; Kliesch, S.; Schlatt, S.; Mallidis, C. Oxidative DNA Damage in Human Sperm Can Be Detected by Raman Microspectroscopy. *Fertil Steril*, **2012**, *98*, 1124–1129.

[20] Mallidis, C.; Wistuba, J.; Bleisteiner, B.; Damm, O.S.; Groß, P.; Wübbeling, F.; Fallnich, C.; Burger, M.; Schlatt, S. *In Situ* Visualization of Damaged DNA in Human Sperm by Raman Microspectroscopy. *Hum Reprod*, **2011**, *26*, 1641–1649.

[21] de Wagenaar, B.; Berendsen, J.T.W.; Bomer, J.G.; Olthuis, W.; van den Berg, A.; Segerink, L.I. Microfluidic Single Sperm Entrapment and Analysis. *Lab Chip*, **2015**, *15*, 1294–1301.

[22] Iliescu, C.; Xu, G.L.; Samper, V.; Tay, F.E.H. Fabrication of a Dielectrophoretic Chip with 3D Silicon Electrodes. *J Micromech Microeng*, **2004**, *15*, 494–500.